UNIVERSIDADE D
COIMBRA

João Pedro Pinto Vieira

UTILIZATION OF SILICA NANOPARTICLES FOR TRANSPORT AND DELIVERY OF A RECOMBINANT PROTEIN FOR CANCER TREATMENT

Dissertação no âmbito do Mestrado em Bioquímica,
orientada pela Professora Doutora Paula Cristina Veríssimo Pires
e pelo Professor Doutor Henrique Manuel dos Santos Faneca
e apresentada ao Departamento de Ciências da Vida da Faculdade de Ciências e Tecnologia
da Universidade de Coimbra.

Setembro de 2019

1 2 9 0

FACULDADE DE CIÊNCIAS E TECNOLOGIA
UNIVERSIDADE D COIMBRA

UTILIZATION OF SILICA NANOPARTICLES FOR TRANSPORT AND DELIVERY OF A RECOMBINANT PROTEIN FOR CANCER TREATMENT

João Pedro Pinto Vieira

Paula Cristina Veríssimo Pires

Henrique Manuel dos Santos Faneca

Coimbra,

September 2019

This work was performed at the Biotechnology Laboratory and the Nanosystems and Targeted Antitumor Strategies groups, at the Center for Neuroscience and Cell Biology of University of Coimbra, Portugal, under the supervision of. Paula Veríssimo, PhD (DCV-UC) and Henrique Faneca, PhD (DCV-UC).

This work was supported by the Portuguese Foundation for Science and Technology (FCT) and the European Regional Development Fund (ERDF) through the COMPETE program (Operational Program for Competitiveness) [grant numbers: IF/01007/2015, POCI-01-0145-FEDER-30916 and UID/NEU/04539/2019]

Agradecimentos

Após o fim de um longo ano de trabalho que culminou na escrita desta dissertação, imperam as sensações de dever cumprido e de satisfação pessoal perante os objetivos aqui alcançados. Como tal, tenho total consciência de que o apoio de imensas pessoas que, felizmente, sempre tive a meu lado, foi fundamental para que isto chegasse a bom porto.

As minhas primeiras palavras de agradecimento vão necessariamente para a Prof. Doutora. Paula Veríssimo pelo exemplo de rigor, seriedade, excelência e paciência que sempre demonstrou ser desde que nos conhecemos nas aulas de Laboratórios de Enzimologia e Química de Proteínas, no 3º ano da minha licenciatura, até à conclusão do mestrado. Tenho total consciência de que tudo o que alcançar daqui em diante será fruto de um acompanhamento irrepreensível, quer a nível técnico e prático quer a nível pessoal, não só durante a realização do trabalho laboratorial para esta dissertação, como também em contextos de sala de aula e extracurriculares. Logicamente que estas palavras se estendem ao Prof. Doutor. Henrique Faneca, que me acolheu sem hesitar no seu grupo de investigação e que aceitou com grande entusiasmo estabelecer a parceria necessária com a Prof. Dra. Paula Veríssimo para a realização deste trabalho. Agradeço a constante disponibilidade que demonstrava para discutir todo e qualquer tipo de questão e pela prontidão com que se predispunha a responder a todas elas. Providenciou-me uma oportunidade única de aprender imenso sobre nanopartículas e estratégias anti tumorais direcionadas que me enriqueceram bastante em termos curriculares.

De igual modo, não poderia deixar de agradecer a todos os membros dos grupos de investigação da Prof. Doutora. Paula Veríssimo e do Prof. Doutor. Henrique Faneca, que sempre foram espetaculares e incansáveis comigo. Mais em particular, à Dra. Rosemeyre Cordeiro por me acompanhar no desenvolvimento de nanopartículas mesoporosas de síica desde o início deste trabalho, pela disponibilidade que teve para me ajudar em todas as minhas tarefas e por todos almoços passados a falar sobre comida e doçaria no geral. À Mariana, à Flávia e à Dina pela amizade, companheirismo, disponibilidade e espírito de entreajuda que sempre demonstraram. À Dra. Rosário Faro, pela supervisão que me prestou aquando da realização da transformação das estirpes de *E. coli* utilizadas neste trabalho, pela sua simpatia e interesse pelo meu trabalho. À Inês, pela amizade, companhia e imediata disponibilidade para me auxiliar em tudo o que precisasse e para me esclarecer todas as questões. Não posso deixar de agradecer à Prof. Dra. Maria Helena Gil, à Filipa Martins e à Sofia Portugal do

Departamento de Engenharia Química da Universidade de Coimbra pelo acompanhamento, interesse e disponibilidade para que questões relevantes para a realização deste trabalho fossem discutidas e permitissem descobrir e otimizar as metodologias necessárias. Uma palavra especial para a Sofia, que foi incansável comigo.

A título mais pessoal, gostaria de agradecer aos meus colegas de mestrado e filhos do Pai Buda, nomeadamente ao Grilo, à Sara (Jamanta), ao André, à Catarina, à Ema e à Maria Francisca que ajudaram a tornar estes dois anos inesquecíveis! Gostaria também de agradecer às amizades de longa data da terrinha, que me viram crescer e amadurecer enquanto pessoa. Um agradecimento especial à malta do Café Avenida, que em muito contribuíram para animar as minhas noites de sexta e sábado.

"ACoimbrando" agora os agradecimentos, gostaria de começar por agradecer a todos aqueles que me acolheram e integraram em Bioquímica e que se tornaram família, nomeadamente ao Zé Dias, ao Tadeu, à Dani, ao Rui, ao Pedro Ribeiro, ao Areal, ao Tozé, ao Zé Gui, à Gouveia, à Bia, ao Piedade, ao Bidarra, ao Beltrão, à Raquel, à Soraia, enfim, se me estiver a esquecer de alguém, espero que me perdoem. Gostaria também de agradecer a toda a malta da JEST pelas experiências e vivências que partilhámos. O Monstro gostaria de deixar um agradecimento muito grande às suas Belas Paula, Lara e Martinha, pela amizade genuína que surgiu e cresceu na cidade sem ter idade, e que levarei no meu coração para a vida. Foi um gosto e um privilégio ter sido o vosso motorista privado e levo acumulado no meu tecido adiposo abdominal cada ida ao McDonald's. Obrigado por todos os momentos, especialmente pelas noites de Quim Barreiros, Estudantina Universitária de Coimbra e Orxestra Pitagórica. Gostaria de agradecer aos meus 10, aqueles que me escolheram para os orientar e aconselhar desde o início da universidade e que se tornaram parte de mim. Vidal, Patrícia, Magda, Brave, Batista, Juliana, Adriana, Sara, Mila e Feliciano o meu obrigado mais sincero! Quero deixar um reparo mais especial para a Magda por todas as conversas até altas horas, conselhos e sessões de cinema que tivemos. Viver contigo foi sobrenatural! Gostaria também de agradecer a todos os Paulos e Paulas Chorões&Choronas que me acompanham desde o início dos tempos e que são sempre o meu porto de abrigo quando necessito. Abreijos para o Chicória, o Cláudio, o Rocha, o Poiares, o Zé, o Bem-Haja, o Abranches, o Navarro, a Andreia, a Carolina, a Inês Cardoso, a Maleita, a Viegas, a Pedrosa e para a Braga. Sem vocês, não teria sido a mesma coisa!

Não podia deixar de dizer obrigado à Maria João por todo o amor, paciência e atenção que me dá. Com um coração do tamanho do mundo, fez-me voltar a acreditar que é possível confiar totalmente em alguém. Quero poder continuar a contar contigo a meu lado nos desafios que aí vêm. Por último, gostaria de agradecer a toda à minha família por todo o apoio, tupperwares de comida, roupa, “notinhas para gelados” e carinho que me deram. Finalmente, um grande obrigado aos meus “Paitrocínios”. Agradeço ao meu pai pelo esforço que fez para que isto se tornasse uma realidade, és um exemplo de dedicação e de espírito de sacrifício. Obrigado mãe pela força que sempre me transmitiste e por me mostrares que levantar a cabeça após as derrotas é o primeiro passo para que sejamos vitoriosos. Obrigado aos dois pelos valores que me transmitiram e pela educação que me deram. Conseguimos!

A nós, Coimbra!

“Só quem viveu teu sonho te pode encontrar

Nesta chuva de encanto pronta a despertar

São memórias de um tempo que vai terminar

Chega ao fim o Momento de um último olhar”

In Balada do Amanhecer, by Grupo de Fado Amanhecer

Table of Contents

List of Acronyms and Abbreviations

(3-Aminopropyl)triethoxysilane	APTES
(3-Glycidyloxypropyl)trimethoxysilane	GPTS
Ammonia	NH_3
Basic Local Alignment Search Tool (BLAST)	BLAST
Bis[3-(triethoxysilyl)propyl] tetrasulfide	BTESPT
Bovine Serum Albumin	BSA
Cancer Stem Cells	csc
CD44 variant isoforms	CD44v
Cetyltrimethylammonium bromide	CTAB
Class II Helical Cytokine Receptor	hCR
Column volumes	cv
Constraint-based Multiple Alignment Tool	COBALT
Damage Associated Molecular Patterns	DAMPs
Deoxyribonucleic acid	DNA
Dodecyl Sulfate Polyacrylamide Gel Electrophoresis	SDS-PAGE
Dynamic Light Scattering	DLS
Ectodomain	ECD
Enhanced Permeability and Retention	EPR
Epithelial cell adhesion molecule precursor	EpCAM
Epidermal Growth Factor Receptor	EGFR
Escherichia coli	*E. coli*
Ethanol	EtOH
Fourier Transform Infrared Spectroscopy	FTIR
HCC progenitor cells	HcPCs
Hepatocellular Carcinoma	HCC
Hepatocyte Growth Factor	HGF
Human Development Index	HDI
Hyaluronic Acid	HA
Hydrochloric acid	HCl
Hydroxyl group	OH
IFN-Stimulated Response Elements	ISRE
Immobilized Metal Affinity Chromatography	IMAC
Interferon Stimulated Genes	ISGs
Interferons	IFNs
Interferonα-2b	IFNα-2b
Interleukine-6	IL-6
Intracellular domain	ICD
Isoelectric point	pI
Isopropyl β-D-1-thiogalactopyranoside	IPTG
Janus Kinase	JAK
Kanamycin	Kan
Laser Doppler Velocimetry	LDV
Loading Capacity	LC
Loading Efficiency	LE
Luria Broth	LB
Mesoporous Silica Nanoparticles	MSNs
molecular weight	M_w
multidrug resistance	MDR
Multi-Drug Resistance Protein	MRP
N-(3-Dimethylaminopropyl)-N′-ethylcarbodiimide hydrochloride	EDC
N-Hydroxysulfosuccinimide	NHS
Osteopontin	OPN

P-glycoprotein	P-gp
Phosphate-Buffered Saline	PBS
Polyethylene glycol	PEG
Protein Kinase B	Akt
Reticuloendothelial System	RES
Ribonucleic acid	RNA
Signal Transducer and Activator of Transcription	STAT
Sodium Hydroxide	NaOH
Standard CD44	sCD44
Sulphuric acid	H_2SO_4
Tetraethyl Orthosilicate	TEOS
Transmembrane domain	TMD
Transmission Electron Microscopy	TEM
Triethylamine	TEA
Tumour Necrosis Factor	TNF
Tumour-Initiating Cells	TICs
U.S Food & Drug Administration	FDA
World Health Organization	WHO

Abstract

Cancer has rapidly constituted one of the main health concerns of the 21st-century. Conventional chemotherapy strategies are largely used in cancer treatment, but they present low specificity for tumour cells, high toxicity and cause a lot of undesirable side effects. Clinical research has been looking for solutions to address these questions and the recent advantages in the fields of nanotechnology and biotechnology are providing more specific, effective and less toxic solutions at more reasonable financial costs that might revolutionize cancer treatment in a short period of time. The main purpose of this work is the development and characterization of a new drug delivery system with potential application in Hepatocellular Carcinoma treatment. Thus, a mesoporous silica nanoparticle functionalized with hyaluronic acid was developed and loaded with a soluble recombinant human protein, Interferonα-2b (IFNα-2b), whose function is to induce cellular death through apoptotic pathways.

During the development of the mesoporous silica nanoparticles formulation, two approaches for their functionalization with hyaluronic acid were tested. Surface modifications with (3-Glycidyloxypropyl)trimethoxysilane (GPTS) and (3-Aminopropyl)triethoxysilane (APTES) were tested and better results were obtained using APTES. FTIR spectrums of unmodified, modified and functionalized mesoporous silica nanoparticles reveal the characteristic peaks profile expected for each type of nanoparticles and the shifts on the respective zeta potential (ζ-potential) readings confirm the presence of nanoparticles' distinctive chemical groups at their surface. DLS readings also enable determining the average hydrodynamic diameter of mesoporous silica nanoparticles right after its synthesis, modification and functionalization reactions. BL21 Star® cells expressed IFNα-2b and protein's purification by IMAC affinity chromatography was also effective, enabling the collection of pure fractions when a HisTrap HP histidine-tagged protein purification column was eluted with PBS supplemented with 500 mM Imidazole with a purity degree superior to 80%. Finally, following the immersion method, functionalized mesoporous silica nanoparticles were loaded with the produced recombinant protein presenting a loading efficiency of approximately 72%. Nanosystem's loading capacity was found to be of approximately 7.2%.

Keywords: *cancer, Hepatocellular Carcinoma, mesoporous silica nanoparticles, hyaluronic acid, recombinant human Interferonα-2b*

Resumo

O cancro rapidamente se tornou uma das maiores preocupações ao nível da saúde no século XXI. Estratégias convencionais de quimioterapia são frequentemente utilizadas para o tratamento do cancro, mas apresentam baixa especificidade para as células tumorais, elevada toxicidade e causam bastantes efeitos secundários indesejados. A investigação clínica tem vindo a procurar soluções para resolver estas problemáticas e avanços recentes nas áreas da nanotecnologia e da biotecnologia estão a fornecer soluções mais específicas, eficazes e menos tóxicas a preços mais razoáveis que poderão revolucionar o tratamento do cancro num futuro próximo. O principal objetivo deste trabalho é o desenvolvimento e caracterização de um novo sistema de entrega de fármacos com potencial aplicação no tratamento do Hepatocarcinoma Celular. Assim, uma nanopartícula mesoporosa de sílica funcionalizada com ácido hialurónico foi desenvolvida e carregada com uma proteína humana recombinante*, Interferãoα-2b* (IFNα-2b), cuja função é induzir morte celular por vias apoptóticas.

Durante o desenvolvimento da formulação da nanopartícula mesoporosa de sílica, duas abordagens para a sua funcionalização com ácido hialurónico foram testadas. Duas modificações de superfície com (3-Glicidiloxipropil)trimetoxissilano (GPTS) e (3-Aminopropil)trietoxissilano (APTES) foram testadas, tendo-se obtido melhores resultados usando-se APTES. Espetros de FTIR correspondentes a nanopartículas mesoporosa de sílica não modificadas, modificadas e funcionalizadas revelaram o perfil de picos característico esperado para cada tipo de nanopartículas e as alterações nas leituras dos respetivos potenciais zeta confirmaram a presença dos distintos grupos químicos na superfície das nanopartículas. Leituras de DLS também permitiram determinar o diâmetro hidrodinâmico médio das nanopartículas mesoporosa de sílica logo após as suas reações de síntese, modificação e funcionalização. A estirpe BL21 Star® foi utilizada para expressar com sucesso o IFNα-2b e a purificação da mesma por cromatografia de afinidade foi também bem-sucedida, permitindo a recolha de frações puras após eluição da coluna de purificação *HisTrap HP histidine-tagged protein* com PBS suplementado com 500 mM de Imidazol, apresentando um grau de pureza superior a 80%. Finalmente, aplicando-se o método de imersão, nanopartículas mesoporosas de sílica funcionalizadas foram carregadas com a proteína recombinante produzida, apresentando uma eficiência de carregamento de aproximadamente 72%. Determinou-se que a capacidade de carregamento do nanossistema é de aproximadamente 7,2%.

Palavras-chave: *cancro, Carcinoma Hepatocelular, nanopartículas mesoporosas de sílica, ácido hialurónico, Interferãoα-2b humano recombinante*

Chapter I

Introduction

1. Cancer Statistics

Statistical data from 2018 provided by the *Global Cancer Observatory* for *The International Agency for Research on Cancer – World Health Organization* (WHO) – global cancer burden has risen to 18.1 million cases and 9.6 million cancer deaths. Also, it is expected that one-in-five men and one-in-six women worldwide will develop cancer over the course of their lifetime, and that one-in-eight men and one-in-eleven women will die from their disease.

The 2018 data also suggests that countries with a high Human Development Index (HDI) have 2-3 times higher cancer incidence than those with low or medium HDI. Figure 1 represents the global age-standardized incidence rates in 2018 for all cancer, genders and ages and marks the cancer incidence contrast between developed and developing countries.

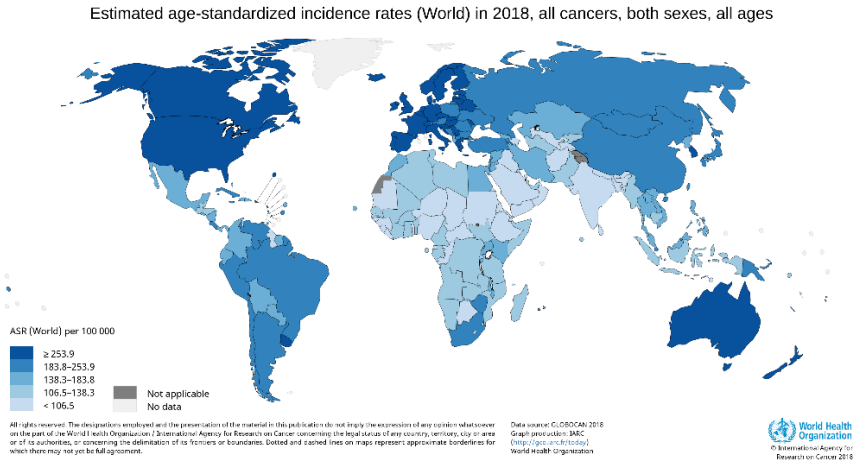

Figure 1 – Global estimated age-standardized cancer incidence rates in 2018 for all types of cancer, genders and ages (reproduced from Observatory, 2018*).*

Population ageing, exposure to cancer risk factors linked to social and economic development, poorer prognosis and limited access to timely diagnosis and treatment are causing an overall increase in the absolute number of cancer cases worldwide. Specifically, cancer incidence is booming in Asia and more than half of all cancer deaths are also located in that continent. Finally, Asia and Africa have a higher proportion of cancer deaths (7.3% and 57.3% respectively) compared with their incidence rates (5.8%

and 48.4% respectively). For a better understanding of the leading cancers' global numbers, cancer incidence and deaths statistics were represented in Figure 2. Lung cancer has the highest incidence rate and is the one that kills the greatest number of people as well. Breast, colorectal, prostate and stomach cancers are the following types of cancer with most incidence rates, but gastrointestinal tract tumours are the ones that are responsible for the greatest number of deaths, including liver cancers.

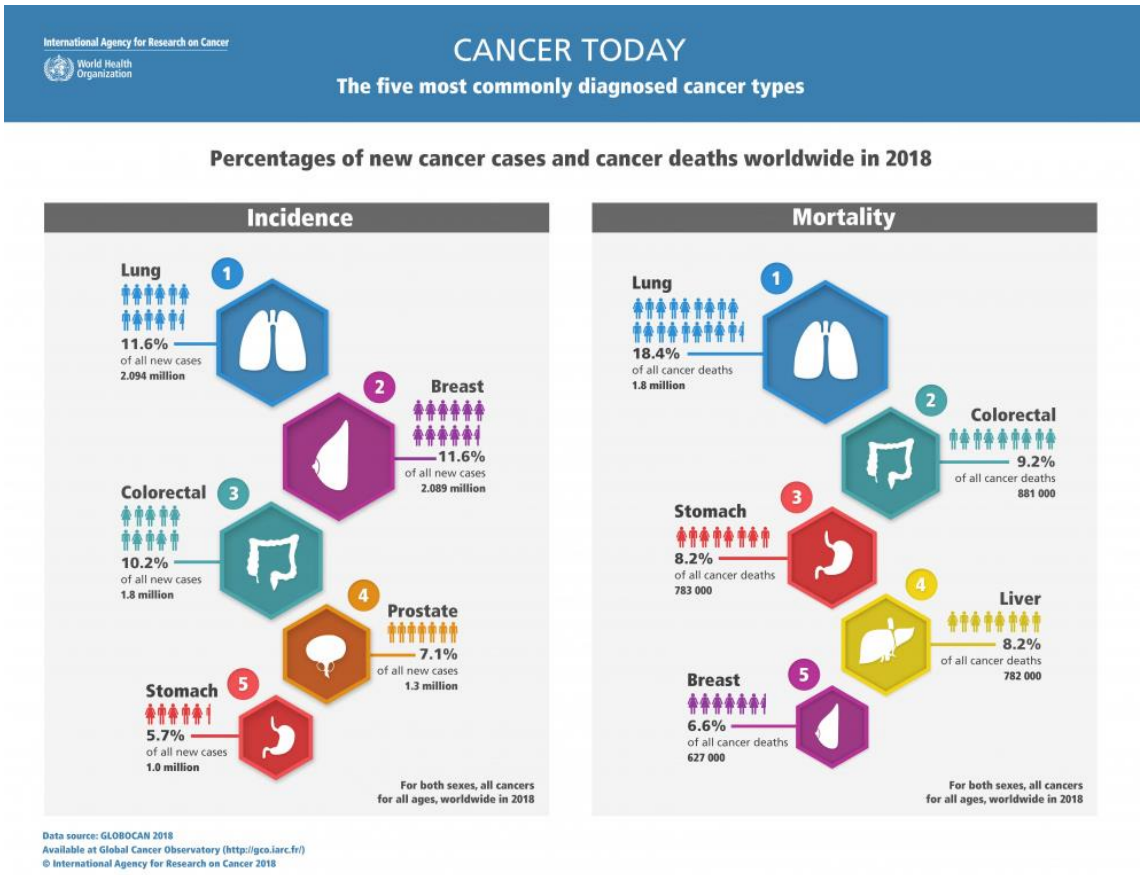

Figure 2 – Statistical analysis of the five most commonly diagnosed cancer types concerning their incidence and mortality rates (reproduced from Observatory, 2018).

2. Cancer and challenges in cancer treatment

Cancer describes a large variety of diseases characterized by unregulated growth of abnormal cells – malignant cells – which have the capacity of invading and spreading to other parts of the organism (International Agency for Research on Cancer, 2008; Senapati *et al.*, 2018). When this occurs, it is commonly said that a primary tumour has metastasized and the accumulation of these malignant cells in other healthy tissues or organs originates secondary tumours that could affect the therapy strategy or its efficiency (Gupta and Massagué, 2006; Valastyan, S, Weinberg, 2011; Xiwei Zheng, Cong Bi, Marissa Brooks, 2015; Parkins *et al.*, 2018; W. Li *et al.*, 2018).

Tumour biology is becoming best understood and recent advantages in diagnostic strategies and cancer treatment may help decreasing cancer mortality rate in a near future. (Senapati *et al.*, 2018). Conventional therapeutic approaches to cancer treatment comprise the use of chemotherapy, radiotherapy and surgery or to the combination of these three strategies. The aim regarding conventional chemotherapy is primarily to interfere with DNA and protein synthesis and with the mitotic process of cancer cells causing its death, with limited success. Nevertheless, the drugs used in this strategy also cause cytotoxicity in healthy cells, originating undesirable side effects. Thus, alongside with other anticancer therapeutic strategies described earlier, conventional chemotherapy is very invasive to the patient and presents other associated disadvantages, such as low bioavailability of the drugs used, requirement of high doses to achieve the desired therapeutic effect, low therapeutic indexes and development of drug resistance (Senapati *et al.*, 2018).

Therapies for cancer treatment might be dramatically revolutionized in the next decade due to the current development of new drug delivery nanosystems. Scientific research in this area is focused on the molecular targeting of cancer that might improve therapeutic indexes. Future anticancer strategies might consider the detection of malignant cells and verify its location in the organism using *in vivo* real-time imaging while killing cancer cells and sparing the healthy ones and monitoring the process data in real time. Targeting the anticancer drug for cancer cells is the key to the minimization of undesirable side effects and there are different strategies to achieve that goal, such as drug rational design, drug controlled and/or sustained release (Mi *et al.*, 2015, 2017; Senapati *et al.*, 2018).

3. Nanoparticles as drug nanocarriers in cancer treatment

Nanoparticles are constituted by its core together with the surrounding layer, establishing its size between 1-100 nm (IUPAC, 1997). Generally, a nanoparticle is defined as a small object that behaves as one unit concerning its transportation and physicochemical properties (Dahirel and Jardat, 2010; Kotov, 2010; Batista, Larson and Kotov, 2015).

Thus, nanoparticles present an enormous biomedical potential. Due to its reduced size and high surface area/volume ratio, they can be drug nanocarriers with the capacity of binding, absorbing and transporting a diverse range of biomolecules such as DNA, RNA and proteins. Associated magnetic properties grant another characteristic to nanoparticles, allowing them to also be high-efficiency imaging agents (Shen, Wu and

Chen, 2017; Nicholas H. Farina *et al.*, 2018; Senapati *et al.*, 2018). The combination of therapy and diagnostic capacity in a single nanoparticle originated a recent research field called theragnostic, where nanoparticles and specific chemical groups are synthesized and conjugated according to the intended modality for the nanoparticle (De Rosales, 2014; Shen, Wu and Chen, 2017).

Using nanoparticles as drug carriers also allow the application of adjuvant therapies that require a spatially and temporally controlled use of several drugs. This is not feasible with conventional chemotherapy strategies due to the associated low bioavailability, undesirable side effects and high dose requirements for achieving good therapeutic indexes. Therefore, considering all the potentialities concerning nanoparticles as drug nanocarriers is safe to assume that they normalize pharmacokinetic and pharmacodynamic parameters of therapeutic agents, improving the efficiency of the associated therapy and mitigating the disadvantages of conventional chemotherapy (Olov, Bagheri-khoulenjani and Mirzadeh, 2018). Ultimately, nanotechnology progress is essential to the development of nanomaterials that can have biomedical relevance in targeted drug delivery (Lokina *et al.*, 2014; Wolfbeis, 2015; Rajendran *et al.*, 2016; Senapati *et al.*, 2018).

4. Organic and Inorganic Nanocarriers

Organic nanocarriers are vehicles that use organic molecules as a major building block material. Depending on their composition, they might be characterized as solid, biocompatible, colloidal and often biodegradable systems within nanoscale dimensions. These nanocarriers are one of the simplest forms of soft materials for nanomedicine applications. They are simply synthesized and post-synthetic modifications are easily applied to achieve the desired properties (Olov, Bagheri-khoulenjani and Mirzadeh, 2018; Senapati *et al.*, 2018).

Drugs are easily encapsulated in typical conditions using hydrophilic or hydrophobic solvents either through dispersion in the polymer matrix or by conjugation to polymer molecules. The purpose of this encapsulation process is to achieve a controlled drug delivery through surface or bulk erosion, diffusion through the polymer matrix, swelling followed by diffusion or as a response to local stimuli. Some polymers have the advantage of sustained release over a period of days to several weeks (Senapati *et al.*, 2018). Multiple organic nanocarriers have been studied for drug delivery in cancer treatment and the most relevant ones are liposomes, protein-based nanocarriers, micelles, dendrimers, molecular self-assembly, supramolecules and

hydrogels (Nicholas H. Farina *et al.*, 2018; Olov, Bagheri-khoulenjani and Mirzadeh, 2018; Senapati *et al.*, 2018).

Inorganic nanocarriers are vehicles that use inorganic elements as a major building block material. They offer great advantages related to therapeutic and imaging treatments, mostly due to their large surface area, better drug loading capacity and bioavailability and controlled drug release. Also, they have great tolerance towards most organic solvents, unlike polymer-based nanoparticles (Olov, Bagheri-khoulenjani and Mirzadeh, 2018; Senapati *et al.*, 2018). In spite of their general lower toxicity issues, they always must be considered. (Olov, Bagheri-khoulenjani and Mirzadeh, 2018). In cancer treatment, quantum dots, carbon nanotubes, fullerenes, layered double hydroxides, mesoporous silica, metallic nanoparticles and magnetic nanoparticles are the most relevant nanoparticles acting as inorganic nanocarriers (Nicholas H. Farina *et al.*, 2018; Olov, Bagheri-khoulenjani and Mirzadeh, 2018; Senapati *et al.*, 2018).

5. Properties of Nanocarriers

In cancer therapy, an organic or inorganic nanocarrier must be selected due to tumour specificity and the associated material advantages (Chen *et al.*, 2018; Senapati *et al.*, 2018). The nanoparticle size is a major determining factor in circulation time, biodistribution and cellular uptake. In clinical applications, its total diameter often varies from 5-200 nm (Nicholas H. Farina *et al.*, 2018) instead of 1-100 nm, as described earlier (Batista, Larson and Kotov, 2015). The nanocarrier delivery system should be modulated considering its surface charge and chemistry, size, shape dispersity, hydrophobicity and biodegradability (Chen *et al.*, 2018; Nicholas H. Farina *et al.*, 2018). Studying the conjugation of these characteristics enables the determination of the biocompatibility of the nanocarrier. In Figure 3 is shown the influence of some physicochemical parameters related to the biocompatibility of Nanoparticles.

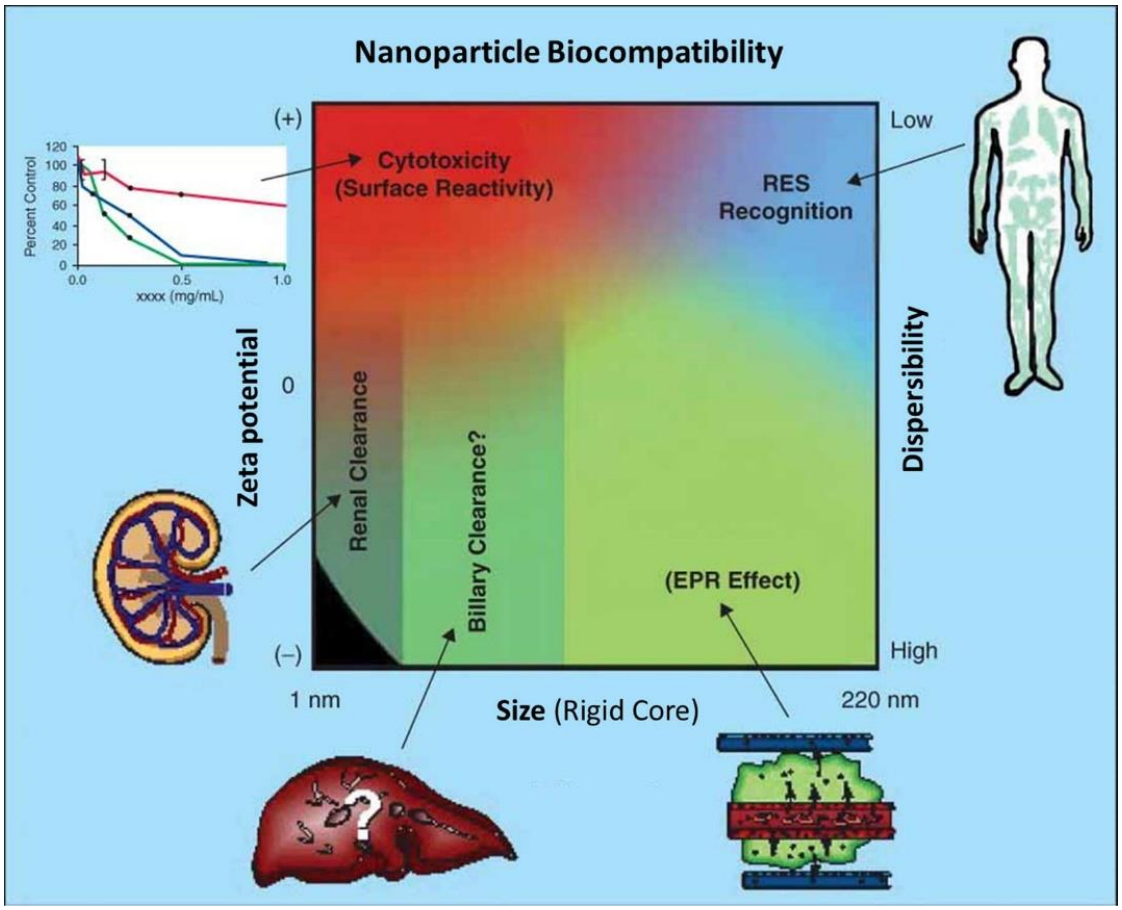

Figure 3 – Influence of physicochemical parameters (effect of size, zeta potential and dispersibility) in Nanoparticles biocompatibility features and qualitative trends in relationships between the independent variables described earlier with the EPR effect and clearance (shown in different shades of green), cytotoxicity (shown in red) and RES recognition (shown in blue). Reproduced from (Chen *et al.*, 2018).

Considering the size of the nanoparticle, if its rigid core diameter is smaller than 8 nm, the nanoparticle will be swiftly removed by the kidneys. (Chen *et al.*, 2018; Zhou, Quan, Wu, Zhang and Niu, 2018). However, larger nanoparticles with a diameter between 30-200 nm can accumulate in tumour tissues due to Enhanced Permeability and Retention Effect – EPR Effect (Chen *et al.*, 2018).

The surface properties of nanoparticles are crucial to its biocompatibility features because chemical surface alterations might change the hydrodynamic size and surface charge of the Nanoparticle. Ultimately, its reactivity will also be affected (Chen *et al.*, 2018). Thus, Nanoparticles with positive surface charge (represented by a positive zeta potential) usually are more toxic than the ones with the negative surface charge because they promote haemolysis and platelet aggregation. Also, they have shorter circulation half-lives than negative and neutral ones. Hydrophobic Nanoparticles will be rapidly cleared by the Reticuloendothelial System – RES system (Chen *et al.*, 2018).

6. Silica nanoparticles for drug delivery in cancer treatment

Silica nanoparticles include a large range of drug nanocarriers often classified as inorganic materials (Chen *et al.*, 2018; Zhou, Quan, Wu, Zhang, Niu, *et al.*, 2018). Their easily modifiable chemistry allows the creation of nanoparticles with a diverse range of shapes, sizes and surface properties. Considering also their known biocompatibility, lower toxicity, good biodistribution and efficient excretion through urine and/or faeces, silica nanoparticles are gaining biomedical interest because they can provide specific and controlled drug delivery for cancer treatment, allowing the improvement of therapeutic strategies (Chen *et al.*, 2018; Nicholas H Farina *et al.*, 2018; Zhou, Quan, Wu, Zhang and Niu, 2018).

The first examples of silica nanoparticles are solid spheres and their synthesis, performed by Kolbe, goes back to 1956. Then they were improved by Werner Stöber, Arthur Fink and Ernst Bohn in 1968 (Chen *et al.*, 2018). In 1992, *Mobil* corporation scientists introduce *mesoporous silica nanoparticles* (MSNs) and originate an explosion in the variety of silica nanoparticles (Chen *et al.*, 2018; Zhou, Quan, Wu, Zhang, Niu, *et al.*, 2018). Alongside with mesoporous particles, mesoporous hollow spheres, rattled-type spheres, foam-like nanoparticles, nanotubes and mesoporous red blood cell-shaped nanoparticles are examples of this new wave of interest in Silica Nanoparticles (Chen *et al.*, 2018).

7. Mesoporous Silica Nanoparticles as Drug Nanocarriers

Mesoporous silica nanoparticles are one type of nanocarrier constituted by amorphous silica. They are formed by a rigid structure that provides a permanent, long-range and uniform porosity of intermediate size, comprised between 2 nm and 50 nm (IUPAC, 1997). This is essential to act as a reservoir for a large range of compounds or biomolecules and also enables its controlled and specific delivery into the therapeutic target (Nicholas H Farina *et al.*, 2018; Zhou, Quan, Wu, Zhang, Niu, *et al.*, 2018). They present low *in vivo* toxicity, proper degradation in body fluid context and excretion through urine and faeces, indicating good biocompatibility (Q. He *et al.*, 2010; Liu *et al.*, 2011; Fu *et al.*, 2013; Zhou, Quan, Wu, Zhang, Niu, *et al.*, 2018). These nanoparticles have interesting structural properties and unique features for biomedical application, making them excellent candidates for controlled drug/gene delivery systems (Zhou, Quan, Wu, Zhang, Niu, *et al.*, 2018).

Their long-range, ordered porous structure without interconnection between individual porous channels allows good control of the drug loading and release kinetics.

The pore volume and surface area of MSNs are usually above 1cm^3/g and 700m^2/g, respectively, promoting drug loading and enhancing dissolution processes (Zhou, Quan, Wu, Zhang, Niu, *et al.*, 2018). The total diameter of this type of nanocarrier can be controlled from 50 to 300 nm to facilitate endocytosis process performed by living cells (Zhou, Quan, Wu, Zhang, Niu, *et al.*, 2018). A study demonstrates that the size of MSNs is a key factor for its retention in the living tissues. Larger MSNs (200-360 nm) accumulate preferentially in the liver and spleen, but they can also be found in the lungs, kidneys and heart. Smaller MSNs (80-120 nm) avoid accumulation in these organs and suffer slower biodegradation due to poor biodistribution (He *et al.*, 2011; Nicholas H Farina *et al.*, 2018).

When MSNs have long residence times and suffer biodegradation, they are transformed into orthosilic acid. After this metabolization process, the orthosilic acid is eliminated via renal excretion (Rosenholm *et al.*, 2012; Nicholas H Farina *et al.*, 2018). Highly cationic MSNs rapidly experience hepatobiliary excretion (Nicholas H Farina *et al.*, 2018). Also, MSNs have two functional surfaces: the cylindrical porous surface and the exterior particle surface. These silanol-contained surfaces can be selectively functionalized to enhance control over hydrophobic or hydrophilic drug loading and its release. The external surface can be conjugated with targeting ligands for efficient cell-specific drug delivery (X. Li *et al.*, 2018; Zhou, Quan, Wu, Zhang, Niu, *et al.*, 2018). These Silica Nanoparticles penetrate the cells through endocytosis processes. After cellular internalization, they are transported to large vesicular endosomes that will fuse with lysosomes. Their membranes are eventually disrupted, and the MSNs accumulate in cell cytoplasm without reaching the cell nucleus. MSNs cell uptake and trafficking can be monitored recurring to confocal microscopy using stained cells and fluorescently labelled nanocarriers (Zhou, Quan, Wu, Zhang, Niu, *et al.*, 2018).

Finally, MSNs can overcome multidrug resistance (MDR) mainly because the energy-dependent endocytosis of MSNs can bypass the drug efflux pumps, such as P-glycoprotein (P-gp) and Multi-Drug Resistance Protein (MRP1). Also, the possibility of co-delivery using MSNs to overcome MDR should be considered because efflux pump blockers or nucleic acids which silent its expression can be simultaneously delivered alongside with the anticancer drug. Nucleic acids can also be co-delivered to overcome MDR due to their ability to silence the antiapoptotic protein gene BCL2, involved in nom-pump MDR events (Zhou, Quan, Wu, Zhang, Niu, *et al.*, 2018).

8. Methodologies applied in MSNs synthesis

Silica Nanoparticles can be synthesized following two different approaches: *bottom-up* and *top-down* methods. *Bottom-up* methods usually involve catalysed hydrolysis and condensation of silica sources. They are the most used methods due to its simplicity, safety and because they allow the obtention of MSNs with multiple morphologies. On the other hand, *Top-down* methods are more hazardous and difficult to implement. The diameter range of the MSNs is restricted to 5-50 nm and the electrochemical etching required (performed by highly corrosive acids) originates stand-free films, that with later sonication and oxidation processes originate an irregular 2D porous structure. This structure morphology is also poorly adjustable and temperatures above 1500ºC are required in *Top-down* synthesis (Chen *et al.*, 2018).

Bottom-up methods often require a silica source, a basic catalyst, templates and an aqueous/organic-based solvent. The modified *Stöber Process* is the most commonly applied methodology in MSNs synthesis. This method can be adjusted and modified accordingly specific situations. The most commonly used reagents in this method are described in Table 1 (Chen *et al.*, 2018; Meier *et al.*, 2018).

Table 1 – Description of the chemical requirements for the synthesis of MSNs and specification of the reagents commonly used in Stöber Process and in a modified *Stöber Process* (Chen *et al.*, 2018; Meier *et al.*, 2018).

Chemical Requirements	**Reagent Specification**
Silica Source	Tetraethyl Orthosilicate (TEOS)
Organic Solvent	Denatured Ethanol (≥99.8%)
Co-Solvent	De-mineralized water
Basic Catalyst	Ammonia Ethanolamine
Templates	Surfactants Cells
Co-Precursors	Aminopropyl-trimethoxysilane Mercaptopropyl-methoxylane

The synthetic process represented in Figure 4 starts with the mixing of a silica precursor, such as TEOS, with an organic solvent, a co-solvent, a basic catalyst and a surfactant, such as cetyltrimethylammonium bromide (CTAB) (Hadipour Moghaddam *et al.*, 2017), in a reaction tube. There, the TEOS solubility in the alcohol is enhanced by the water and originates a silanol. Then, it is hydrolysed in silicate species and ethanol is also obtained. Following this step, the silanol condenses and form the Si–O–Si bridges. Co-precursors like Bis[3-(triethoxysilyl)propyl] tetrasulfide (BTESPT) can be used to promote the introduction of functional groups in the MSNs surface (Chen *et al.*, 2018; Meier *et al.*, 2018). Pore induction can be accomplished by removing surfactant's micelles with acidic ethanol (Hadipour Moghaddam *et al.*, 2017).

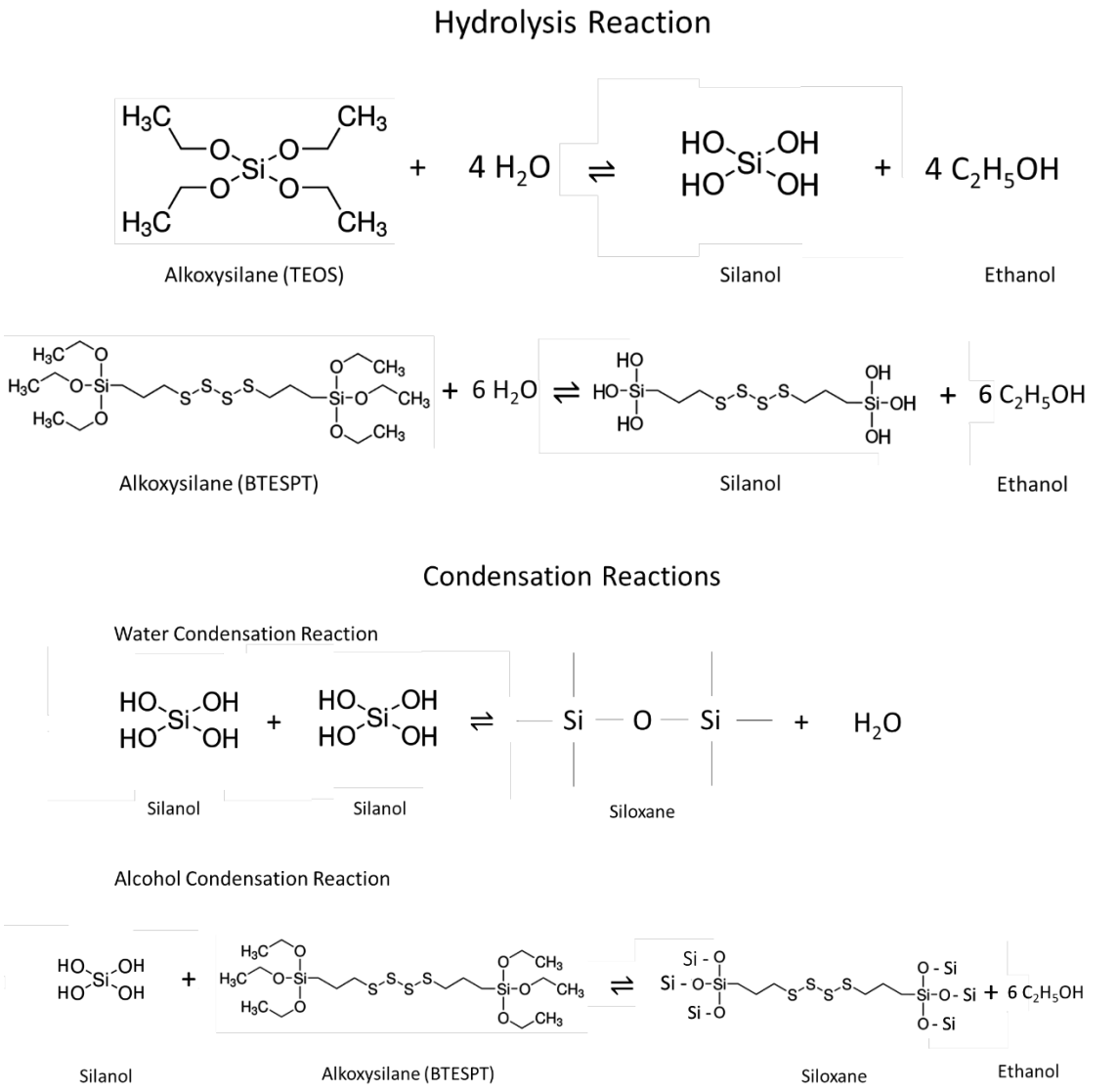

Figure 4 – Representation of the hydrolysis and condensation reactions occurring during the formation of silica nanoparticles.

The hydrolysis and condensation processes are modulated according to the acidic/basic character of the catalyst. Basic catalysts are more commonly used because polymerization and condensation processes allow a more easily obtention of homogenous silica products. However, when the synthesis is performed under lower pH conditions, the hydrolyzation and precipitation of silica particles are faster, but more ploy-disperse (Chen *et al.*, 2018).

Usually, this method is performed at room temperature (25ºC) and at atmospheric pressure. Under these conditions, the smallest silica nanoparticles structurally considered well-formed have approximately 100 nm and the current scientific trend is to obtain smaller silica nanoparticles (see Figure 5). Thus, studies are showing that higher synthesis temperatures could solve the issue, but challenges related to physicochemical parameters of the reagents required for this synthesis arise. However, modifications done in the *Stöber Process* are pointing to promising results, mainly the increase of synthesis temperature, (Meier *et al.*, 2018). Ultimately, the pore size is determined by the surfactant and other templates. Bigger molecule cargos can be stored in the pore if its diameter is increased with the use of a pore expanding agent, like 1,3,5-trimethylbenzene (Zhao *et al.*, 1998; Chen *et al.*, 2018).

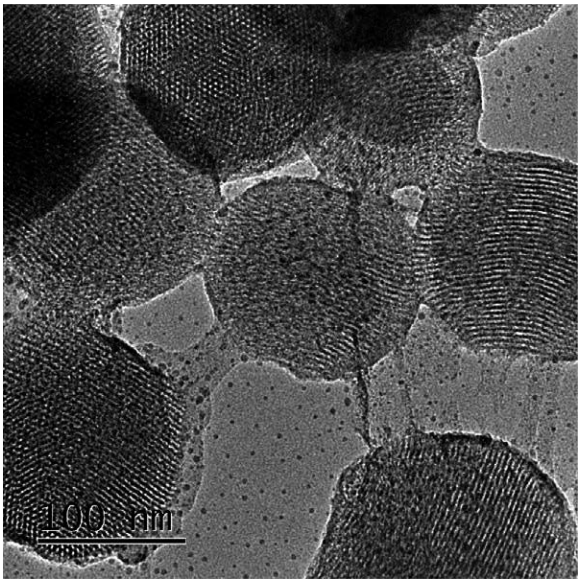

Figure 5 – The microscopic image of MSNs obtained with Transmission Electron Microscopy (TEM). Individual MSNs have a well-defined spherical shape which diameters can present different sizes, although none of them is smaller than 100 nm (reproduced from Zhou, Quan, Wu, Zhang, Niu, et al. 2018).

9. Surface modification and functionalization of MSNs

Colloidal silica nanoparticles have a high degree of hydroxyl groups in its surface that facilitate the modification of the MSNs with a diverse range of silane reagents that allow the introduction of other functional groups onto the two modifiable surfaces (Chen *et al.*, 2018).The modification of MSNs can occur chemically through covalent bonding and the linkage established is irreversible. Also, the modification can occur physically through physisorption and unlike the previous modification type, this one is reversible due to the instability of the non-covalent bonding process (Chen *et al.*, 2018). The chemical nature of MSNs presents a high degree of similarity to silica glass and the same chemistry used to perform modifications in glass can be applied (Nicholas H Farina *et al.*, 2018).

The modified surface of the MSNs can be functionalized with numerous surface groups that confer relevant and specific properties to biomedical applications (Chen *et al.*, 2018; Nicholas H Farina *et al.*, 2018; Zhou, Quan, Wu, Zhang, Niu, *et al.*, 2018). Polyethylene glycol (PEG) is the traditional polymer used for MSNs functionalization (PEGylation) (Ma *et al.*, 2012a) because when vectorized causes an increase in particle delivery to tumour cells, resulting in the improvement of the uptake mechanism (Nicholas H Farina *et al.*, 2018; Zhou, Quan, Wu, Zhang, Niu, *et al.*, 2018). PEGylation also reduces nanoparticle's intracellular aggregation and macrophage uptake, increasing their circulation times (Chen *et al.*, 2018; Nicholas H Farina *et al.*, 2018). Preferably, PEGylated MSNs accumulate in acidic organelles, such as mitochondria, lysosomes, some elements of the endoplasmic reticulum, endosomes and Golgi apparatus (Oba-yabana *et al.*, 2018; Zhou, Quan, Wu, Zhang, Niu, *et al.*, 2018). Organic acids like folic acid, or polymeric chains of organic acids such as hyaluronic acid, whose receptors are over-expressed on the surface of cancer cells (Zhou, Quan, Wu, Zhang, Niu, *et al.*, 2018) can promote active targeting therapies. This therapeutic strategy directs the functionalized MSNs to cancer cells and reduces its endocytosis by healthy cells (Ma *et al.*, 2012a; Zhou, Quan, Wu, Zhang, Niu, *et al.*, 2018).

Figure 6 summarizes the diversity of chemical groups that can be attached to the modified surfaces. This enhances the multimodal characteristics of MSNs and the potentialities for the development of new generation cancer therapies based on these systems (Chen *et al.*, 2018; Nicholas H Farina *et al.*, 2018; Zhou, Quan, Wu, Zhang, Niu, *et al.*, 2018).

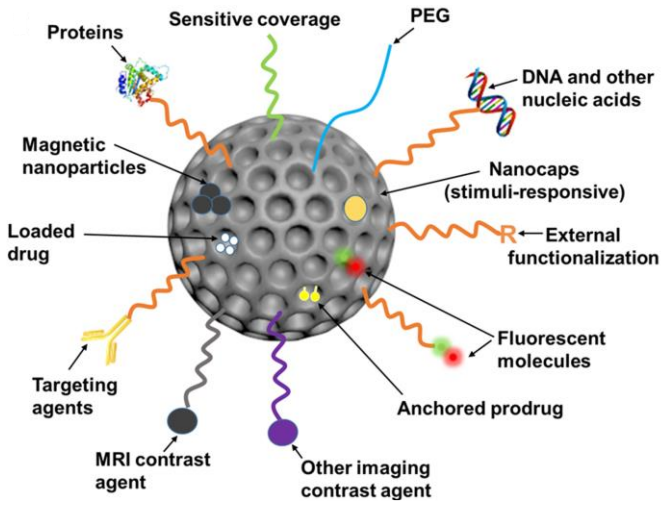

Figure 6 – Representation of MSNs multifunctionality and the major possibilities for hypothetical functionalizations to be applied in future therapeutical approaches (reproduced from Chen *et al.*, 2018*).*

10. MSNs conjugated with Hyaluronic Acid

Hyaluronic acid (HA), whose structure is represented in Figure 7, is a non-sulphated glycosaminoglycan composed by alternating units of beta-*1,3-N-acetyl*glucosamine and beta-1,4-glucuronic acids (Ma *et al.*, 2012a; Zhang *et al.*, 2014a). This acid locates preferably in the extracellular matrix of normal tissues and presents good biocompatibility and viscoelastic properties, as well as a non-immunogenic character (Ma *et al.*, 2012a; Zhang *et al.*, 2014a). Its levels are regulated by hyaluronidase and structural modifications and/or crosslinks reactions that could protect HA from enzymatic degradation (Zhang *et al.*, 2014a). This molecule has enhanced hydrophilic character which prevents its direct conjugation with hydrophobic polymers, drug molecules or lipids (Ma *et al.*, 2012a).

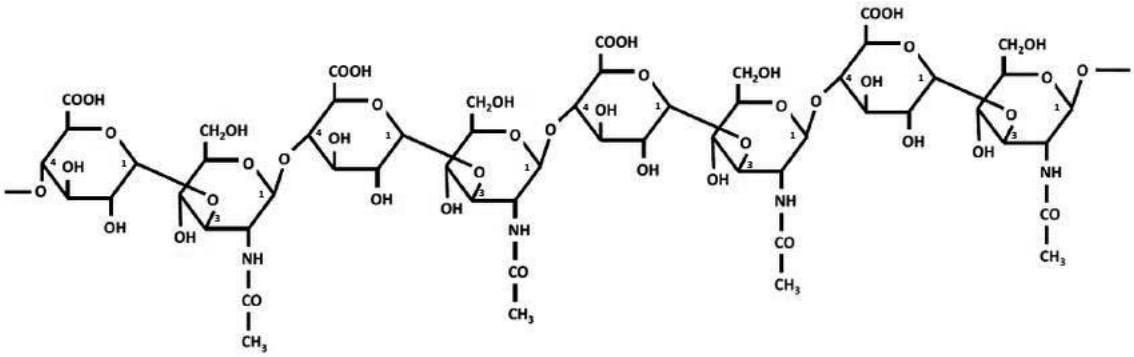

*Figure 7 – Representation of the chemical structure of HA, which is composed of beta-*1,3-N-acetyl*glucosamine acid and beta-1,4-glucuronic acid. The number of the carbons involved in β → (1,3) linkage and β → (1,4) linkage are pointed in the image (adapted from Lennon and Singleton 2011).*

MSNs and HA can be conjugated through an amidation reaction resulting in a specific inorganic/organic hybrid drug delivery system (MSNs-HA) which synergistically combines the advantages of MSNs and HA. Not only HA improves dispersity of MSNs in physiological solution but also enhances the tumour selectivity due to its potential to act as a targeting biological molecule (Ma *et al.*, 2012a). HA selectively binds to the receptor CD44, triggering an endocytosis process defined as HA-receptor mediated endocytosis route (Ma *et al.*, 2012a; Zhou, Quan, Wu, Zhang, Niu, *et al.*, 2018).

11. CD44 Receptor

CD44 is a ubiquitous transmembrane glycoprotein, also known as P-glycoprotein 1, expressed in healthy cells but over-expressed in cancer cells of all types of tumours (Ma *et al.*, 2012a; Senbanjo and Chellaiah, 2017). This receptor is constituted by an extracellular domain, also known as ectodomain, a transmembrane domain and an intercellular domain, otherwise called intracellular domain. The ectodomain (CD44-ECD) senses the extracellular stimulus, which depends on the extracellular microenvironment (Williams *et al.*, 2013; Senbanjo and Chellaiah, 2017). The transmembrane domain (CD44-TMD) allows the interaction with co-factors and adaptor proteins as well as directs lymphocyte homing (Williams *et al.*, 2013; Senbanjo and Chellaiah, 2017). Finally, the intracellular domain (CD44-ICD) is capable of executing a translocation into the nucleus, regulating gene transcriptional processes (Williams *et al.*, 2013; Senbanjo and Chellaiah, 2017). The conserved form of this receptor is defined as standard CD44 (sCD44) and its weight varies between 85-90 kDa, while a diverse range of larger variant isoforms (CD44v) may also occur (Senbanjo and Chellaiah, 2017).

In healthy cells, this multifunctional receptor is involved in the regulation of HA metabolism, activation of lymphocytes and the release of cytokines. CD44 loss causes the disruption of HA metabolism, cellular healing in wounds and keratinocyte proliferation. However, in cancer cells, its over-expression leads to cancer dissemination and metastasis, being the expression of vCD44 often associated, suggesting that this receptor intervene in tumour progression improving its adhesion and enhancing the survival of cancer cells (Williams *et al.*, 2013; Senbanjo and Chellaiah, 2017).

Figure 8 represents the mechanistic behaviour of CD44, which involves all the domains of this receptor, and a larger variant isoform of CD44. Considering sCD44, its CD44-ECD is cleaved by membrane type 1 matrix metalloprotease (M1-MMP) and then presenilin-1/γ secretase, induced by binding of ligands, such as HA or osteopontin (OPN), cleaves the CD44-TMD. Fragments from both domains are released and the

CD44-ICD is translocated into the nucleus and activates transcription genes important in metastasis and cell survival, such as MMP-9, NOTCH1 and RANKL (Thorne, Legg and Isacke, 2004; Senbanjo and Chellaiah, 2017).

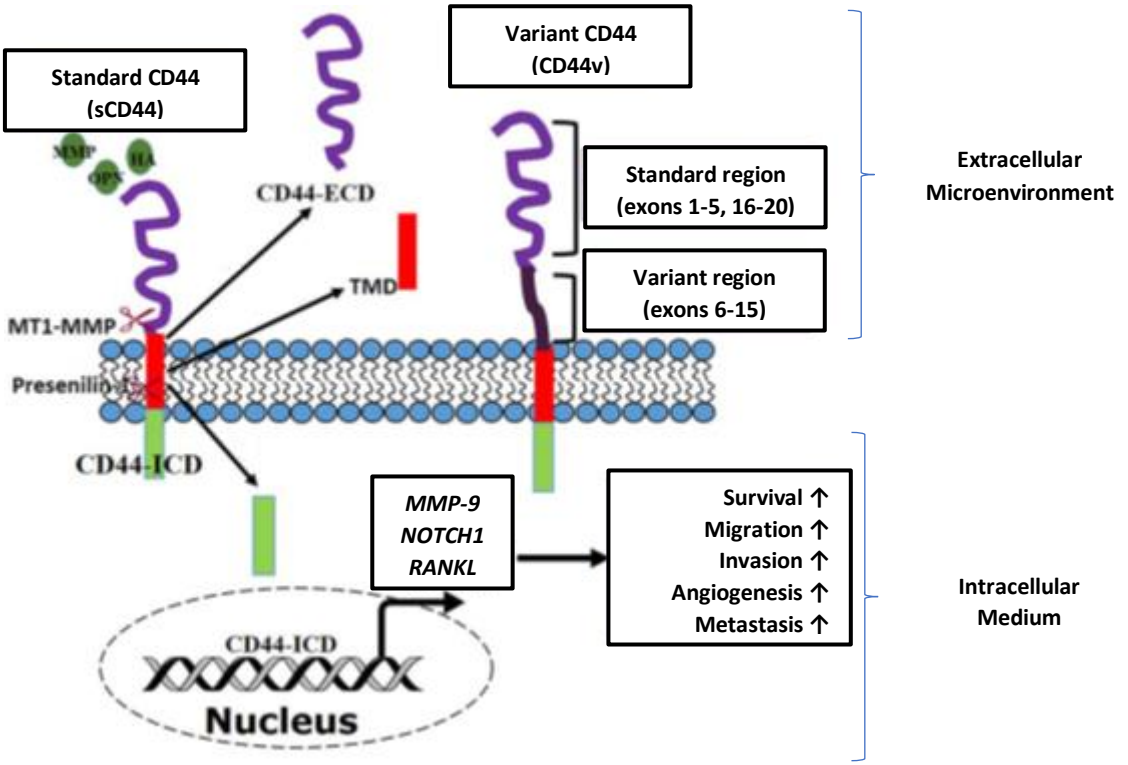

Figure 8 – Scheme of the mechanism involving a sCD44 transmembrane receptor and the effect of sCD44-ICD in the enhanced expression of genes relevant to cell survival and metastasis process. General representation of a vCD44, a larger CD44 transmembrane receptor, constituted by its standard and variant regions (adapted from Senbanjo and Chellaiah 2017 and Thorne, Legg and Isacke, 2004).

As a matter of fact, CD44 performs a dual role in the progression of tumours. Its role as a transcriptional factor and its mechanistic properties were already described. Nevertheless, the translocational movement of CD44-ICD into the nucleus causes its binding to a novel promoter response element and a transcriptional regulation is triggered, favouring the expression of genes involved in cell survival under conditions of stress, inflammation, oxidative glycolysis and tumour invasion. Also, this translocation movement performed by CD44-ICD might suggest an interaction with stemness factors (Senbanjo and Chellaiah, 2017).

Likewise, CD44 also performs a role in tumour invasion and angiogenesis. The special organization of CD44 at the cell surface could modulate the structure of the pericellular matrix dependent on the HA scaffold. Thus, any alteration in this matrix and in its adhesive structures, including CD44, will physiologically affect the actin cytoskeleton and the nucleus due to their dynamic regulation, resulting in alterations in

cell shape, intracellular signalling and gene expression, essential to tumour invasion capacity (Williams *et al.*, 2013; Senbanjo and Chellaiah, 2017). Particularly, the expression of CD44v3, CD44v6 and CD44v10 allows the binding of Hepatocyte Growth Factor (HGF) to c-Met in its ectodomain, resulting in the formation of the CD44v6/HGF/c-Met complex and in the activation of c-Met, MEK and ERK signalling to promote the migration and invasion of Cancer Stem Cells (CSC) (Williams *et al.*, 2013). Angiogenesis is also under the influence of sCD44 and CD44v expression and the conjugation of this factor together with an increase in microvessel number might constitute a diagnostic marker (Senbanjo and Chellaiah, 2017). Metastasis formation is linked to a more pronounced vascular CD44 expression, which is enhanced by the production of angiogenic factors by cancer cells that will lead to the formation of new blood vessels and facilitate the binding process of this cells to this new vasculature. This favours the extravasation of tumour cells through this blood vessel that also present receptors for endothelial growth factors, heparin-binding basic fibroblasts growth factor and heparin-binding epidermal growth factor (Senbanjo and Chellaiah, 2017).

Therefore, CD44 is involved in reprogramming cells to exhibit a more stem cell-like phenotype and might be essential to promote tumour progression and chemoresistance. Considering the similarities and differences between sCD44 and CD44v function new therapeutic strategies might be developed to metastatic cancer (Williams *et al.*, 2013).

12. CD44 Receptor and Hepatocellular Carcinoma

Hepatocellular Carcinoma (HCC) is the most common type of liver cancer and one of the deadliest known cancers. The post-surgical 5-year survival rate remains low and this situation is associated with a high recurrence rate caused by intrahepatic and distant metastasis (Hou *et al.*, 2011; Qiu *et al.*, 2016). HCC development is highly related to chronic liver damage, inflammation and a high-fat diet. This tumour is resulting from fully differentiated and rarely dividing epithelial cells and pericentral hepatocytes originating from differentiated zone 3, represented in Figure 9 (Dhar *et al.*, 2018).

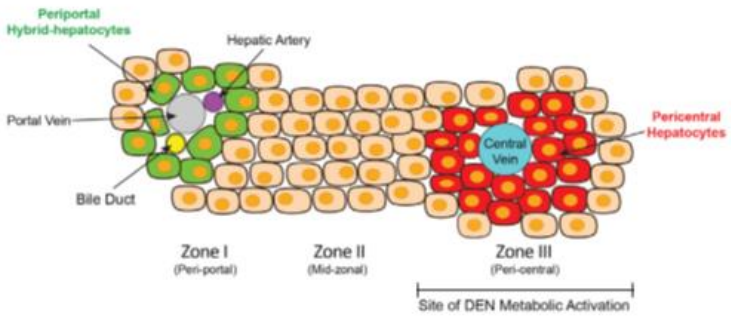

Figure 9 – Histological representation of liver anatomy relevant for HCC study, in which three metabolic zones and its major vessels, ducts and types of hepatocytes are identified (reproduced from Dhar et al., 2018).

HCC cancer cells are known for its metastatic character. They undergo Hematogenous Dissemination through the formation of tumour thrombi in the portal or hepatic veins (also represented in Figure 6) and secondary tumours are formed in distant parts of the organism, decreasing the survival chances of patients diagnosed with malignant HCC (Hou *et al.*, 2011; Dhar *et al.*, 2018). This condition is caused by a small population of tumour cells capable of promoting and sustaining tumour formation and growth, also known as Tumour-Initiating Cells (TICs). TICS allow the growth of tumour cells from extremely small numbers, resulting in the formation of tumour bulk. Their main markers are CD133 and CD44 receptors and combined or alternated decreased expression of both receptors suppress the formation of metastasis. The over-expression of both receptors leads to the appearance of tumours in healthy tissues (Hou *et al.*, 2011). Thus, the CD44 receptor is involved in human HCC initiation and is one of the markers for this cancer detection because of its upregulation, as well as CD24, CD90, and CD133 receptors and EpCAM (Epithelial cell adhesion molecule precursor) (Dhar *et al.*, 2018). CD44 not only can bind HA, OPN, collagen and fibronectin but also can serve as a coreceptor for growth factor receptors, such as the over-expressed Epidermal Growth Factor Receptor (EGFR) and c-Met. Also, CD44 participates in nuclear factor (NF)-κB and STAT3 activation and the presence of standard and variant isoforms of CD44, such as CD44v6, are associated with HCC (Hou *et al.*, 2011; Dhar *et al.*, 2018; Zhou, Quan, Wu, Zhang, Niu, *et al.*, 2018).

The critical step for HCC initiation is hepatocyte proliferation. In normal conditions, damaged hepatocytes release Damage Associated Molecular Patterns (DAMPs) that will contact liver macrophages. These liver macrophages will produce mitogens that will promote hepatocyte proliferation required for damage repair and liver mass maintenance (Dhar *et al.*, 2018). However, this compensatory response is only effective for a few cycles of cell division and under carcinogenic insult, differentiated

hepatocytes could be converted in HCC progenitor cells (HcPCs) that will be unable to trigger apoptotic death or cell cycle withdrawal of DNA-damaged cells (Dhar *et al.*, 2018).

The molecular circuit of HCC initiation is represented in Figure 10. When DNA damage or stress occurs in Pericentral Hepatocytes, stress-induced kinases activate and stabilize p53 protein through phosphorylation that will also induce its inhibitor, Mdm2 (Aubrey, Strasser and Kelly, 2016; Wu and Prives, 2017; Dhar *et al.*, 2018). p53 is translocated into the nucleus and induces $p21^{Waf1}$ expression, as well as Noxa and Puma pro-apoptotic gene expression that leads not only to the arrest of cell cycle in damaged cells but also to its senescence and apoptosis (Aubrey, Strasser and Kelly, 2016; Dhar *et al.*, 2018). p53 also prevents CD44 expression and together with p21 protein avoid cellular reprogramming (Dhar *et al.*, 2018).

However, a carcinogenic insult could cause release of DAMPs that activate liver macrophages to produce cytokines such as Interleukine-6 (IL-6) (Maeda *et al.*, 2005; Bergmann *et al.*, 2017) and growth factors including EGFR ligands like EGF, HB-EGF, epiregulin, betacellulin, and transforming growth factor α and c-Met ligand, HGF (Dhar *et al.*, 2018). Thus, they will activate EGFR/CD44 receptors and Protein Kinase B (Akt), resulting in Mdm2 phosphorylation and in its nuclear translocation by CD44-coupledEGFR-Akt signalling axis. Nuclear Mdm2 inhibits p53 activation and accumulation, allowing the survival, proliferation and transmission of potentially oncogenic mutations from carcinogen-exposed Pericentral Hepatocytes to their progeny. The activation of Janus Kinase 1/2 is caused by CD44, resulting in the phosphorylation of an oncogenic transcription factor, Signal Transducer and Activator of Transcription 3 (STAT3), that will also translocate into the nucleus and induce CD44 expression (Cells, 2008; G. He *et al.*, 2010; Dhar *et al.*, 2018). Most likely, induction of CD44 expression ensures growth factor-induced regeneration of Pericentral Hepatocytes after acute toxic injury. In other words, CD44 couples the necroinflammatory response that leads to STAT3 activation to inhibition of the tumour-suppressive p53 response (Dhar *et al.*, 2018).

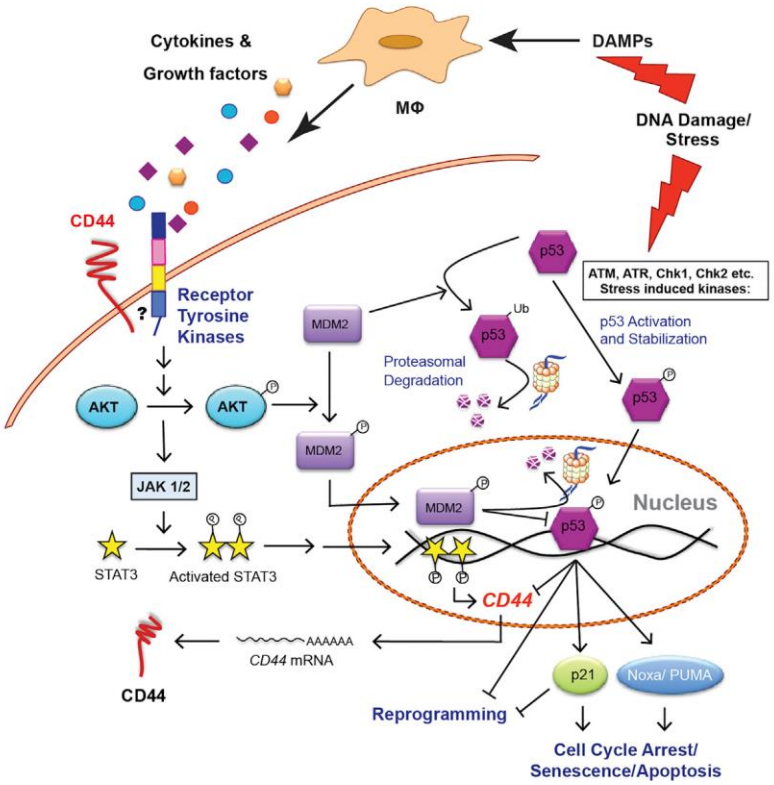

Figure 10 – Schematic representation of the molecular circuit required for HCC initiation in Pericentral Hepatocytes. STAT3 regulates CD44 expression, responsible for the suppression of damage-induced p53 response. The p53 protein is inhibited by Mdm2, whose nuclear translocation is facilitated by CD44-coupledEGFR-Akt signalling axis. Ultimately, CD44 promotes HCC initiation due to its protective effect in hepatocytes submitted to carcinogenic insult (reproduced from Dhar et al., 2018).

13. Protein Therapeutics

New therapeutic approaches for the treatment of several diseases or conditions are gaining a significant impact on medicine and clinical investigation. *Protein Therapeutics* could revolutionize cancer treatment in the near future because it offers greater specificity and a much more complex set of functions than conventional chemotherapy strategies. New production methods of recombinant proteins are changing the scale, the cost and even its administration routes. The first breakthrough in protein therapeutics was the recombinant production of insulin at the beginning of the seventies. However, failed vaccine attempts, non-humanized monoclonal antibodies and cancer trials questioned the credibility of this therapeutic strategy. Recent achievements in the fields of genetics and protein therapeutics thrilled once again the scientific community. Currently, human recombinant proteins or peptides are the major newly approved drugs from biotechnology origin by U.S Food & Drug Administration (FDA),

that include monoclonal antibodies, interferons, hormones, modified enzymes and several types of cellular therapies (Leader, Baca and Golan, 2008; Shi *et al.*, 2019).

Proteins are known for being the macromolecule that has the most dynamic and diverse role in the human organism. They act as catalysts in biochemical reactions and molecule transporters, form receptor and cell membranes and provide intracellular and extracellular scaffolding support (Leader, Baca and Golan, 2008). Due to this diversity of functions, protein therapeutics is functionally classified into four distinct groups, as summarized in Table 2.

Table 2 – Functional classification of protein therapeutics and specifications of each group (Adapted from (Leader, Baca and Golan, 2008).

Group	Functional Classification	Specifications
I	Protein therapeutics with enzymatic or regulatory activity	a: Replacing an abnormal or deficient b: Augmenting an existing pathway c: Providing a novel function or activity
II	Protein therapeutics with special targeting activity	a: Interfering with a molecule or organism b: Delivering other compounds or proteins
III	Protein Vaccines	a: Protecting against a deleterious foreign agent b: Treating an autoimmune disease c: Treating cancer
IV	Protein Diagnostics	-

This new therapeutic strategy is considered a safer alternative to gene therapy because it doesn't require permanent genetic changes of the target cells and it isn't involved in random genetic alterations in the genetic profile of those same cells (Ford *et al.*, 2001). However, there are some challenges to address in this scientific field, such as protein instability, immunogenicity, low circulation times, protein susceptibility to hydrolysis/proteolysis/oxidation/denaturation (Manning *et al.*, 2010) and low cellular internalization due to low membrane permeability (Lu, Sun and Gu, 2014).

14. MSNs as Protein Nanocarriers

Using nanocarriers for transport and delivery of proteins is the most considered solution for addressing the disadvantages of protein therapeutics previously mentioned. Nanocarriers facilitate the intracellular delivery of proteins and protect them from premature degradation and denaturation processes. As previously referred in sections 5 and 6 of this chapter, nanocarriers present low toxicity and its chemical structure can be easily modulated for the potentiation of the intended therapeutic purpose (Shi *et al.*, 2019).

MSNs present great potential as a non-invasive and biocompatible nanocarrier for protein delivery in the fields of enzyme therapies, vaccination and imaging. Their reduced size comparing with eukaryotic cells makes them a facilitating platform for the transport of proteins into cell cytosol via an endocytosis pathway and subsequent endosomal escape. Proteins can be adsorbed either at the outer surface of the MSNs or into its pores usually by the immersion approach (He and Shi, 2014). Typically, proteins adsorbed at the outer surface of MSNs aren't protected by the interior environment of the nanocarrier, thus being exposed to a great diversity of proteases and denaturation conditions that could compromise protein folding. Also, in the outer surface, proteins don't take advantage of the large internal surface area created by the pores that may increase the encapsulation of small and larger molecules. For increasing encapsulation efficiency and release control, larger pore channels are required, whose ideal dimensions should be between 5 and 10 nm (Slowing, Trewyn and Lin, 2007; Tu *et al.*, 2016). Chemical functionalization of MSNs surface with HA may increase cellular uptake and promote the adsorption of proteins with different isoelectric points at the outer surface of the silica nanocarrier (Tu *et al.*, 2016).

Protein encapsulation and release by MSNs depends not only on the surface chemistry of the silica nanocarrier but also from protein size and charge distribution. The effects of protein size and charge distribution in the encapsulation process are easily separated. Nevertheless, more research is required for clearly understanding which effect is more important (Tu *et al.*, 2016). Some authors state that protein adsorption depends of the protein's isoelectric point (pI) and that the optimal protein encapsulation process occurs when the MSNs and the protein have opposite surface charges (Moerz and Huber, 2015; Shi *et al.*, 2019). The relevance of these properties is also significant in the release kinetics. More, release parameters like the ones previously mentioned plus incubation buffer and ionic force make this process characterization more subtle than the encapsulation characterization. Released proteins from MSNs usually present the

original folding, indicating that strong MSNs-Protein interactions aren't expected (Tu *et al.*, 2016).

Generally, MSNs are capable of encapsulating from 200 mg to 300 mg of a therapeutic drug per 1 g of silica but this ratio could be extended up to 600 mg of drug per 1 g of silica (He and Shi, 2014). There are already some data referring to protein encapsulation into MSNs in the literature. The most commonly used proteins in this type of study are listed in Table 3 alongside some of its properties, such as classification, molecular weight (M_w) and pI.

Table 3 – Most common proteins encapsulated into in MSN and its general properties.

Protein	**PDB code**	**Classification**	**M_w (kDa)**	**pI**	**Reference(s)**
Alpha-lactalbumin	1HFX	Glycoprotein	14.2	4.5	(Tu *et al.*, 2016)
Bovine Serum Albumin (BSA)	4F5S	Transport Protein	66.5	4.9	(Katiyar *et al.*, 2010; Landry and Asuncion, 2014; Tu *et al.*, 2016; Clemments, Botella and Landry, 2017)
Catalase	1TGU	Oxidoreductase	250.0	5.8	(Tu *et al.*, 2016)
Haemoglobin	2QSS	Oxygen Binding	64.5	6.8	(Landry and Asuncion, 2014; Tu *et al.*, 2016)
Myoglobin	3RGK	Oxygen Transport	17.9	6.9	(Moerz and Huber, 2015)
Lysozyme	4YM8	Hydrolase	14.3	10.0-10.5	(Katiyar *et al.*, 2010; Moerz and Huber, 2015; Tu *et al.*, 2016)
Cytochrome C	2N3B	Electron Transport	12.4	11.35	(Slowing, Trewyn and Lin, 2007; Moerz and Huber, 2015; Tu *et al.*, 2016; Shi *et al.*, 2019)
Green Fluorescent Protein (GFP)	1B9C	Luminescent Protein	26.7	5.8	(Shi *et al.*, 2019)
KillerRed	3WCK	Fluorescent Protein	24.3	5.1	(Shi *et al.*, 2019)

15. Cytokines and Human Interferon-α2b for HCC treatment

Cytokines are the molecules used for communication among cells of the immune system. The interaction of a cytokine with its membrane receptor on a target cell can cause changes, not only in the expression of adhesion molecules and chemokine receptors on the target membrane but also in its transcriptional program. Thus, effector functions could be altered and ultimately cytokines can promote cell survival or trigger cell death (Kuby *et al.*, 2013). The first classified cytokines were named Interleukins. However, further discovered Interleukins were reclassified and they are most commonly known as Tumour Necrosis Factor (TNF) or Interferon (IFN). A subpopulation of cytokines known as Chemokines participates in the organism immune response and possesses the ability to mobilize immune cells from one organ to another or from one zone of an organ to another (Kuby *et al.*, 2013).

Cytokines and associated receptors are divided among six families, depending on their molecular and cell biology and associated secretory pathways (Kuby *et al.*, 2013). Regarding the molecular interactions responsible for HCC initiation, represented in Figure 7, is observable that the Hematopoietin (Class I Cytokine) Family plays an important role in this type of cancer. Thus, mechanistic knowledge about some of Class I Cytokines involved in HCC, such as IL-6, contributes to the establishment of this cancer initiation mechanism and to the proposal of some therapeutic solutions (Spangenberg, Thimme and Blum, 2008; Tamori *et al.*, 2016; Dutta and Mahato, 2017). Therefore, IFN-α (Class II Cytokine) is one of the most used cytokines in multiple cancers treatment, playing an important role in the application of adjuvant therapies (Kotredes and Gamero, 2013; Dutta and Mahato, 2017). IFN-α is already commercialized as an approved drug (*Roferon® A* and *Intron® A*) not only for the treatment of liver-related pathologies such as Hepatitis B and Hepatitis C but also for cancer treatment, presenting good effectiveness against hairy cell leukemia, melanoma, renal cell carcinoma, follicular non-Hodgkin's lymphoma, chronic myelogenous leukemia and AIDS-related Kaposi's sarcoma (Srivastava *et al.*, 2005; Kuby *et al.*, 2013).

Interferons (IFNs) are a family of naturally secreted glycoproteins produced by almost all types of cells under a biological pathogenic attack or in the presence of a carcinogenic insult. This family of cytokines received its name due to its ability to interfere with a viral infection and is known for its immunomodulatory, antiangiogenic, antiproliferative and apoptotic activities (Kotredes and Gamero, 2013; William J Crisler and Lenz, 2018). Depending on each IFN specific receptor binding, three types of IFNs had been identified. Type I INFs comprise 13 subtypes of IFN-α, IFN-β, IFN-δ IFN-ε, IFN-κ, IFN-ξ, IFN-τ and IFN-ω. Type II IFNs only include IFN-γ. Type III IFNs are represented

by IFN-λ1 (IL-29), IFN-λ2 (IL-28A) and IFN-λ3 (IL-28A). Receptors for type I and type II IFNs are expressed by almost all types of nucleated cells, whereas the expression of type III IFNs receptors is restricted to epithelial cells, hepatocytes and a subset of immune cell types (Kotredes and Gamero, 2013; William J Crisler and Lenz, 2018).

IFN-α2b is one member of IFN-α2 group of proteins with a similar biological activity that is known for its therapeutic use in multiple cancers treatment (Srivastava *et al.*, 2005). A monomeric IFN-α2b is composed by five α-helixes linked by one long overhand connection and three short segments. The length of the helix D is similar to ones found in IFN-β, IFN-γ and IL-10 which bind Class 2 Cytokines Receptors. At physiological conditions and for concentrations up to 50 µM, IFN-α2b is monomeric in its active form (Radhakrishnan *et al.*, 1996). IFN-α2b presents a considerable amino acid sequence homology with the remaining IFNs from IFN-α family and a molecular weight of approximately 18.5 kDa (Radhakrishnan *et al.*, 1996; Srivastava *et al.*, 2005). The receptor for IFN-α2b belongs to the Class II Helical Cytokine Receptor (hCR) family and the involved structures, IFNAR1 and IFNAR2, present different affinities for its ligand (see Figure 11). Comparing their K_d values, IFNAR1 presents lower affinity ($0.05 < K_d <$ 10 µM) than IFNAR2 ($0.1 < K_d <$ 1000 nM). Considering IFNAR-ligand interaction, each one of the described structures plays a different role when binding IFN-α2b. IFNAR1 is necessary for signalling and possibly responsible for the differential recognition of IFNs, while IFNAR2 is directly involved in ligand interactions through its aliphatic hydrophobic amino acids. Regarding the expression patterns, IFNAR1 expression is more extensive than IFNAR2, that is more restricted. (De Weerd, Samarajiwa and Hertzog, 2007). IFNAR2 also exists in three distinct forms: IFNAR2-a (short form), IFNAR2-b (soluble form) and IFNAR2-c (long form), which will be important for the signal transduction mechanism represented in Figure 12 (Pfeffer *et al.*, 1998; De Weerd, Samarajiwa and Hertzog, 2007).

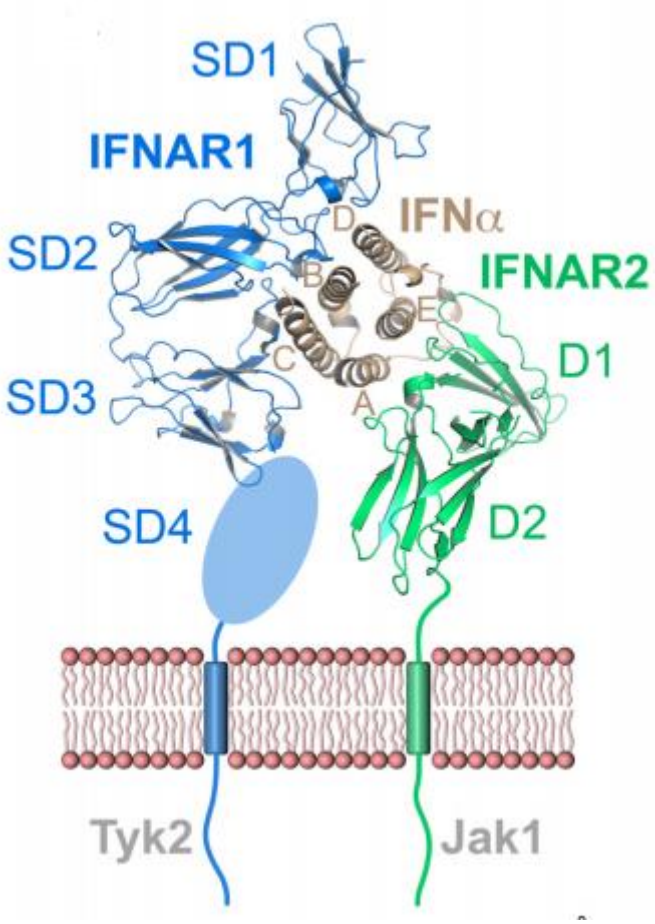

Figure 11 – Crystal structures of type I IFN receptor components and ligand-receptor complexes Ribbon representations of Ternary complex of IFNAR1 (blue), IFNAR2 (green) and IFNα -2b. Reproduced from Thomas, Christoph et al., 2011 (PDB code: 3SE3).

When IFN-α2b binds the heterodimeric IFNAR complex causes an oligomerization of IFNAR1 and IFNAR2 receptor chains (Pfeffer *et al.*, 1998; William J. Crisler and Lenz, 2018). Constitutively associated JAK1 and TYK2 tyrosine kinases to the receptor chains phosphorylate each other and the activated kinases phosphorylate residues on the associated receptor chains. Those residues act as docking stations for cytoplasmic STAT1 and STAT2 proteins which are phosphorylated by receptor-associated JAKs (Pfeffer *et al.*, 1998). The consequence of this phosphorylation cascade is the formation of an active STAT1-STAT2 heterodimer (Au-Yeung, Mandhana and Horvath, 2013) which associates with interferon-regulated factor nine (IRF-9) originating the ISGF3 complex (McComb *et al.*, 2014). The ISGF3 complex is translocated into the nucleus to bind IFN-Stimulated Response Elements (ISRE) and then inducing the transcription of Interferon Stimulated Genes (ISGs) (Pfeffer *et al.*, 1998; William J. Crisler and Lenz, 2018). Ultimately, IFN-α2b causes the activation of ERK1/2 and JNK pathways culminating in apoptosis via the mitochondrial-dependent death pathway and involving the activation of proapoptotic Bcl-2 family members Bax and Bak. Nevertheless, the NF-

κB survival pathway and other unknown additional pathways are involved in the regulation of this IFN-induced apoptotic process (Kotredes and Gamero, 2013).

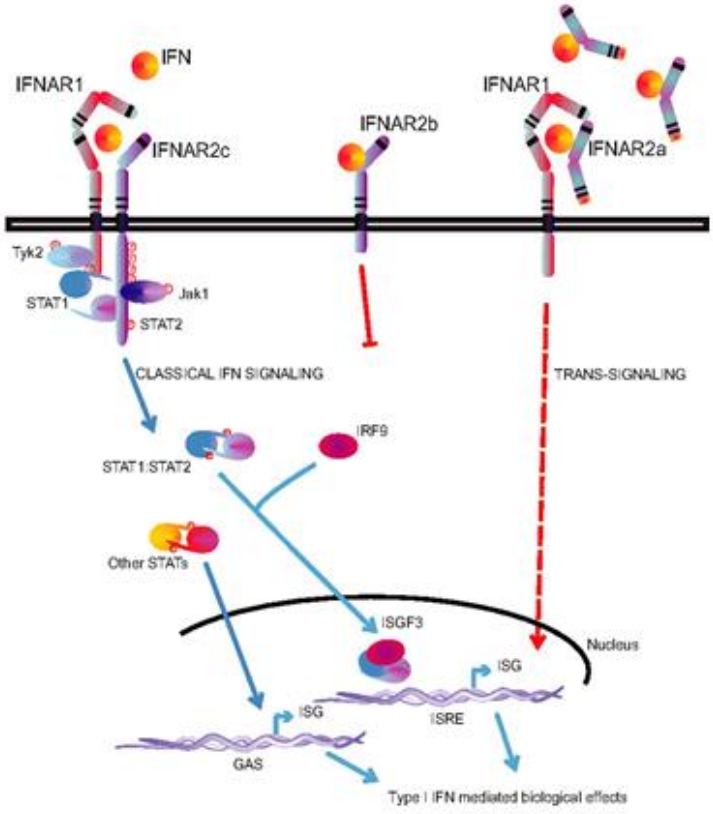

Figure 12 - Schematic representation of the classical IFN signalling pathway triggered by the binding of an IFN to its receptor complex. The IFN binding to IFNAR-2b shows no signalling consequences, while its binding to IFNAR-2c triggers a trans-signalling response that will affect gene expression (reproduced from De Weerd, Samarajiwa and Hertzog, 2007).

Objectives and Motivations

The purpose of this work is to develop and characterize a new drug delivery system that could be used to mediate a new therapeutic strategy against Hepatocellular Carcinoma (HCC). This new drug delivery system is composed of a mesoporous silica nanoparticle functionalized with a naturally occurring and mucoadhesive carbohydrate, hyaluronic acid, and a recombinant human protein, IFN-α2b, known as a cellular apoptosis inducer. The potential of protein transport and delivery of mesoporous silica nanoparticles is already described and characterized in the literature for a great variety of proteins, which are loaded into the silica nanoparticles' pores. So, the intention of adsorbing IFN-α2b at the surface of the nanosystem is to increase the exposition of the protein to promote the interaction with its specific receptor at the surface of the target cells.

To accomplish this goal, three objectives must be achieved:

1. Development, characterization and optimization of the silica nanocarrier;
2. Expression and purification of the recombinant human protein IFN-α2b;
3. Assembly and physicochemical characterization of the new drug delivery system;

The driving forces for the development of this work are related to the harmful consequences caused by conventional chemotherapy in the cancer patients and the low associated therapeutic indexes.

Thus, the notorious emergence in biomedical applications for the scientific fields of nanomaterials and biotechnology provides an excellent opportunity to use multiple experimental techniques in the development of a new drug delivery system that could constitute a new option for a therapeutic strategy in cancer treatment.

Chapter II

Materials and Methods

The experimental design of this work was executed as described in the diagram represented in Supplementary Figure 1. The methodologies applied in each step are described below, throughout this chapter.

1. Development of the silica nanocarrier formulation

1.1 MSNs Synthesis

The synthesis of mesoporous silica tetrasulfide-based nanoparticles was adapted from a procedure described in the literature (Hadipour Moghaddam *et al.*, 2017). Briefly, 110 mL of ultra-pure water, 10 mL of 100% EtOH, 900 µL of an aqueous solution of 2M NaOH and 220 mg of cetrimonium bromide (CTAB) were mixed together in a 500 mL round-bottomed flask in a bath at 80 ºC for 30 minutes under reflux with a stirring rate of 500 rpm, ensuring a complete dissolution of the surfactant used. After increasing the stirring rate to 1,400 rpm, a mixture of TEOS and BTESPT with a molar ratio of 6.6:1 was added dropwise to the solution (i.e. 1.24 mL of TEOS and 0.42 mL of BTESPT) and the synthesis reaction conditions were maintained for 6 hours. Then, the nanoparticles obtained were precipitated and washed three times with 100% EtOH by centrifugation at 18,000 rpm and 4 ºC for 10 min (Avanti J-20 Centrifuge – Beckman Coulter). By the end of this step, the MSNs were suspended in 30 mL of 100% EtOH.

1.2 Pore Induction

For removing the surfactant, the suspension of MSNs was placed on an ice bath and dispersed using sonication (60% vibration amplitude, 2 minutes on, 1 minute off cooling the apparatus with icy water and 2 minutes on). Then, 1 mL of 37% Hydrochloric acid (HCl) was added and the reaction volume was transferred to a 500 mL round-bottomed flask, placed in a bath at 80 ºC under a stirring rate of 1,400 rpm for another 6 hours. Then, the MSNs were washed three times by centrifugation at 18,000 rpm and 4 ºC for 10 min (Avanti J-20 Centrifuge – Beckman Coulter) with ultra-pure water and transferred into Falcon tubes. Carefully, all the tubes containing MSNs were frozen at -

80 ºC and freeze-dried at approximately -50 ºC for 24 hours (CoolSafe Freeze Dryers – ScanVac, Labogene).

1.3 MSNs Surface Modifications

1.3.1 MSNs modification with (3-Glycidyloxypropyl)trimethoxysilane (GPTS)

The modification of the MSNs with GPTS was adapted from a procedure described in the literature (Chu, Daniels and Francis, 1997; Li *et al.*, 2014). Briefly, 100 mg of the MSNs synthesized as described earlier were dissolved in a 10 mL solution containing 5.7 mL of ultra-pure water and 4.3 mL of 100% EtOH in a 50 mL round-bottomed flask under reflux at room temperature and a stirring rate of 400 rpm for 30 minutes. Using an aqueous solution of 25% Ammonia (NH_3), the pH was adjusted to 9.5 and 93.5 µL of GPTS was added to the MSNs. After this step, the MSNs were replaced under reflux, again at a stirring rate of 400 rpm and at room temperature for 24 hours. Then, the reaction solvent was extracted recurring to centrifugation at 4,000 rpm for 30 minutes and the MSNs were washed one time with 100% EtOH at 4,000 rpm for 10 minutes. The supernatant was discarded and the MSNs were left drying at 50 ºC for 24 hours.

1.3.1.1 MSNs functionalization with HA

The functionalization of the MSNs was adapted from a procedure described in the literature (Li *et al.*, 2014; Salis *et al.*, 2016). Initially, a 4 mg/mL HA in 0.1 M NaOH solution was thoroughly prepared. For completely dissolving the HA, 10-minute cycles of manually stirring and ultrasound aid were alternately used. Then, 10 mL of this solution was added to approximately 110 mg of MSNs previously modified with GPTS and left under reflux, in a bath at 35 ºC and at a stirring rate of 400 rpm for 16 hours. Next, the MSNs were precipitated recurring to centrifugation at 16,000 rpm and 4 ºC for 30 minutes and the supernatant was collected (Avanti J-20 XP Centrifuge – Beckman Coulter). Finally, the MSNs were washed two more times with EtOH at 4,000 rpm and 4 ºC for 10 minutes each and dried at 32 ºC for 24 hours.

1.3.1.2 HA Quantification: Phenol-Sulphuric Acid Method

The quantification of HA that functionalized the modified surface of MSNs with GPTS was performed using a method described in the literature (Dubois *et al.*, 1956;

Khamlue, Ounaroon and Saelim, 2012). Briefly, a calibration curve was obtained adding 100 µL of standard HA solutions in 0.1 M NaOH (mimicking the conditions in the functionalization reaction and ranging from 0.2 and 1.0 mg/mL concentrations of HA) to 900 µL of 0.1 M NaOH. Then, 25 µL of a 0.81mg/mL phenol aqueous solution was added to the previous mixture ensuring its homogeneity. Finally, 2.5 mL of 97% Sulphuric acid (H_2SO_4) were added dropwise to the mixture and safely stored for 30 minutes at room temperature. Using quartz cuvettes, their optical density was measured at a wavelength of 480 nm (Spectrophotometer Spectramax plus 384 - Molecular Devices LLC). The same procedure was applied to the prepared HA stock solution and final samples collected by the end of the functionalization reaction.

1.3.1.3 BSA loading into MSNs

BSA adsorption into functionalized MSNs with HA was adapted from a procedure described in the literature (Nairi *et al.*, 2018). Firstly, 20 mg of functionalized MSNs with HA were dissolved in 2 mL of a 4 mg/mL solution of BSA in Phosphate-Buffered Saline (PBS) buffer (pH 7.53; prepared as described by *Cold Spring Harbor Protocols* without the addition of any supplement (doi:10.1101/pdb.rec8247) for 16 hours under agitation at 4ºC. Then, the supernatant was collected through centrifugation at 4000 rpm and 4ºC for 20 minutes (Eppendorf 5810R Centrifuge – Eppendorf) and stored at 4ºC for BSA quantification.

1.3.2 MSNs modification with (3-Aminopropyl)triethoxysilane (APTES)

The modification of MSNs with APTES was adapted from procedures described in the literature (Salis *et al.*, 2016; Wang *et al.*, 2016; Nairi *et al.*, 2018). Briefly, 50 mg of MSNs were dispersed in 25 mL of ultra-pure water in a 50 mL round-bottomed flask using ultrasounds in the same conditions as described in topic 2.1 of this chapter. Then, the flask was placed in a bath at 50 ºC and 500 µL of APTES were added dropwise to the MSNs and left at a stirring rate of 500 rpm for 24 hours. Next, the MSNs were transferred into plastic tubes, precipitated and washed two times with ultra-pure water by centrifugation at 18,000 rpm and 4 ºC for 10 min (Avanti J-20 Centrifuge – Beckman Coulter). Finally, all the tubes containing modified MSNs with APTES (MSN-NH_2) were frozen at -80 ºC and freeze-dried at approximately -50 ºC for 24 hours (CoolSafe Freeze Dryers – ScanVac, Labogene).

1.3.2.1 MSN-NH_2 functionalization with HA

The functionalization of the MSNs was adapted from a procedure described in the literature (Salis *et al.*, 2016; Nairi *et al.*, 2018). In one round-bottomed flask, 25 mg of MSN-NH_2 were dispersed in 25 mL of ultra-pure water using ultrasounds in the same conditions as described in topic 2.1 of this chapter. In a separate beaker, 28.25 mg of HA were thoroughly dissolved in 15 mL of ultra-pure water with the aid of magnetic agitation at a stirring rate of 400 rpm for approximately 1 hour. In another beaker, 92.5 mg of N-Hydroxysulfosuccinimide (NHS > 97%) and 50 mg of N-(3-Dimethylaminopropyl)-N′-ethylcarbodiimide hydrochloride (EDC > 98%) were dissolved in ultra-pure water and homogenized. Then, the EDC/NHS mixture was added to the HA solution and the mixture containing EDC, NHS and HA was poured into the MSNs dispersion in the round-bottomed flask. The pH of the final mixture containing MSNs, EDC, NHS and HA was adjusted to 9.0 with the addition of approximately 100 µL of Triethylamine (TEA) and left overnight in a bath at 38 ºC under a stirring rate of 500 rpm. Next, the MSNs were transferred into plastic tubes, precipitated and washed two times with ultra-pure water by centrifugation at 18,000 rpm and 4 ºC for 10 min (Avanti J-20 Centrifuge – Beckman Coulter). Finally, all the tubes containing functionalized MSNs with HA (MSN-HA) were frozen at -80 ºC and freeze-dried at approximately -50 ºC for 24 hours (CoolSafe Freeze Dryers – ScanVac, Labogene) and then stored at 4 ºC.

1.3.2.2 Recombinant human IFNα-2b loading into MSN-HA

IFNα-2b adsorption into MSN-HA was adapted from solution immersion procedures described in the literature (He and Shi, 2014; Shi *et al.*, 2019). Initially, 7 mg of unmodified MSNs (MSN-OH), MSN-NH_2 and MSN-HA were dispersed in 1 mL of ultra-pure water using ultrasounds in the same conditions as described in topic 2.1 of this chapter. Next, 3.18 mg of recombinant human IFNα-2b were dissolved in 1 mL of ultra-pure water and gently homogenized. Then, 20 µL of the recombinant protein stock were individually added to a 200 µL aliquot of MSNs dispersions in a 2 mL Eppendorf tube. Two aliquots were removed from each stock dispersion of MSNs (MSN-OH, MSN-NH_2 and MSN-HA) and two conditions were tested on each one of them. One aliquot was gently shaken for approximately 10 seconds at room temperature and then centrifugated twice at 14,000 rpm for 5 minutes at each time (Eppendorf 5810R Centrifuge – Eppendorf). The precipitated MSNs were frozen at -20 ºC and the supernatant collected and stored at 4ºC. The other one remained overnight under gentle rotation and in the following morning, its supernatant was equally collected. The supernatants of both aliquots from all types of MSNs were used to access the weight of adsorbed protein.

A scale-up of this experiment was also performed. The general procedure was equally applied as described before, but different ratios of MSNs and recombinant protein were used. Now, 10 mg of MSN-OH, MSN-NH_2 and MSN-HA were dispersed in 2 mL of ultra-pure water and 10 mg of recombinant human IFNα-2b were dissolved in 2 mL of ultra-pure water. For each aliquot, 40 μL of recombinant protein stock were individually added to 400 μL of MSNs dispersions. All supernatants were collected and stored at 4 ºC and precipitated MSNs were frozen at 4ºC.

2. Recombinant IFNα-2b production

2.1Expression vector containing recombinant human IFNα-2b

A high copy (HC) pSMART® plasmid containing IFNα-2b synthetic coding sequence (NCBI Protein Accession Number: P01563) was the expression vector used in this work. It was synthesized, developed and optimized by a biotechnology company called *GeneCust* for allowing the expression of a soluble and active eukaryotic protein in a prokaryotic system. Thus, the synthetic sequence was developed in order to obtain a protein whose affinity towards its receptors is modulated as described by Zhang and his colleagues in a recent publication in which they prove the enhancement of the IFNα-2b anticancer properties (Zhang *et al.*, 2017). The respective nucleotide sequence was inserted in the plasmid in the restriction site cleaved by BamHI and XhoI endonucleases.

pSMART® HCKan plasmid, represented in Figure 13, is composed of 1,788 nucleotide base pairs and presents several advantages comparing to standard plasmids used for similar purposes. The presence of transcription terminators (T) eliminates transcription both into and out of the insert DNA, avoiding the transcription of toxic coding sequences and deleterious features, such as sequences with strong secondary structure. The general design of this plasmid increases its stability in *E. coli* cells and its copy numbers per cell are approximately 300, similar to ones known for pUC plasmids. The selection mark confers *E. coli* colonies resistance to Kanamycin (Kan) and the advantage in using kanamycin-resistant pSMART® vectors is the complete elimination of satellite colonies and the high copy option theoretically increases the amount of transcript genetic material that ultimately will reflect the amount of protein produced. Finally, pSMART® HCKan transformants don't require additional screening against colonies containing empty vector because they shouldn't be present at detectable levels (Lucigen Corporation, no date).

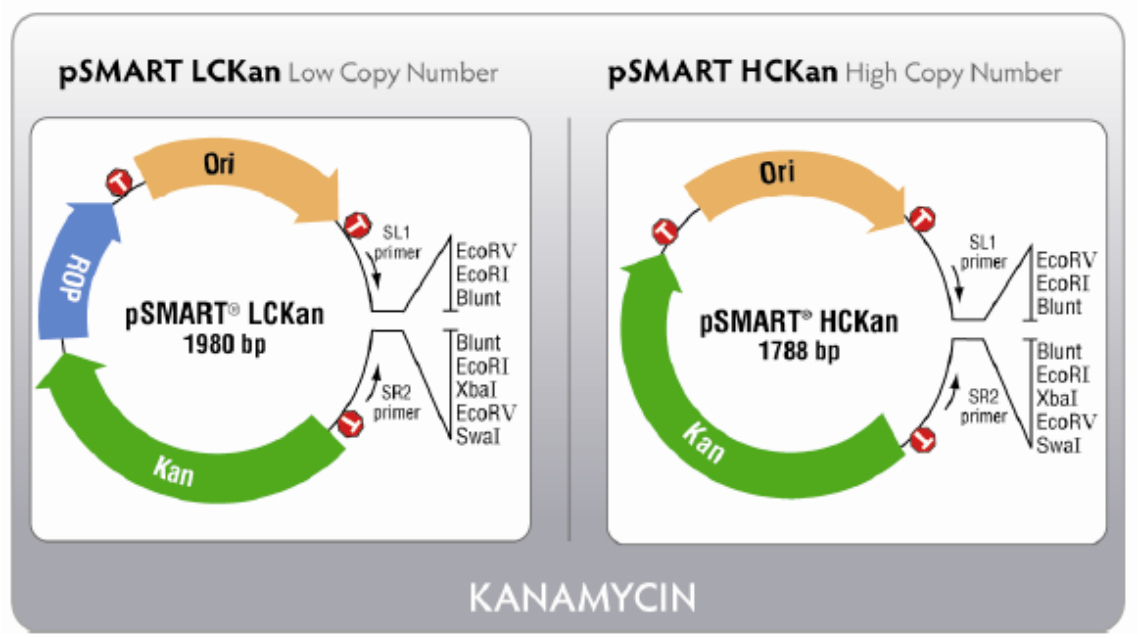

Figure 13 -Schematic diagram of the kanamycin-resistant pSMART® vectors. Ori: origin of replication; Kan: Kanamycin resistance gene; ROP: Repressor of primer (lowers plasmid copy number). Approximate positions of sequencing primers and transcription terminators (T) are indicated (reproduced from Lucigen Corporation, no date).

2.2 Preparation of LB medium and LB medium with agar

According to the instructions provided by the manufacturer, 500 mL of Luria Broth (LB) Medium were prepared. Briefly, 12.5 g of LB powder was dissolved in 500 mL of ultra-pure water and equally distributed into 2 Glass Media Bottles (Schott) of 500 mL. In one of them, 3.75 g of agar were dissolved in the LB medium. Both flasks were subjected to autoclave sterilization and after a cooldown period, Kanamycin (stock solution 30 mg/mL) was added in the ratio of 1:1000 to both flasks under sterile conditions. The content of both flasks was gently shaken and approximately 10 mL of LB medium containing agar was added to sterile Petri dishes. After medium solidification, all Petri dishes were stored at 4 ºC with the lids facing downwards.

2.3 Transformation of *E. coli* competent cells

Transformation and cloning procedures described were adapted from the literature (Cohen, Stanley N., Chang, Annie C., Hsu, 1972; Sambrock, J., Fritschf and MANIATIS, 1989).

The following protocol was used for the transformation of competent strains of *E. coli* previously stored in a glycerol stock solution. The original dried stock of plasmid sent

by the manufacturer was resuspended in 20 µL of sterile, ultra-pure water, presenting a concentration of f 171.3 µg/µL. Plasmid's concentration was accessed using a NanoDrop™ 2000 Spectrophotometer (Thermo-Fisher). Then, 171,3 µg of plasmid were added to another aliquot of competent cells and incubated on ice for 25 minutes. Next, for the heat shock, cells were transferred for 50 seconds into a bath at 42 ºC and smoothly placed again on ice for 3 minutes. 1 mL of sterile LB medium prewarmed to 37 ºC was added to each tube and cells were left to recover from the heat shock at 37 ºC for 1 hour under a stirring rate of 200 rpm. The cells were centrifuged for 1 minute at room temperature and 13,000 rpm (Sigma 1-15) and resuspended in approximately 200 µL of LB medium. Finally, 100 µL of the concentrated cell suspension were spread in LB – Kanamycin plates previously prewarmed to 37 ºC and incubated in an inverted position overnight. In the next day, the plates were checked for colony growth, sealed with parafilm and stored at 4 ºC.

2.4 Preparation of Glycerol Cell Stocks

The freshly grown plates were prewarmed at 37 ºC for 10 minutes in order to pick isolated colonies of BL21® Star *E. coli* strain. Meanwhile, sterile tubes were marked accordingly and 30 µg/mL kanamycin were added to 25 mL of LB medium. Then, LB medium containing kanamycin was distributed into sterile tubes and isolated colonies were selected from the plate and placed to grow in each tube. These cultures were grown overnight slightly sloped at 37 ºC with a stirring rate of 200 rpm. In the following day, the glycerol stocks were prepared for each culture by adding 250 µL of sterile 87% glycerol and 250 µL of cell culture suspension to each tube. All tubes were immediately stored at -80 ºC.

2.5 IFNα-2b expression

For the pre-induce preparation, 100 µL of glycerol cell stock in BL21 Star® containing the plasmid was added to 5 mL of LB medium containing kanamycin. The culture was grown overnight at 37 ºC under a stirring rate of 200 rpm. Then, this cell growth was diluted in a ratio of 1:100 into 500 mL LB medium plus 30 µg/mL kanamycin. The culture was set to grow at 37 ºC with a stirring rate of 200 rpm and its Optical Density (O.D.) at 600 nm was periodically controlled for approximately 3 hours. When the O.D. value of the cell culture was between 0.6-0.8 arbitrary units (a.u.), IFN-α2b expression was induced with the addition of 0.2 mM IPTG. Finally, the culture was grown overnight at approximately 20 ºC with a stirring rate of 200 rpm (Novagen, 2003).

3. Recombinant IFNα-2b purification

3.1 Cell lysis

E. coli cells were sedimented through centrifugation at 6,000 rpm and 4 ºC for 10 minutes (Avanti J-20 Centrifuge – Beckman Coulter) and then resuspended in 40 mL of PBS. The suspension was poured into a Falcon tube and horizontally frozen overnight at -20 ºC. Next, the culture was left to unfreeze, on ice, for 1 hour and then subjected to sonication on an ice bath, based on the conditions described by plasmid's manufacturer company in their quality control report: 25% vibration amplitude, 2 seconds on, 8 seconds off and 25 minutes (distributed in 15 and 5 minute sonication cycles). Finally, insoluble cellular content and inclusion bodies were sedimented by centrifugation at 16,000 rpm and 4 ºC for 10 minutes and the supernatant containing soluble proteins was stored at 4 ºC for further purification.

3.2 Recombinant human IFNα-2b affinity purification

The IFNα-2b was purified by IMAC affinity chromatography performed at medium pressure in an *ÄKTA start protein purification system*, using a 5 mL *HisTrap HP histidine-tagged protein purification column* (GE Healthcare), that takes advantage of the known affinity between the histidine tag and the nickel ions in the column. Firstly, the supernatant containing the soluble protein content released from the *E. coli* cultures was filtered through a sterile, endotoxin-free, hydrophilic, cellulose acetate membrane with 30 mm of diameter and 0.20 μm of porosity (Orange Scientific). Then, 5 column volumes (cv) of PBS supplemented with 20 mM Imidazole were perfused through the column and then approximately 35 mL of supernatant were loaded. PBS supplemented with 20 mM Imidazole was once again perfused through the column and followed by 4 cv of PBS supplemented with 100 mM Imidazole when absorbance readings (λ = 280 nm) stabilize and achieve baseline levels. Finally, 4 cv of PBS supplemented with 500 mM Imidazole were also perfused through the column after the stabilization of baseline absorbance readings. Fractions of representative absorbance peaks were collected and stored in Falcon tubes at 4ºC.

3.3 Dodecyl Sulfate Polyacrylamide Gel Electrophoresis (SDS-PAGE)

12.5% SDS-PAGE was performed as described in the literature (Keller, Pedemonte and Willmouth, 1970) for analysing the protein profiles of the content collected in each relevant fraction from the protein purification process. Denaturation buffer (125 mM Tris-HCL, pH 6.8, 100 mM glycine; 40% (v/v) glycerol; 4% SDS (w/v); 200 mM DDT; 0.001% (w/v) bromophenol blue) and aliquots of the relevant protein fractions were mixed together in an Eppendorf tube considering a ratio of 1:1 and incubated at a Thermoblock (Stuart Scientific) at 100 ºC for 5 minutes. Then, the denaturated samples and a protein ladder (Precision Plus Protein™ All Blue Protein Standards – Bio Rad) were loaded into a 12.5% polyacrylamide gel in a 14-15% glycine, 3% Tris and 1% SDS buffer and subjected to a voltage of 90 V for approximately 45 minutes. After this time, the voltage was increased to 130 V for approximately 1 hour at room temperature. Gels were stained with Coomassie Blue Staining Solution (0.1% (w/v) Brilliant Blue R-250, 45% (v/v) methanol and 5% (v/v) glacial acetic acid) for 15 minutes and then destained overnight with Coomassie Blue Destaining Solution (25% (v/v) methanol and 10% (v/v) glacial acetic acid)

3.4 Protein Dialysis

Pure and impure fractions containing recombinant human IFNα-2b were subjected to dialysis for the removal of PBS and Imidazole salts. Based on the protein profiles of each fraction, the content in each tube was transferred into size 1 dialysis membranes with 24 Å of pore size (Medicell International Ltd.). Then, the membranes were immersed in ultra-pure water with magnetic agitation under a stirring rate of 100 rpm for 1 hour at room temperature. Next to this step, magnetic agitation was turned off and recipients containing the membranes were stored at 4ºC overnight. In the following morning, the recipients were removed from the fridge and placed under magnetic agitation once again for 15 minutes at room temperature. Finally, the content in each membrane was frozen at -80 ºC for the freeze-drying process.

4. Nanosystem Physicochemical Characterization

4.1 Protein Quantification

Protein concentrations were determined using *The Bio-Rad Protein Assay,* following the *Microassay Procedure For Microtiter Plates* presented by the kit's manufacturer (Bio-Rad), that is based in the Bradford Method, described in the literature (Bradford, 1976). Generally, a calibration curve was obtained by mixing together 160 µL of BSA standard protein solutions in PBS or ultra-pure water (ranging from 10 and 80 µg/mL concentrations of protein) and 40 µL of dye reagent concentrate to each well. Then, all samples were incubated for five minutes at room temperature. The microtiter 96-well plate was inserted in a spectrofotometer and absorbance was measured at a wavelength of 595 nm (Spectrofotometer Spectramax Plus 384 - Molecular Devices LLC). The same procedure was applied to the prepared protein stock solutions of BSA or IFNα-2b and the supernatants collected by the end of the protein loading experiment.

4.2 Protein Loading Efficiency & Nanosystem Loading Capacity

For determining Protein Loading Efficiency in weight percentage (LE wt%) into the MSNs it is necessary to calculate the weight of loaded protein. Thus, this value is obtained by measuring the difference in concentration of the protein in the supernatant before and after loading experiments, recurring to the method described in topic 5.1 of this chapter. By weighting a specific mass of any type of MSNs, nanosystem Loading Capacity (LC) can be also accessed. Both parameters are respectively described by equations 1 and 2, presented below:

$$LE\ (wt\%) = \left(\frac{weight\ of\ loaded\ protein}{weight\ of\ feeding\ protein}\right) \times 100 \quad (1)$$

$$LC\ (wt\%) = \left(\frac{weight\ of\ loaded\ protein}{weight\ of\ nanoparticles}\right) \times 100 \quad (2)$$

4.3 DLS and LDV readings

For determining MSNs diameter and ζ-potential, aqueous solutions of unmodified MSNs (MSN-OH), MSN-NH_2 and MSN-HA with a final concentration of 100 µg/mL were prepared. Approximately 0,1 mg of dry MSNs were weighted and dissolved in one millilitre of ultra-pure water (pH = 7.0)) and subjected to ultrasounds in the same

conditions as described in topic 2.1 of this chapter. Then, the solution was transferred to a specific cell and placed in a Zetasizer Nano ZS (Malvern Instruments Ltd., UK).

Specifically, for determining unmodified MSNs (MSN-OH), MSN-NH_2 and MSN-HA hydrodynamic diameter and its respective Polydispersity Index (PdI), measurements were taken by Dynamic Light Scattering (DLS) at 25 ºC and with a detection angle of 173º (backscatter detection).

The zeta potential describes the electrokinetic potential between the dispersion medium and the stationary layer of fluid attached to the dispersed particle (IUPAC, 1997). Thus, ζ-potential measurements were made using Laser Doppler Velocimetry (LDV), being applied the Smoluchowski Model.

Before DLS and LDV readings, mesoporous silica nanoparticles were sonicated in different conditions. The ones used throughout topic 1.3.1 of this work's chapter were sonicated with 60% amplitude for 10 uninterrupted minutes.The remaining topics regarding the utilization of mesoporous silica nanoparticles were sonicated with 60% vibration amplitude, 2 minutes on, 1 minute off cooling the apparatus with icy water and 2 minutes on.

4.4 Fourier Transform Infrared Spectroscopy (FTIR)

For the characterization of mesoporous silica nanoparticles' chemical structure after their synthesis, modification and functionalization reactions, Fourier Transform Infrared Spectroscopy (FTIR) was used. Measurements were performed using the KBr pellet method, which forms a transparent sheet in the IR region due to its plasticity properties when subjected to pressure. Briefly, 0.2-0.3 mg of unmodified (MSN-OH), modified (MSN-NH_2) and functionalized (MSN-HA) mesoporous silica nanoparticles were mixed and grounded in a mortar 78.5-80 mg of KBr until a homogenous mixture was obtained. Then, the samples were dried at 40 ºC for at least 24 hours and rapidly pressed in a pellet-forming die. Before samples' measurements, a background reading was done using a pellet composed only by KBr. All measurements were performed using a FT/IR 4200 spectrometer (Jasco), with 256 scans, a resolution of 4 cm^{-1} and a wavelength range between 400 and 4,000 cm^{-1}.

5. Bioinformatics and Data Statistical Analysis

5.1 Bioinformatics Analysis

Bioinformatics analysis of IFNα-2b nucleotide and amino acid sequences were performed using an online, open source tool called Basic Local Alignment Search Tool (BLAST) that finds regions of similarity between biological sequences. The program compares nucleotide or protein sequences to sequence databases and calculates the statistical significance. (Stephen F. Altschul *et al.*, 1997; Cabello *et al.*, 2010). For this work, the following algorithm parameters were applied:

General Parameters:

- Max target sequences: 100
- Expected threshold: 10
- Word sixe: 6
- Max matches in a query range: 0

Scoring Parameters:

- Matrix: BLOSSUM62
- Gap Costs: Existence: 11 Extension: 1
- Compositional adjustments: Conditional compositional score matrix adjustment

Filters and Masking:

- Filter: Low complexity regions

Another online, open source tool called Constraint-based Multiple Alignment Tool (COBALT) was used as a multiple sequence alignment tool that finds a collection of pairwise constraints derived from conserved domain database, protein motif database, and sequence similarity, using RPS-BLAST, BLASTP, and PHI-BLAST. Pairwise constraints are then incorporated into a progressive multiple alignment (Papadopoulos and Agarwala, 2007).

The following links redirect to BLAST and COBALT web sites, respectively:

- https://blast.ncbi.nlm.nih.gov/Blast.cgi
- https://www.ncbi.nlm.nih.gov/tools/cobalt/cobalt.cgi

5.2 Statistical Analysis

All data was compiled in Microsoft® Office 365 Excel and then analysed using GraphPad Prism 6.01 software (GraphPad Software, Inc., San Diego, California, USA). Results are expressed as mean ± SEM for the number of experiments indicated in figure legends, as well as the statistical tests used for each data analysis. Values with $p < 0.05$ were considered statistically significant. Model equations are available at GraphPad website - https://www.graphpad.com.

Chapter III

Results and Discussion

1. Mesoporous silica nanoparticle synthesis and pore induction

The mesoporous silica nanoparticles synthesis reaction was based on the modified Stöber Process. It requires ultra-pure water as a solvent, EtOH as co-solvent and NaOH as a basic catalyst. CTAB will act as surfactant and a mold because micelles are formed when this compound is dissolved in polar solvents. Silica precursors, TEOS and BTESPT, must be thoroughly homogenized and then added dropwise under intense magnetic stirring to prevent the formation of lumps and ensuring homogenous dispersion of all compounds. Hydrolysis and Condensation of silica sources occurs and the characteristic structural network containing Si-O-Si bridges and tetra-sulphide bonds is formed around the surfactant. The induction of medium-size pores in silica nanoparticles is achieved with their dispersion in acidic EtOH.

The surface chemistry of mesoporous silica nanoparticles is well described in the literature (Zhuravlev, 2000). The previously mentioned hydrolysis and condensation reactions could lead to the formation of different types of silanol groups (such as vicinal, isolated and geminal silanols) and siloxane bridges in the surface of amorphous silica. Thus, negatively charged OH groups theoretically confer a negative surface charge to the mesoporous silica nanoparticle. To verify nanoparticles surface charge and determining their hydrodynamic diameter, zeta potential and DLS readings were performed, respectively. The obtained results show that MSN-OH nanoparticles present an average diameter of 403.4 ± 28.97 nm and an average surface charge of -32.06 ± 1.467 mV (n = 4). These results confirm the assumptions established earlier about nanoparticles' surface charge and indicate that surfactant's micelles were successfully removed from the silica nanoparticles. If not, a positively charged amine located in the outer side of the CTAB micelle would be detected in the LDV measurements. However, hydrodynamic diameter measurements reveal that nanoparticles' size is bigger than expected. According to the authors of the followed protocol (Hadipour Moghaddam *et al.*, 2017), the nanoparticles should have a diameter of 110 nm. Thus, the measurements performed could indicate the formation of mesoporous silica nanoparticles' aggregates, favoured by the multiple centrifugations that they were subjected in washing processes at the end of synthesis reaction and pore induction.

2. Mesoporous silica nanoparticles modification with GPTS, functionalization with HA and protein loading

Freeze-dried mesoporous silica nanoparticles were dispersed for modification with a silica co-percursor, GPTS, whose structure is represented in Figure 14. The experimental purpose was to take advantage of the epoxy's ring opening for the covalent bonding between co-precursor's carboxyl group and the polysaccharide (HA) hydroxide group at the pentose ring.

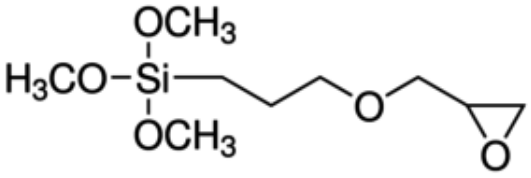

Figure 14- Structural representation of GPTS. Reproduced from (Merck, 2019a).

The hydrodynamic diameter and surface charge of the assembled nanosystem were measured using DLS and LDV. The results were summarized in Table 4 and represented in Figure 15. They show that the average size of the MSN-HA increases approximatelly 100 nm after the modification and functionalization reactions and the ζ-potential remains unaltered. The negative surface charge in both types of mesoporous silica nanoparticles is due to the hydroxide groups present at its surface. The increased diameter in MSiNP-HA could indicate the coating profile intended for the MSNs.

Table 4 – Average hydrodynamic diameter and ζ-potential results obtained after DLS e LDV readings. Data are expressed as mean ± SD of 2 replicates of each type of mesoporous silica nanoparticle

MSNs Types	Diameter (nm)	Z-Potential (mV)
MSN-OH	317.5 ± 16.18	-33.62 ± 1.443
MSN-HA	413.8 ± 22.89	-36.97 ± 0.9443

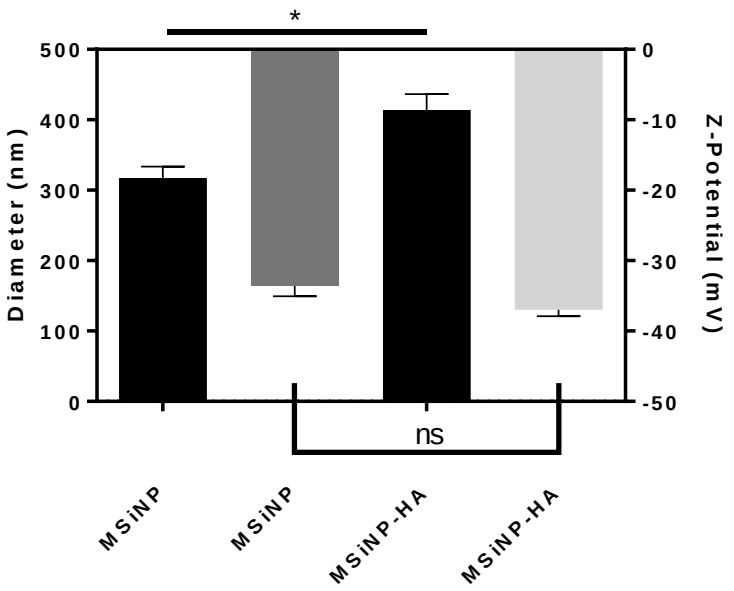

*Figure 15 – Average hydrodynamic diameter and ζ-potential of unfunctionalized (MSiNP) and functionalized nanoparticles (MSiNP-HA). Data are expressed as mean ± SEM of 2 replicates. *: p<0.05, ns: p≥0.05, with p being calculated using two-tailed Mann-Whitney test (n = 2).*

To quantify the mass of HA bonded to the modified silica nanoparticle, the spectrophotometric Phenol-Sulphuric Acid Method was used. The results obtained, represented in Table 5, reflect an excess of HA mass in the supernatant after the functionalization reaction. This result wasn't expected because there wasn't any supplementation with this polysaccharide during the functionalization reaction. Only in one sample, containing mesoporous silica nanoparticles that underwent through both modification and functionalization reactions, HA mass in the supernatant was lower than the one quantified in the HA stock solution.

Table 5 - HA quantification after the functionalization reaction applying Phenol-Sulphuric Acid Method to the supernatant

	HA Stock 1	**Sample 1**	**HA Stock 2**	**Sample 2**	**HA Stock 3**	**Sample 3**
HA mass (mg)	35,7	38	40,7	44,9	43,1	41,2
Functionalized HA mass (mg)	-2.3		-4.2		1.9	

Loading Efficiency (LE) and Loading Capacity (LC) were determined using equations 1 and 2 and the results shown in Figure 16 that no statistically significant differences between both types of mesoporous silica nanoparticles were found.

Nevertheless, the results prove that the system can adsorb protein and suggest that it may be greater in unfunctionalized MSNs (presenting a loading efficiency mean value of 21.29%) than in the functionalized ones (presenting a loading efficiency mean value of 10.86%). Considering the methodology used for these studies, some questions related with the efficiency of the adsorption reaction rose up. After the addition of the solvent containing the protein, even with constant agitation, a considerable mass of nanoparticles deposited in the bottom of the Falcon Tube. Also, the mechanical dispersion promoted by the agitation wasn't enough to completely disperse the nanoparticles. Thus, protein loading efficiency may be compromised because most nanoparticles couldn't interact with BSA.

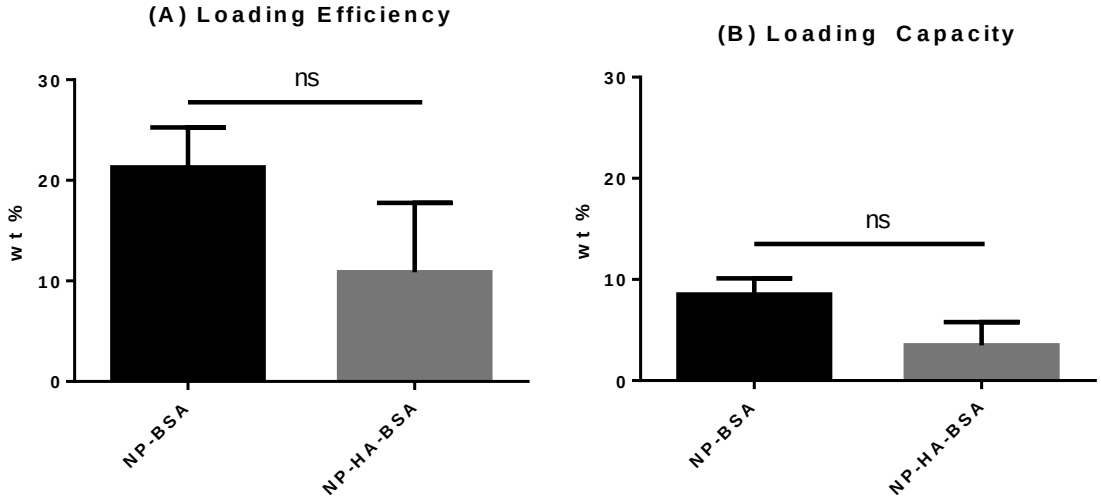

Figure 16 - BSA loading efficiency (A) and loading capacity (B) of unfunctionalized (MSiNP) and functionalized MSNs with HA (MSiNP-HA). Data are expressed as mean ± SEM of 2 replicates. ns: p≥0.05, with p being calculated using two-tailed Mann-Whitney test.

Considering all the obtained results, some questions concerning HA functionalization reaction must be pointed. Despite a diameter increase verified in DLS results, no significant HA mass was detected in the samples collected after the functionalization reaction. As stated before, two positions may be inferred: the yield of the functionalization reaction is practically null, or the method of quantification isn't sufficiently sensitive to the actual functionalization reaction yield. The method is suitable for the quantification of successively diluted HA solutions in 0.1 M NaOH because it allows the obtention of a calibration curve with a coefficient of determination (R^2) of 0.9942. So, is safe to assume that the method isn't sensitive enough to the actual HA functionalization reaction yield. Not dispersing the nanoparticles before reactions and using water as solvent for bonding HA might be the cause of the reaction's unsuccess. Also, Phenol-Sulphuric Acid Method looked like a good experimental solution for a

quantitative characterization of the functionalization reaction. However, method's protocol is a bit complex and some optimizations should be considered.

3. Mesoporous silica nanoparticles modification with APTES, functionalization with HA and nanosystem's physicochemical characterization

Considering the issues pointed out in topic 2 of this chapter, another modification reaction was tested with APTES. Mesoporous silica nanoparticles (MSN-OH) modification with APTES is well described in the literature (Salis *et al.*, 2016; Wang *et al.*, 2016; Nairi *et al.*, 2018).and is largely used for the insertion of NH_2 groups at the nanoparticles' surface. This primary amine presents positive charge and the success of this modification reaction can be easily verified considering nanoparticles' surface charge. Modified mesoporous silica nanoparticles with APTES (MSN-NH_2) were then subjected to the functionalization reaction with HA and a covalent bond between the amine group and the HA's carboxyl group is expected to occur, originating a carboxamide as schematized in Figure 17. At the end of the functionalization reaction (MSN-HA), a negative superficial charge should be recovered due to the hydroxyl groups as part of HA's structure.

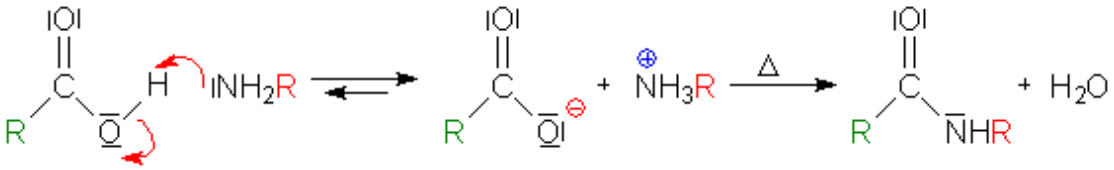

Figure 17 - Formation of a carboxamide by treating with an amine and subsequent heating of the ammonium salt. R letter in the carboxyl represents the remaining structure of HA and the other R in the amine group represents the remaining structure of APTES. Reproduced from (Chemgaroo, no date).

By this step, average hydrodynamic diameter and ζ-potential measurements were made to characterize the modified and functionalized nanosystem. Data were summarized in Supplementary Table 1 and represented in Figure 18 (n = 4). Mesoporous silica nanoparticles' hydrodynamic diameter increases approximately 135 nm after the modification reaction and approximately 292 nm at the end of the functionalization reaction. Comparing the average hydrodynamic diameter of unmodified and functionalized nanoparticles, its value more than duplicate. Thus, looking to this data, more evidence regarding aggregation issues during the development of this silica nanosystem's formulation stands out and particles this big could become an obstacle for

future biodistribution experiments. Mucoadhesive and hygroscopic properties associated to HA (Kim *et al.*, 2019) could help to explain the hydrodynamic diameter value obtained for functionalized nanoparticles since DLS technique measurements could be affected by an excess of water molecules interacting with the polysaccharide.

Regardless of the aggregation issues and the hypothetical influence of HA in the measurements of mesoporous silica nanoparticle's hydrodynamic diameter, there is an experimental cause that could also be contributing to the increased size of the nanoparticles. After their synthesis reaction, silica nanoparticles were necessarily dispersed through sonication. During the time spent performing practical work, the quality condition of the apparatus was affected by its intensive use and the sonication's conditions were altered in order to avoid nanoparticles' contamination with metal released from the apparatus. Shorter and repeated cycles of sonication were applied over time (60% vibration amplitude, 2 minutes on, 1 minute off cooling the apparatus with icy water and 2 minutes on), instead of the 10 minutes of sonication recommended in the followed protocol (Hadipour Moghaddam *et al.*, 2017). Also, was discovered that sonication's amplitude intensity was decreasing over time. Comparing average hydrodynamic diameters measurements of unmodified mesoporous silica nanoparticles (MSN-OH) from topics 2 and 3 of this chapter, there is a difference of 85.9 nm between both hydrodynamic diameter characterizations. Thus, these technical details could be a great influence on the hydrodynamic diameter characterizations.

Considering the surface charge measurements between all types of nanoparticles, clear differences were found regarding their ζ-potential measurements. As expected, average ζ-potential measurements shift from negative to positive values when mesoporous silica nanoparticles are modified with APTES and then shift once again to negative values when modified nanoparticles are functionalized with HA. These results indicate that all previously mentioned reactions are being performed successfully.

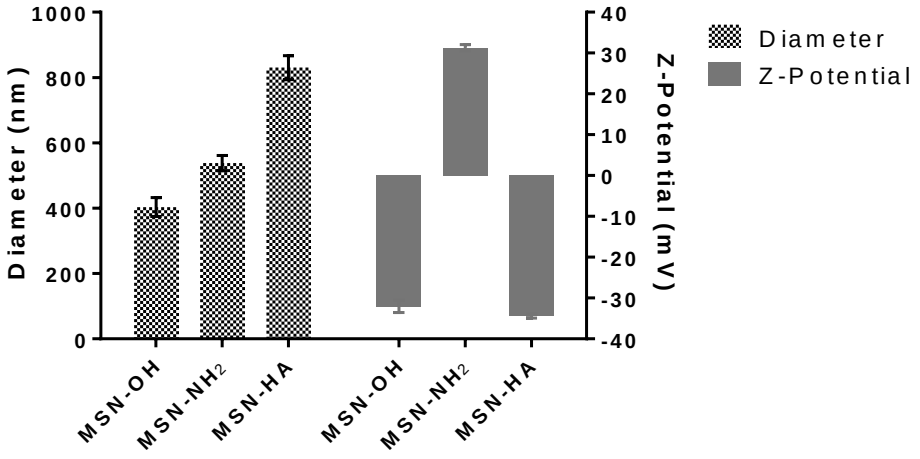

Figure 18 – Physicochemical characterization of unmodified (MSN-OH), modified (MSN-NH_2) and functionalized (MSN-HA) mesoporous silica nanoparticles using DLS and DLV techniques. Data are expressed as mean ± SEM of 4 independent experiments.

Complementary to DLS and LDV nanosystem characterization, Fourier Transform Infrared (FTIR) Spectroscopy was used to prove the structural alterations in the mesoporous silica nanoparticle structure throughout modification and functionalization reactions. In simple terms, IR Spectroscopy principle states that the gross selection rule for a vibrational mode of a molecule to be IR active is that there is a change of the electric dipole moment of molecule upon absorption of light. The absorption of infrared light, due to the excitation from the ground vibrational energy level to a higher energy level, gives information on molecular structure and molecular interactions (Mudunkotuwa, Minshid and Grassian, 2014).

FTIR spectrums of unmodified (MSN-OH), modified (MSN-NH_2) and functionalized (MSN-HA) mesoporous silica nanoparticles can be observed in Figure 19 and respective transmittance peaks were assigned recurring to a IR Spectrum Table and information in the literature (Ma *et al.*, 2012b; Zhang *et al.*, 2014b; Qin *et al.*, 2016; Naowanon *et al.*, 2018; Merck, 2019b). There, the characteristic peaks of silica structure can be observed in all types of mesoporous silica nanoparticle at 465 cm^{-1} (Si-O bending), 800 cm^{-1} (Si-O-Si bending), 950 cm^{-1} (Si-OH bending) and 1100 cm^{-1} (Si-O-Si stretching). Also, at 650 cm^{-1}, transmittance peak corresponding to C-S stretching can be identified. At 1410 cm^{-1}, a sharp peak characteristic of the HA's C=O stretching, appears only in functionalized nanoparticles and in HA control spectrum, proving the success of the followed protocol. At 1555 cm^{-1}, N-H bending peak can be observed only in modified and functionalized nanoparticles. At 3300 cm^{-1}, N-H stretching peak is disguised by O-H stretching peak. However, it affects O-H stretching peak profile, that is

different comparing the peaks of unmodified silica nanoparticles with modified and functionalized nanoparticles, thus confirming the success of the followed protocols for each reaction. At 1630 cm^{-1} and 2350 cm^{-1}, intense peaks characteristic of samples' contamination with water and CO_2 emerge.

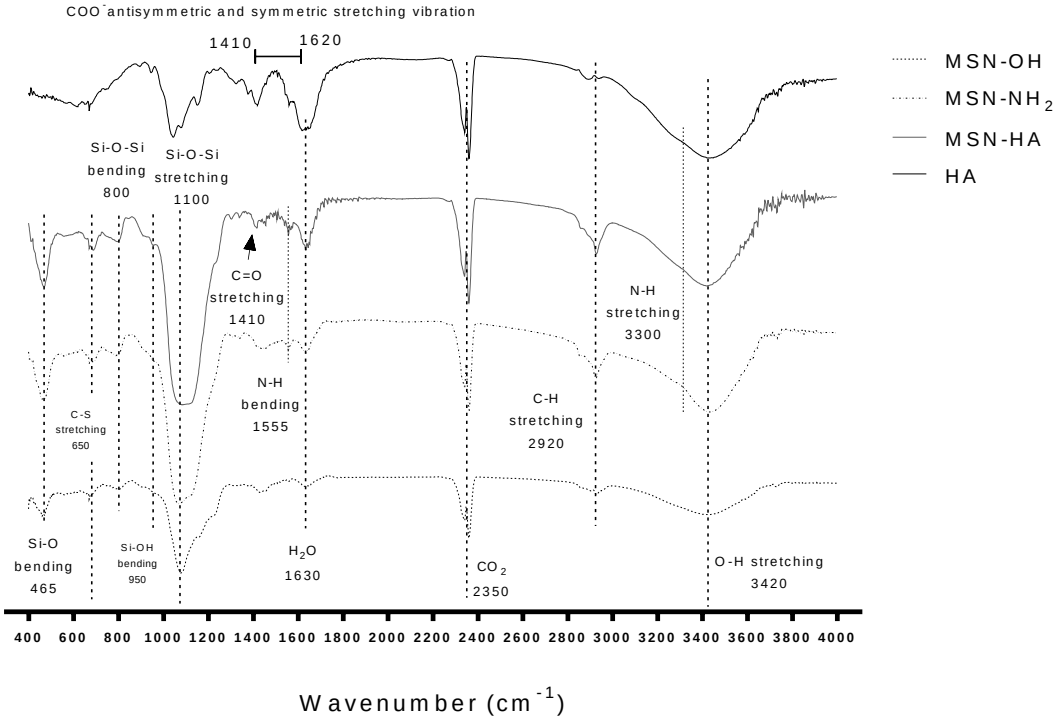

Figure 19- FTIR analysis of the functional groups present on unmodified (MSN-OH), modified (MSN-NH_2) and functionalized (MSN-HA) mesoporous silica nanoparticles.

4. Recombinant IFNα-2b

4.1 Recombinant IFNα-2b characterization

The field of Bioinformatics is gaining a significant relevance in life sciences and medical research. Computational algorithms and other informatic tools are allowing faster and more accurate data analysis, contributing for the current biotechnological growing progress. Online tools from the National Center for Biotechnology Information (NCBI), such as BLAST and COBALT, present reliable results linked to other online databases, such as UniProt and Protein Data Bank (PDB), references of excellency for data and text mining.

As described in section 2.1 of the Materials and Methods chapter, this is a synthetic sequence modified in order to allow the expression of a soluble and active IFNα-2b in a prokaryotic system and to optimize the protein's affinity towards its

receptors, favouring the modified IFNα-2b interaction with IFNAR1 instead of IFNAR2. This triggers a most expressive response via activating the JAK–STAT pathway, enhancing antitumour immunity. (Zhang *et al.*, 2017). Accordingly, to the information presented in NCBI about IFNα-2b, this protein is constituted by 188 amino acids and has a molecular weight of 21.55 kDa. However, the sequence inserted in the plasmid, represented in Figure 20, has 274 amino acids, a molecular weight of 31.8 kDa and a pI of 5.8.

MGHHHHHHMSDSEVNQEAKPEVKPEVKPETHINLKVSD
GSSEIFFKIKKTTPLRRLMEAFAKRQGKEMDSLRFLYDGI
RIQADQTPEDLDMEDNDIIEAHREQIGGQGSCDLPQTHS
LGSRRTLMLLAQMRKISLFSCLKDRHDFGFPQEEFGNQ
FQKAETIPVLHEMIQQIFNLFSTKDSSAAWDETLLDKFYT
ELYQQLNDLEACVIQGVGVTETPLMKEDSILAVRKYFQRI
TLYLKEKKYSPCAWEVVRAEIMRSFSLSTNLQESLRSKE

Figure 20- Synthetic IFNα-2b amino acid sequence inserted into pSMART® HCKan plasmid.

Thus, the synthetic IFNα-2b sequence provided by GeneCust was analysed using BLAST and relevant information was extracted. Looking at sequence's conserved domains, it was possible to verify that besides the Interferon hit, another protein was found to be present in the synthetic IFNα-2b sequence. Considering the listed accession codes and after cross-referencing with PDB in Europe database, that protein identity was found to match with the Small Ubiquitin-Related Modifier (SUMO). SUMO protein (also known as "Smt3" and "sentrin" in other organisms) is conjugated to numerous intracellular targets and serve to modulate protein interaction, localization, activity or stability. Also, SUMO is linked to several different pathways, including nucleocytoplasmic transport. Attachment of SUMO to targets proteins is stimulated by PIAS (Protein inhibitor of activated STATs) proteins which serve as E3-like ligases. Chain A of SUMO protein presents a length of 78 amino acids and a theoretical weight of 9.06 kDa (PDBe code: 1wm2). Therefore, all the protein structure was maintained in order to promote IFNα-2b stability and solubility when expressed in the prokaryotic cells.

For uncovering more clues about IFNα-2b sequence, protein's NCBI accession number (P01563) was crossed-referenced in UniProt Database, showing the presence of two disulphide bonds between residues 24-121 and 52-161 and a glycosylation site at threonine residue 129. Finally, the translated sequence from the sequencing result and the one provided by protein's NCBI accession number were aligned using BLAST and then their multiple alignment was performed using COBALT. Multiple alignment result, expressed in Figure 21, has uncovered all the content in both sequences and the

molecular manipulation executed by GeneCust, such as the histidine tag, SUMO protein, a modified signal peptide and the sequence of IFNα-2b.

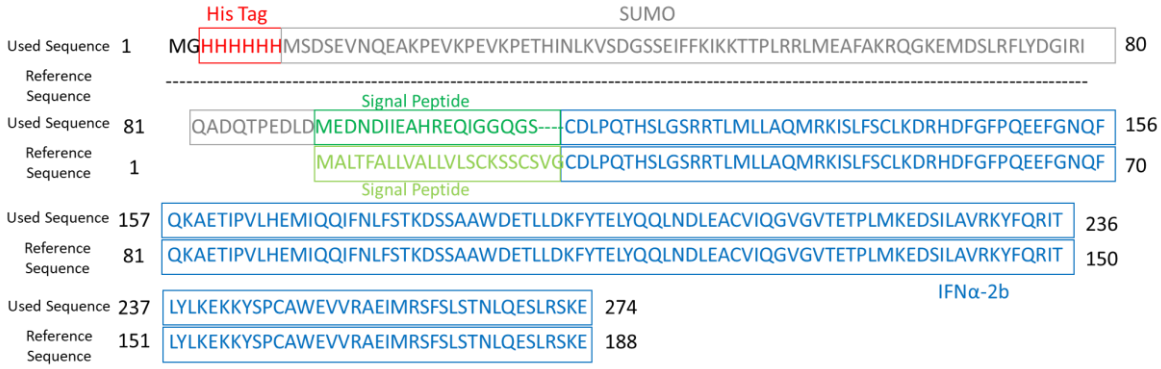

Figure 21- Multiple alignment between protein sequenced sequence the reference sequence using Constraint-based Multiple Alignment Tool (COBALT).

4.2 Recombinant IFNα-2b production and purification

Initially, competent *E. coli* strains were transformed with the pSMART® HCKan plasmid as described in the Materials and Methods section of this work and grown in LB + agar plates in the presence of kanamycin. Isolated colonies of BL21 Star® strain were picked and grown in LB medium also containing the selective antibiotic. Then, an expression research was made in order to determine which colony successfully produced soluble IFNα-2b.

A pre-induce culture was prepared from an aliquot of a BL21 Star® as mentioned in topic 2.5 at this work Materials and Method's chapter and then poured into 500 mL of LB medium containing 30 µg/mL kanamycin. The culture was grown at 37 ºC and 0.2 mM IPTG was added when the O.D. value of the cell culture was between 0.6-0.8 a.u.. However, this culture was grown overnight at approximately 20 ºC. Then, cells were recovered and suspended in PBS and frozen at -20 ºC overnight. The cells were placed on ice to unfreeze for 1 hour and then sonicated in a slushy state with macroscopic ice crystals, as an attempt of increasing the yield of cell bursting due to the mechanical action of ice crystals against cells wall and membrane, contributing to a bigger recovery of soluble protein by the end of this step. Then, insoluble cellular content and inclusion bodies were once again precipitated and the soluble fraction directly loaded into the purification column. The column was eluted just with PBS supplemented with 500 mM Imidazole, after its washing with PBS supplemented with 20 mM Imidazole. The respective chromatogram is represented in Figure 22, as well as the collected samples

into each Falcon Tube. Respective protein profile analysis by SDS-PAGE is represented in Figure 23.

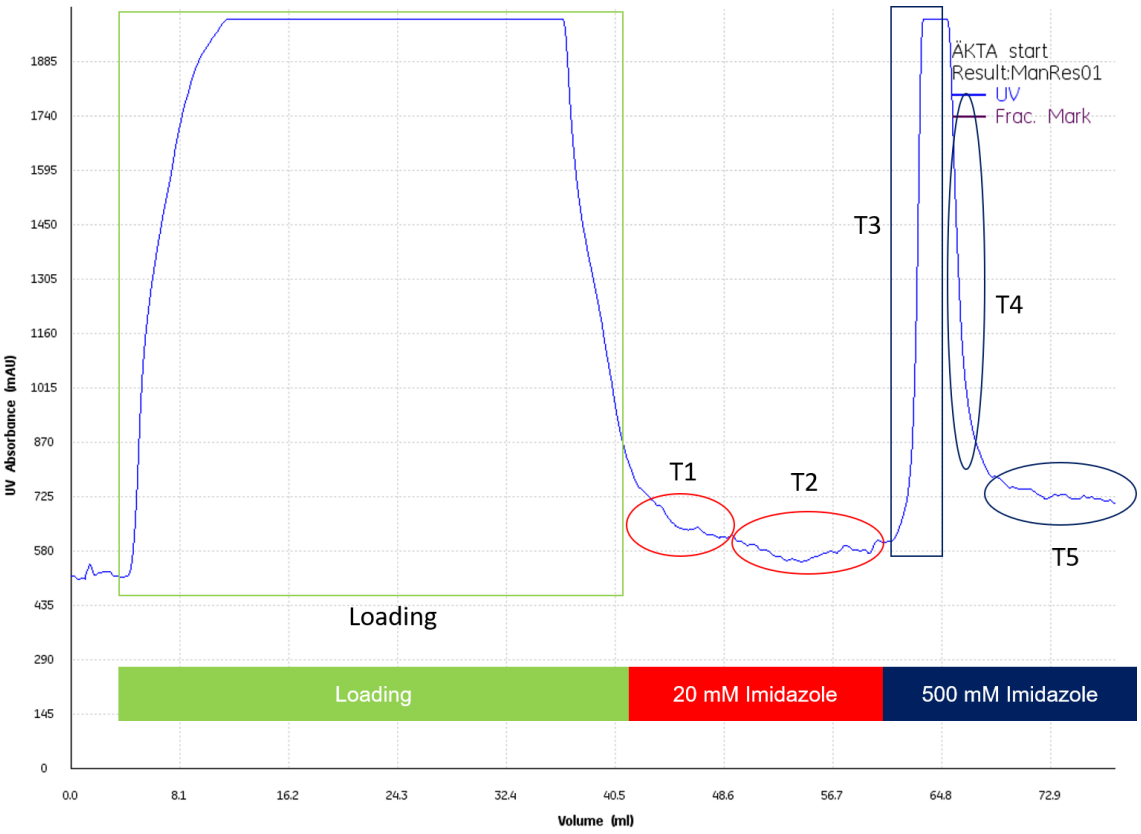

Figure 22- Chromatogram from IFNα-2b production, from an IMAC affinity chromatography with a 5 mL HisTrap HP histidine-tagged protein purification column, which has been washed with PBS supplemented with 20 mM Imidazole and later eluted with PBS supplemented with 500 mM Imidazole.

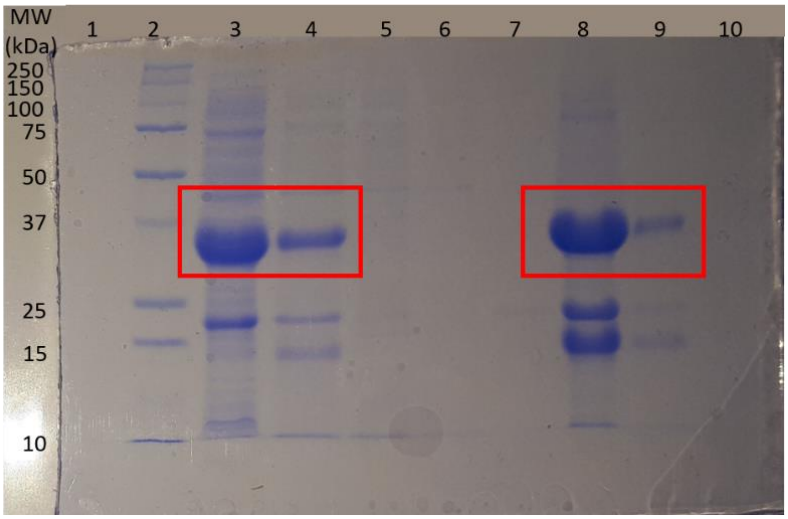

Figure 23- SDS-PAGE gel containing the resulting liquid fractions from IFNα-2b production and purification. 1- Empty; 2- Protein Ladder; 3- Insoluble Fraction; 4- Soluble Fraction; 5- Flow through; 6- T1 (20 mM Imidazole); 7- T2 (20 mM Imidazole); 8- T3 (500 mM imidazole); 9- T4 (500 mM Imidazole); 10- T5 (500 mM Imidazole).

The results show the presence of soluble IFNα-2b not only in the insoluble fraction but also in the soluble fraction, below 37 kDa. They also show that the desired protein is only collected when PBS supplemented with 500 mM Imidazole elutes the previously loaded purification column. These results indicate that the histidine tag included in the structure of the IFNα-2b successfully interacts with the nickel ions existent in the chelating agent that couples with highly cross-linked agarose beads that constitute the purification column, and that only a compound with more affinity for this ion can cause the elution of the trapped protein. However, protein profiles of wells 8 and 9 indicate the presence of contaminants that were collected simultaneously with the desired protein. Thus, for obtaining purer fractions, column's elution with PBS supplemented with 100 mM Imidazole must be mandatory.

For determining protein concentration collected in each fraction, the Bradford Method was applied. T3 fraction presented a concentration of 12.59 mg/mL and T4 fraction presented a concentration of 0.87 mg/mL. Considering an expression volume of 500 mL, a good amount of protein was obtained following this methodology. Fractions T3 and T4 were dialysed against PBS and freeze-dried.

4.3 Optimization of IFNα-2b production

After establishing the basic procedures required for successfully producing and purifying the desired recombinant protein, a few optimizations for increasing the recombinant human IFNα-2b production and recovery yield were immediately drawn. Recombinant protein production using the pSMART® HCKan plasmid was promoted at lower incubation temperatures. A pre-induce culture was poured into 500 mL of LB medium containing 30 µg/mL kanamycin and grown at 37 ºC for 1 hour and a half. Then, the incubator's temperature was lowered to approximately 20 ºC because with approximately 1 hour and a half still remaining for 0.2 mM IPTG addition, the incubator had more time to lower its internal temperature, thus ensuring that the protein expression will immediately begin at a lower temperature than in previous conditions. The only disadvantage of lowering incubation temperature while growing the pre-induce culture is a lower population growth because cells weren't at their optimal temperature conditions (37 ºC). But, since the cells continue to replicate themselves while expressing the desired protein, that issue is irrelevant to the final result.

Then, cells were frozen, lysed and purified in conditions mentioned in the respective topics 3.1 and 3.2 of this work's Material and Methods chapter. However, in the purification process, fractions were collected considering a smaller volume per

Falcon tube (2-3 mL) in an attempt to better isolate the pure fractions of the desired protein. The chromatogram of this optimized protein expression is represented in Figure 24, as well as the collected samples into each Falcon Tube. The respective protein profile analysis by SDS-PAGE is represented in Figures 25 and 26.

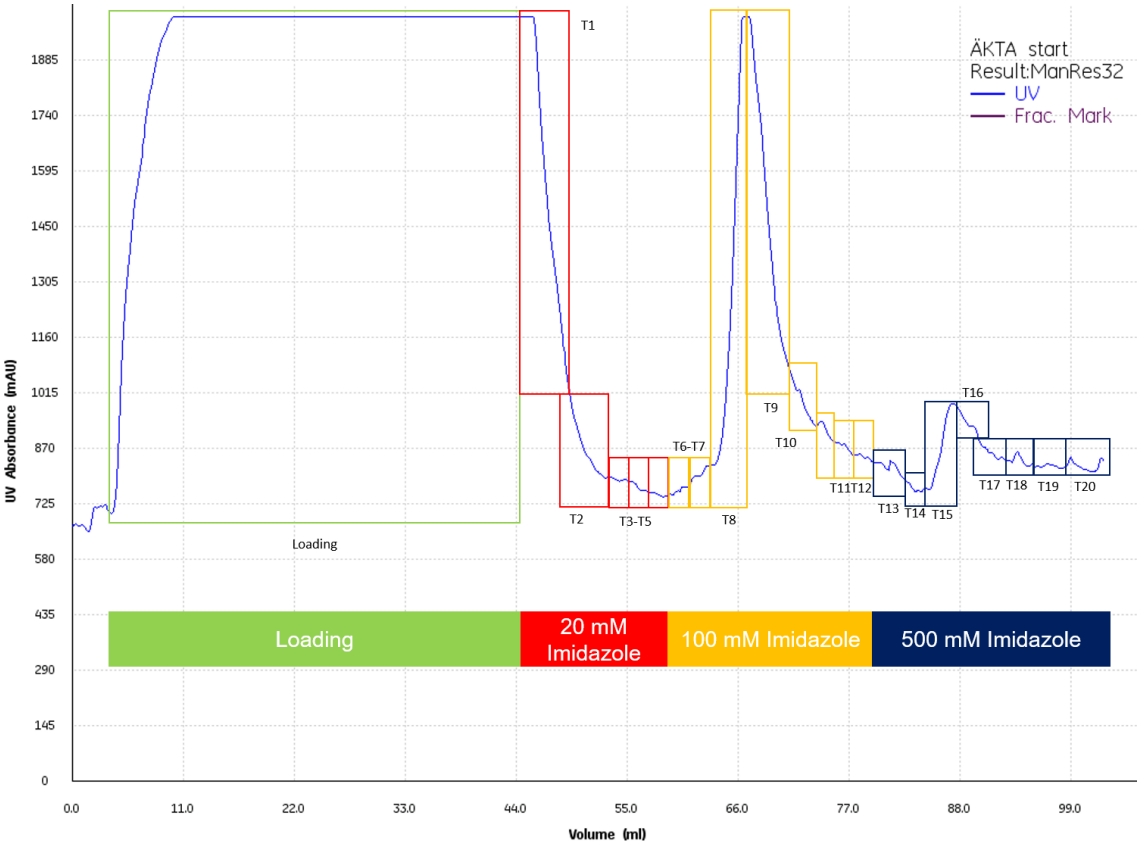

Figure 24- Chromatogram of the optimization of IFNα-2b production, from an IMAC affinity chromatography with a 5 mL HisTrap HP histidine-tagged protein purification column, which has been washed with PBS supplemented with 20 mM Imidazole and later eluted with PBS supplemented with 100mM Imidazole and 500 mM Imidazole.

The results in Figure 25 show that the soluble fraction contains significant amounts of IFNα-2b, but also some insoluble protein can be found. The absence of any band in the region next to 37 kDa in Figure 25, wells 4 and 5, proves once again the efficiency of the interaction between the nickel ions and the protein's histidine tag while column's loading with the soluble fraction and washing with PBS supplemented with 20 mM Imidazole. Fractions of the desired recombinant protein are only collected when PBS supplemented with 100 mM Imidazole elutes the purification column, and a pure fraction of the recombinant human IFNα-2b is collected after the column's elution with the PBS supplemented with 500 mM Imidazole.

Looking to protein profiles of Figure 26, the increased number of collected samples with smaller eluted volumes sequentially allowed the increase of protein purity degree throughout the fractions. Protein concentrations of the fractions eluted with 100 mM Imidazole and 500 mM Imidazole were determined using the Bradford Method: Fraction T8- 11.32 mg/mL; Fraction T9- 6.86 mg/mL; Fraction T10- 3.28 mg/mL; Fraction T11- 1.43 mg/mL; Fraction T12: 2.11 mg/mL; Fraction T15- 4.05 mg/mL; Fraction T16- 1.91 mg/mL; Fraction T17- 0.38 mg/mL and Fraction T18- 0.04 mg/mL. These results show that following this methodology, recombinant human IFNα-2b production and purification yields are increased.

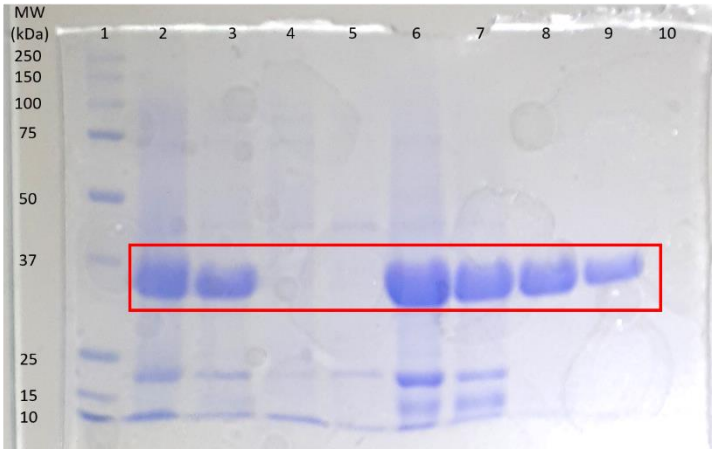

Figure 25 – SDS-PAGE gel containing the resulting liquid fractions from the optimization of IFNα-2b production and purification. 1- Protein Ladder; 2- Insoluble Fraction; 3- Soluble Fraction; 4- Flow Through; 5- T2 (20 mM Imidazole); 6- T8 (100 mM Imidazole); 7- T9 (100 mM Imidazole); 8- T15 (500 mM Imidazole); 9- T16 (500 mM Imidazole); 10- Empty.

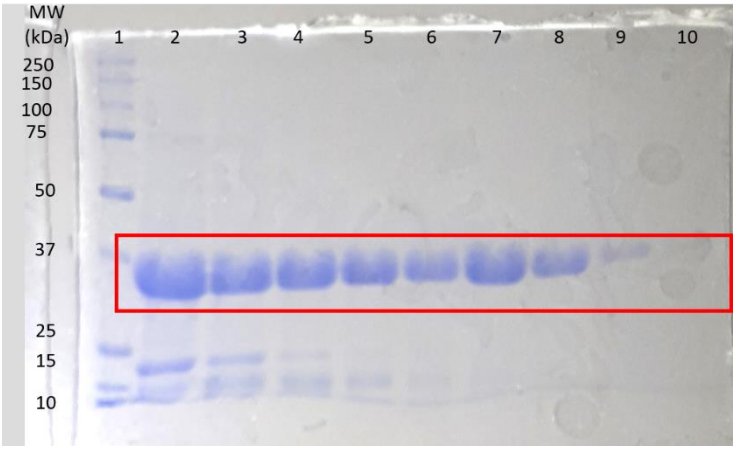

Figure 26- SDS-PAGE gel gel containing the resulting liquid fractions from the optimization of IFNα-2b production and purification, focusing on the collected liquid fractions. 1- Protein Ladder; 2- T8 (100 mM Imidazole); 3- T9 (100 mM Imidazole); 4- T10 (100 mM Imidazole); 5- T11 (100 mM Imidazole); 6- T12 (100 mM Imidazole); 7- T15 (500 mM Imidazole); 8- T16 (500 mM Imidazole); 9- T17 (500 mM Imidazole); 10- T18 (500 mM Imidazole).

In order to increase the yield of pure protein recovery by the end of the production and purification processes, a second IMAC affinity chromatography was performed using the fractions containing high concentrations of the desired protein with contaminants, collected after column's elution with PBS supplemented with 100 mM Imidazole. Impure dried protein samples were re-solubilized with PBS and liquid fractions containing 100 mM Imidazole were approximately diluted 5 times and once again chromatographed and purified following the optimized purification protocol mentioned in topic 3.2 of this work's Materials and Methods chapter. The chromatogram represented in Figure 27, shows the general profile of all chromatographed fractions. Respective protein profiles are represented in Figure 28.

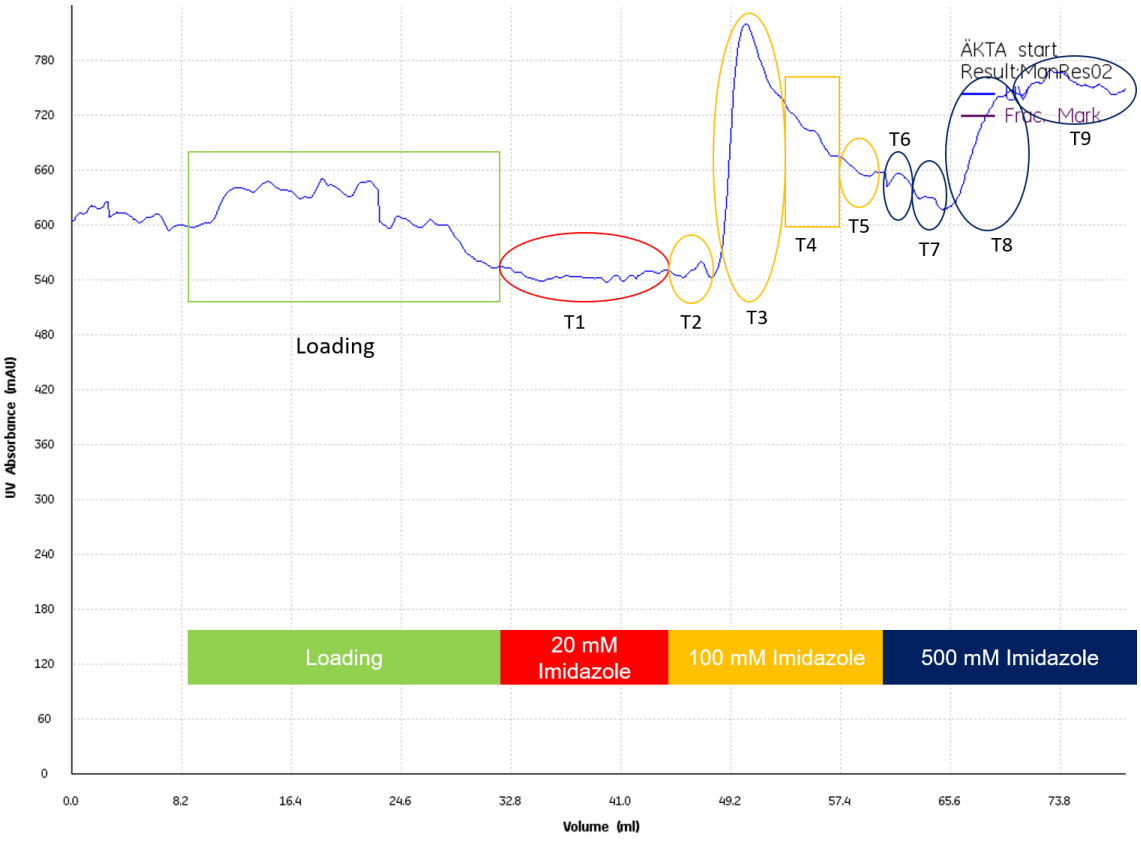

Figure 27- Chromatogram of the optimization of IFNα-2b production, from a second IMAC affinity chromatography, with a 5 mL HisTrap HP histidine-tagged protein purification column, which has been washed with PBS supplemented with 20 mM Imidazole and later eluted with PBS supplemented with 100mM Imidazole and 500 mM Imidazole.

Looking at Figure 27, the profile of the represented chromatogram is similar to one represented in Figure 24. However, peaks' intensity is lower in this case because the starting amount of available protein is lower as well. Column's elution with 100 mM Imidazole also causes the same large base peak, indicating that a significant amount of IFNα-2b may be being collected. The protein profile in Figure 28 proves that column's

elution with PBS supplemented with 500 mM Imidazole allows the collection of protein with a purity degree superior to 80%. Thus, these results prove that impure fractions can be once again chromatographed and purified and that even more amounts of pure protein can be extracted from impure fractions. However, a new purification process leads to an inevitable protein loss due to protein's unspecific interaction with the tube's polymer and this issue must always be accounted for. Anyway, approximately 94 mg of IFNα-2b are produced considering an expression volume of 500 mL, of which 19 mg are have a purity degree superior to 80%.

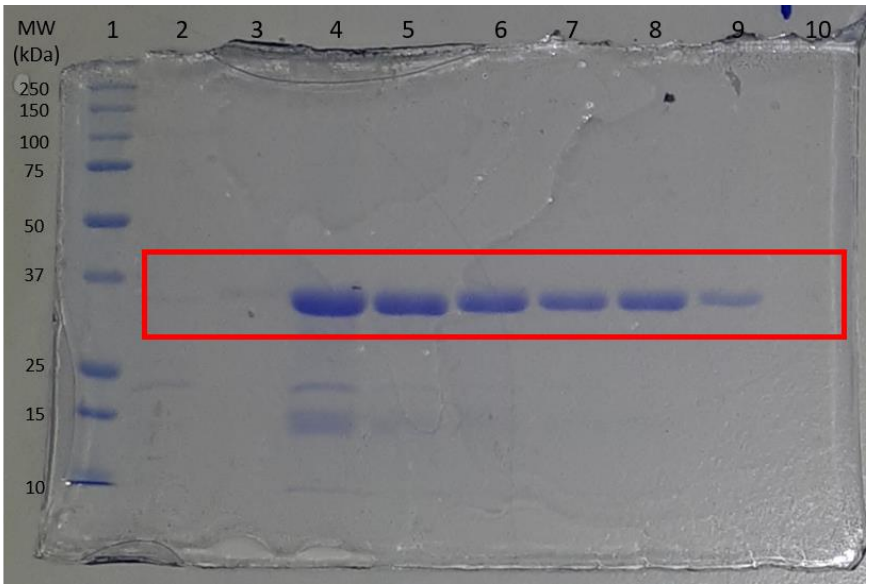

Figure 28- SDS-PAGE gel containing the liquid fractions of the second IMAC affinity chromatography. 1- Protein Ladder; 2- Flow Through; 3- T2 (100 mM Imidazole); 4- T3 (100 mM Imidazole); 5- T4 (100 mM Imidazole); 6- T5 (100 mM Imidazole); 7- T6 (500 mM Imidazole); 8- T7 (500 mM Imidazole); 9- T8 (500 mM Imidazole); 10- T9 (500 mM Imidazole).

5. IFNα-2b Loading into Mesoporous Silica Nanoparticles

Protein loading experiments were performed after successfully functionalizing mesoporous silica nanoparticles with HA and producing IFNα-2b with a purity degree superior to 80%. The experimental design was redrawn considering the experience gained with BSA loading studies, leading to the establishment of the optimal ratio between the amount of loaded protein and mass of nanoparticles used. Lower amounts of protein and mesoporous silica nanoparticles were used, and the dispersion volume was also smaller, compared with the methodology applied in the BSA adsorption studies. Also, instead of using a 15 mL Falcon for the loading reaction dispersion, a 2 mL Eppendorf tube was used. Two loading timepoints were considered because adsorption efficiency could be influenced by the incubation time and no information regarding

overnight incubation was present in the applied methodology (Shi *et al.*, 2019). In the BSA adsorption studies, unmodified mesoporous silica nanoparticles presented a loading efficiency of 21.29% and the functionalized ones 10.86%, considering a ratio of 8 mg of BSA per 20 mg of nanoparticles. Loading capacity of unmodified nanoparticles was 8.52% and 3.48% for the functionalized ones.

Thus, considering the new methodologic approach, a ratio of 0.064 mg of IFNα-2b per 1.4 mg of nanoparticles was tested. Briefly, 20 µL of dialysed protein against ultra-pure water and PBS and then rehydrated were added to 200 µL of dispersed nanoparticles. Samples of all types of mesoporous silica nanoparticles (unmodified- MSN-OH; modified- MSN-NH_2 and functionalized- MSN-HA) were incubated for approximately 10 seconds and overnight and their supernatant's protein content was determined using the Bradford Method. Applying equations 1 and 2, protein loading efficiency (LE) and loading capacity (LC) were determined and are presented in Figure 29. The results show that unmodified and modified mesoporous silica nanoparticles presented 100% of loading efficiency regardless of protein dialysis buffer and incubation times. Protein's structural memory due to its previous solubilization in PBS might be contributing to these results because protein's relaxation state is influenced by the conditions of the surrounding environment, such as ionic strength and pH, and binding affinity (Xu, Ca and Hamm, 2016). So, regardless of the surrounding environment (ultra-pure water or PBS), IFNα-2b relaxation state remains unaltered or changes very slowly when this protein is adsorbed by HA. Loading capacity values are variable but constantly repeated: the highest ones are verified in samples on which protein was dialysed against ultra-pure water (approximately 4%) and the lowest ones are for protein dialysed against PBS (approximately 2 %) This variation is due the contribution of the PBS salts in the initial protein weighing. Slightly different results were obtained for functionalized nanoparticles. Higher values of loading efficiency were promoted by overnight incubation, and the sample whose protein was dialysed against PBS presented 100% of loading efficiency, unlike the 90% Loading efficiency percentage of the sample whose protein was dialysed against ultra-pure water. However, regarding nanosystem's loading capacity, the sample whose protein was dialysed against ultra-pure water and incubated overnight presented the better result amongst all samples, 3.74 % of loading capacity.

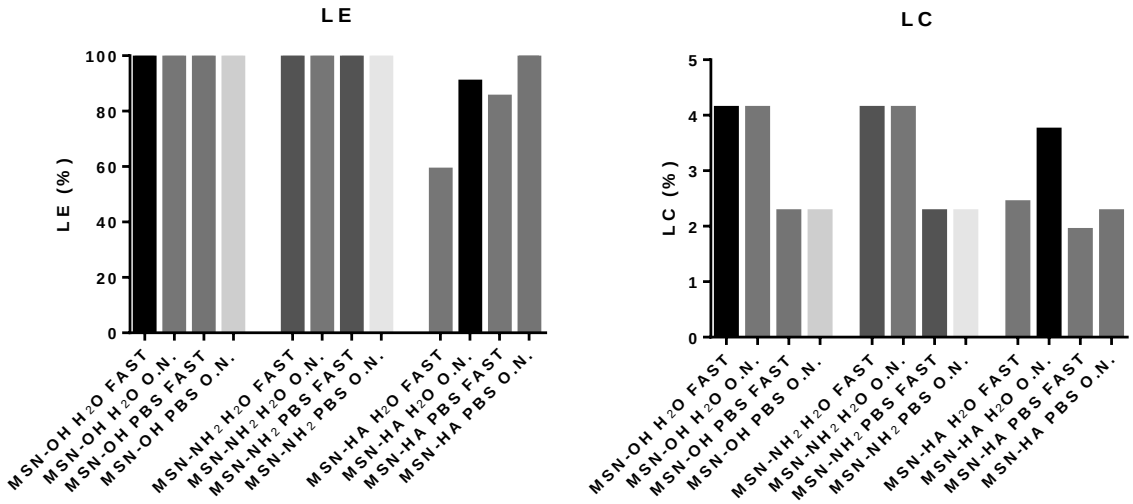

Figure 29- Protein loading efficiency (LE) and loading capacity (LC) considering protein dilution in ultra-pure water and PBS and two distinct incubation times: "FAST" samples were incubated for 10 seconds before supernatant collection and "O.N." samples were incubated overnight for approximately 16 hours before supernatant collection.

These results suggest that this new methodology dramatically increases protein loading efficiency, probably due to a more effective nanoparticle dispersion that promotes more successful interactions between nanoparticles and protein, and also to the fact of being using approximately 10 times less amount of protein than nanoparticles. Overnight samples containing functionalized nanoparticles presented higher loading efficiency probably because of the mucoadhesive properties of HA (Kim *et al.*, 2019) and because of the fact that pores might be partially obstructed by HA, turning protein entrance into the pores and general loading more challenging. At pH 7.53, the produced IFNα-2b is negatively charged, so, it may take some time for repulsive forces between the polysaccharide hydroxide groups and protein charge to be nullified by Van der Waals interactions (Nairi *et al.*, 2018).

Loading capacity values of the unmodified nanoparticles used in this experiment are approximately half of the ones determined in BSA loading studies due to the lower amount of protein used in this situation. Samples whose protein was dialysed against PBS presents even lower loading capacity values for all types of nanoparticles. Thus, buffer salts are a big influence in protein's weighting and lower amounts of protein are being loaded into the nanosystem. Considering equation 2, this issue must be a key factor for the different loading capacity values and for controlling this variable, all used protein must be dialysed only against ultra-pure water. Loading capacity values also suggest that greater amounts of protein can be loaded into the nanoparticles without compromising the efficiency of the process.

Considering the conclusions above, a new loading ratio – 0.2 mg of IFNα-2b per 2.0 mg of nanoparticles – was tested. The scale-up experiment described in this work's Materials and Methods section was performed and the results are shown in Figure 30.

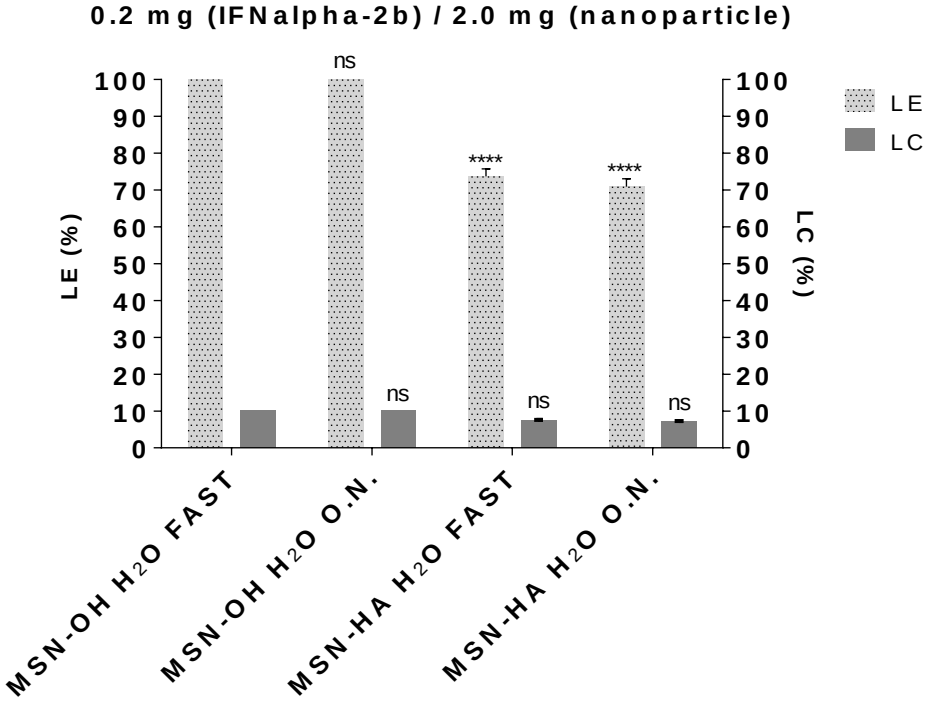

*Figure 30- Protein loading efficiency (LE) and loading capacity (LC) considering protein dilution in ultra-pure water and two distinct incubation times: "FAST" samples were incubated for 10 seconds before supernatant collection and "O.N" samples were incubated overnight for approximately 16 hours before supernatant collection. Data are expressed as mean ± SEM of 2 independent experiments. ****: p ≤ 0.0001, ***: p≤0.001, **: p≤0.01, *: p≤0.05, ns: p>0.05, with p being calculated using ordinary two-way ANOVA test with Tukey's multiple comparisons test.*

The results of the scale-up experiment confirm the previous assumptions made about protein loading efficiency and loading capacity. Once again, protein loading efficiency of unmodified nanoparticles was 100% regardless of the incubation time. This value highlights their immense adsorbance potential that could occur either in the outer surface or into nanoparticles' pores (Slowing, Trewyn and Lin, 2007; Tu *et al.*, 2016). However, considering this new ratio, protein loading efficiency and loading capacity of tested samples presented different patterns. Unmodified nanoparticles achieved a loading capacity of 10.02% and functionalized nanoparticles "FAST" and "O.N." samples achieved a loading capacity of 7.39 ± 0.20% and 7.11 ± 0.210%, respectively. Functionalized nanoparticles "FAST" and "O.N." samples present a loading efficiency of 73.75 ± 1.98 % and 70.95 ± 2.13%, respectively. This shows that incubation time practically didn't influenced protein loading in the same way as verified with the previous ratio, 0.064 mg of IFNα-2b per 1.4 mg of nanoparticles.

A recent study explored protein loading efficiency into mesoporous silica nanoparticles and determined nanosystem's loading capacity (Tu *et al.*, 2016). In that study, authors followed a very similar methodology comparing with the one used in this work: unmodified mesoporous silica nanoparticles were dispersed recurring to ultrasounds and adsorption studies were performed following the immersion method, considering a protein/nanoparticles ratio of 1:4, i.e., 250 mg of protein per 1 g of nanoparticles. Several different proteins with different physicochemical parameters, such as size, molecular weight and pI, were solubilized in 1 mM phosphate buffer, at room temperature, and incubated for 20 minutes under gentle agitation. An average protein loading efficiency of 97% was obtained, as well as an average loading capacity of 20%. When the authors tested a ratio of 1:1 (10 times higher than the last ratio tested, 0.2:2.0), average protein loading efficiency dropped to 54% but average loading capacity increased to 53%. So, these results support the ones shown in this work because the same pattern regarding loading efficiency/loading capacity and protein/nanoparticles ratio is verified. Thus, increasing the amount of loaded protein will cause an increment in system's loading capacity, but protein loading efficiency will consequently decrease due to the protein excess that won't be loaded into the nanosystem.

Chapter IV

Conclusions

The development of new drug delivery systems and new chemotherapy strategies are a major priority for clinical research. Now, probably more than ever, are available incredible technological tools that accelerate and facilitate research work in astonishing ways. Scientific knowledge can synergistically use technological tools in order to address the current problems related with conventional chemotherapy strategies. The main objective of this work was to develop and characterize a new drug delivery system capable of transporting and delivering a recombinant protein for a potential clinical use in HCC treatment. Thus, a mesoporous silica nanoparticle functionalized with hyaluronic acid was developed and loaded with a soluble recombinant human protein, Interferonα-2b (IFNα-2b), whose function is to induce cellular death through apoptotic pathways.

Mesoporous silica nanoparticles were successfully synthesized but presented an average hydrodynamic diameter higher than expected. This suggests that aggregation issues must be the cause for the measured values. Surfactant was also successfully removed because unmodified silica nanoparticles presented a negative ζ-potential. Before functionalizing mesoporous silica nanoparticles with HA, two surface modifications approaches were tested: one using GPTS and another using APTES. The functionalization reaction of GPTS-modified nanoparticles was unsuccessful probably because of the methodology followed. BSA adsorption studies shown that unmodified nanoparticles could adsorb protein. Functionalization reaction in APTES-modified nanoparticles proved to be successful and reliable. ζ-potential measurements shown the expected shifts in voltage values, reflecting the positive charge of APTES-modified nanoparticles, provided by the amine group, and the negative charge of APTES-modified functionalized nanoparticles by the hydroxide groups of HA. FTIR spectrums of unmodified, APTES-modified and functionalized nanoparticles show the characteristic peaks profile expected for each nanoparticle formulation, thus supporting the previous results.

The desired protein, IFNα-2b, was successfully produced and purified from BL21 Star® strain and purification by an IMAC affinity chromatography allowed the collection of approximately 19 mg of protein with a purity degree superior to 80%. Approximately 94 mg of IFNα-2b are produced considering an expression volume of 500 mL.

Finally, nanoparticles loading experiments with the produced IFNα-2b shown that all types of nanoparticles can adsorb protein. Loading capacity shown to be unaffected regardless of the solvent used and the incubation time. However, considering the final protein/nanoparticles ratio (0.2 mg of IFNα-2b per 2.0 mg of nanoparticles), loading efficiency for functionalized nanoparticles decreased from 100% to approximately 70%, i.e. a reduction of approximately 30%. For unmodified nanoparticles, loading capacity value was 10% and for the functionalized ones was approximately 7%. Loading capacity increases with an inevitable decrease of protein loading efficiency percentage and it is only possible to compromise loading efficiency percentage until a certain threshold. Loading capacity is directly dependent of the protein amount used for nanoparticle's loading.

Overall, it can be concluded that the main objective of this work was successfully achieved but there are some aspects that might be clarified and also some new experiments to consider. The first issue to be addressed is the great nanoparticle aggregation described in this work. Perhaps, sonication equipment should be replaced because its current condition may be compromising experimental conditions. Another issue that might be crucial for future experiments is increasing the amount of nanoparticles used in modification and functionalization reactions to compensate the inevitable loss of nanoparticles mass during the reactions, respective washes and freeze-drying process. The same reasoning should be applied to the protein production, because in spite of the high production and collection yields, a great stock of dried protein is recommended for a more methodical use in future experiments. Another key issue should be increasing the functionalized nanosystem's loading capacity in order to protein releasing experiments could be performed. Nanosystem trafficking experiments through confocal microscopy could also be performed in order to evaluate if the nanosystem interacts with the cellular membranes, if it is internalized by HCC representative cell lines and, if so, identify nanosystem's major accumulation sites inside the cells. The collection of TEM and SEM images of the nanosystem could also reveal the individual diameter of mesoporous silica nanoparticles and actually confirm the presence of aggregated nanoparticles. Finally, an evaluation of cytotoxicity and proliferation of HCC representative cell lines treated with the new drug delivery system developed in this work could present the first step for the development of a new, safer and specific anticancer strategy.

Chapter V

References

Au-Yeung, N., Mandhana, R. and Horvath, C. M. (2013) 'Transcriptional regulation by STAT1 and STAT2 in the interferon JAK-STAT pathway', *Jak-Stat*, 2(3), p. e23931. doi: 10.4161/jkst.23931.

Aubrey, B. J., Strasser, A. and Kelly, G. L. (2016) 'Tumor-Suppressor Functions of the TP53 Pathway'.

Batista, C. A. S., Larson, R. G. and Kotov, N. A. (2015) 'Nonadditivity of nanoparticle interactions', 350(6257). doi: 10.1126/science.1242477.

Bergmann, J. *et al.* (2017) 'IL-6 Trans-Signaling Is Essential for the Development of Hepatocellular Carcinoma in Mice', 65(1). doi: 10.1002/hep.28874.

Bradford, M. M. (1976) 'A Rapid and Sensitive Method for the Quantitation Microgram Quantities of Protein Utilizing the Principle of Protein-Dye Binding', 254, pp. 248–254.

Cabello, C. M. *et al.* (2010) 'Protein Database Searches Using Compositionally Adjusted Substitution Matrices', *Febs J.*, 46(2), pp. 220–231. doi: 10.1016/j.freeradbiomed.2008.10.025.The.

Cells, C. (2008) 'Inhibition of JAK1 , 2 / STAT3 Signaling Induces Apoptosis , Cell Cycle Arrest , and Reduces Tumor Cell Invasion in Colorectal', 10(3), pp. 287–297. doi: 10.1593/neo.07971.

Chemgaroo (no date) *Carboxylic Acid Derivatives - Formation of Carboxamides*. Available at: http://www.chemgapedia.de/vsengine/vlu/vsc/en/ch/12/oc/vlu_organik/c_acid/carbons_und_derivate.vlu/Page/vsc/en/ch/12/oc/c_acid/amidbildung/amidbildung.vscml.html (Accessed: 22 July 2019).

Chen, F. *et al.* (2018) 'Multifunctional nanomedicine with silica: Role of silica in nanoparticles for theranostic, imaging, and drug monitoring', *Journal of Colloid and Interface Science*. Elsevier Inc., 521, pp. 261–279. doi: 10.1016/j.jcis.2018.02.053.

Chu, L., Daniels, M. W. and Francis, L. F. (1997) 'Use of (Glycidoxypropyl) trimethoxysilane as a Binder in Colloidal Silica Coatings', 1(10), pp. 2577–2582. doi:

10.1021/cm9702880.

Clemments, A. M., Botella, P. and Landry, C. C. (2017) ‘Spatial Mapping of Protein Adsorption on Mesoporous Silica Nanoparticles by Stochastic Optical Reconstruction Microscopy (STORM) Spatial Mapping of Protein Adsorption on Mesoporous Silica Nanoparticles by Stochastic Optical Reconstruction Microscopy (S’. doi: 10.1021/jacs.7b01118.

Cohen, Stanley N., Chang, Annie C., Hsu, L. (1972) ‘Nonchromosomal Antibiotic Resistance in Bacteria: Genetic Transformation of Escherichia coli by R-Factor DNA’, *Proceedings of the National Academy of Sciences*, 69(8), pp. 2110–2114. doi: 10.1073/pnas.69.8.2110.

Crisler, William J and Lenz, L. L. (2018) ‘Crosstalk between type I and II interferons in regulation of myeloid cell responses during bacterial infection’, *Current Opinion in Immunology*. Elsevier Ltd, 54, pp. 35–41. doi: 10.1016/j.coi.2018.05.014.

Crisler, William J. and Lenz, L. L. (2018) ‘Crosstalk between type I and II interferons in regulation of myeloid cell responses during bacterial infection’, *Current Opinion in Immunology*. Elsevier Ltd, 54, pp. 35–41. doi: 10.1016/j.coi.2018.05.014.

Dahirel, V. and Jardat, M. (2010) ‘Effective interactions between charged nanoparticles in water: What is left from the DLVO theory?’, *Current Opinion in Colloid and Interface Science*. Elsevier Ltd, 15(1–2), pp. 2–7. doi: 10.1016/j.cocis.2009.05.006.

Dhar, D. *et al.* (2018) ‘Liver Cancer Initiation Requires p53 Inhibition by Article Liver Cancer Initiation Requires p53 Inhibition by CD44-Enhanced Growth Factor Signaling’, *Cancer Cell*. Elsevier Inc., 33(6), pp. 1061-1077.e6. doi: 10.1016/j.ccell.2018.05.003.

Dubois, M. *et al.* (1956) ‘Colorimetric Method for Determination of Sugars and Related Substances’, pp. 350–356. doi: 10.1021/ac60111a017.

Dutta, R. and Mahato, R. I. (2017) ‘Recent advances in hepatocellular carcinoma therapy’, *Pharmacology and Therapeutics*. Elsevier Inc., 173, pp. 106–117. doi: 10.1016/j.pharmthera.2017.02.010.

Farina, Nicholas H *et al.* (2018) ‘Nanoparticle-based targeted cancer strategies for non-invasive prostate cancer intervention’, (March), pp. 6408–6417. doi: 10.1002/jcp.26593.

Farina, Nicholas H. *et al.* (2018) ‘Nanoparticle-based targeted cancer strategies for non-invasive prostate cancer intervention’, *Journal of Cellular Physiology*, 233(9), pp. 6408–6417. doi: 10.1002/jcp.26593.

Ford, K. G. *et al.* (2001) 'Protein transduction : an alternative to genetic intervention ?', pp. 1–4.

Fu, C. *et al.* (2013) 'The absorption, distribution, excretion and toxicity of mesoporous silica nanoparticles in mice following different exposure routes', *Biomaterials*. Elsevier Ltd, 34(10), pp. 2565–2575. doi: 10.1016/j.biomaterials.2012.12.043.

Gupta, G. P. and Massagué, J. (2006) 'Cancer Metastasis: Building a Framework', *Cell*, 127(4), pp. 679–695. doi: 10.1016/j.cell.2006.11.001.

Hadipour Moghaddam, S. P. *et al.* (2017) 'Redox-Responsive Polysulfide-Based Biodegradable Organosilica Nanoparticles for Delivery of Bioactive Agents', *ACS Applied Materials and Interfaces*, 9(25), pp. 21133–21146. doi: 10.1021/acsami.7b04351.

He, G. *et al.* (2010) 'Article Hepatocyte IKK b / NF- k B Inhibits Tumor Promotion and Progression by Preventing Oxidative', *Cancer Cell*. Elsevier Inc., 17(3), pp. 286–297. doi: 10.1016/j.ccr.2009.12.048.

He, Q. *et al.* (2010) 'The three-stage in vitro degradation behavior of mesoporous silica in simulated body fluid', *Microporous and Mesoporous Materials*. Elsevier Inc., 131(1–3), pp. 314–320. doi: 10.1016/j.micromeso.2010.01.009.

He, Q. *et al.* (2011) 'In vivo biodistribution and urinary excretion of mesoporous silica nanoparticles: Effects of particle size and PEGylation', *Small*, 7(2), pp. 271–280. doi: 10.1002/smll.201001459.

He, Q. and Shi, J. (2014) 'MSN Anti-Cancer Nanomedicines : Chemotherapy Enhancement , Overcoming of Drug Resistance , and Metastasis Inhibition', pp. 391–411. doi: 10.1002/adma.201303123.

Hou, Y. *et al.* (2011) 'hematogenous metastasis of liver cancers', *Nature Publishing Group*. Nature Publishing Group, 22(1), pp. 259–272. doi: 10.1038/cr.2011.139.

International Agency for Research on Cancer (2008) 'World Cancer report 2008', *Cancer Control*, 199, p. 512. doi: 10.1016/j.cma.2010.02.010.

IUPAC (1997) 'Coprecipitation', *Compendium of Chemical Terminology (the 'Gold Book')*, p. 336. doi: 10.1351/goldbook.I03352.

Katiyar, A. *et al.* (2010) 'Investigation of the mechanism of protein adsorption on ordered mesoporous silica using flow microcalorimetry', *Journal of Chromatography A*. Elsevier B.V., 1217(10), pp. 1583–1588. doi: 10.1016/j.chroma.2009.12.058.

Keller, A., Pedemonte, E. and Willmouth, F. M. (1970) ‘Cleavage of Structural Proteins during the Assembly of the Head of Bacteriophage T4’, *Nature*, 225, pp. 538–539.

Khamlue, R., Ounaroon, A. and Saelim, N. (2012) ‘PURIFICATION AND CHARACTERIZATION OF POLYSACCHARIDES EXTRACTED FROM Tremella fuciformis AND Auricularia auricula’, pp. 1–9.

Kim, H. *et al.* (2019) ‘Multifunctional hyaluronate – nanoparticle hybrid systems for diagnostic, therapeutic and theranostic applications’, *Journal of Controlled Release*. Elsevier, 303(December 2018), pp. 55–66. doi: 10.1016/j.jconrel.2019.04.003.

Kotov, N. A. (2010) ‘Inorganic nanoparticles as protein mimics’, *Science*, 330(6001), pp. 188–189. doi: 10.1126/science.1190094.

Kotredes, K. P. and Gamero, A. M. (2013) ‘Interferons as Inducers of Apoptosis in Malignant Cells’, *Journal of Interferon & Cytokine Research*, 33(4), pp. 162–170. doi: 10.1089/jir.2012.0110.

Kuby, J. *et al.* (2013) *Immunology*. doi: 10.1007/s13398-014-0173-7.2.

Landry, C. and Asuncion, P. B. (2014) ‘Effect of surface properties in protein corona development on mesoporous silica nanoparticles’. doi: 10.1039/C4RA03277B.

Leader, B., Baca, Q. J. and Golan, D. E. (2008) ‘Protein therapeutics: a summary and pharmacological classification’, 7(january), pp. 21–39.

Lennon, F. E. and Singleton, P. A. (2011) ‘Hyaluronan regulation of vascular integrity’, (June 2014).

Li, M. *et al.* (2014) ‘Efficient Side-chain Modification of Dextran via Base-catalyzed Epoxide Ring-opening and Thiol-ene Click Chemistry in Aqueous Media *’, 32(8), pp. 969–974. doi: 10.1007/s10118-014-1489-7.

Li, W. *et al.* (2018) ‘Molecular alterations of cancer cell and tumour microenvironment in metastatic gastric cancer’, *Oncogene*. Springer US, p. 1. doi: 10.1038/s41388-018-0341-x.

Li, X. *et al.* (2018) ‘Biomaterials A mesoporous silica nanoparticle e PEI e Fusogenic peptide system for siRNA delivery in cancer therapy’, 34(2013). doi: 10.1016/j.biomaterials.2012.10.072.

Liu, T. *et al.* (2011) ‘Single and repeated dose toxicity of mesoporous hollow silica nanoparticles in intravenously exposed mice’, *Biomaterials*. Elsevier Ltd, 32(6), pp. 1657–1668. doi: 10.1016/j.biomaterials.2010.10.035.

Lokina, S. *et al.* (2014) 'Cytotoxicity and antimicrobial activities of green synthesized silver nanoparticles', *European Journal of Medicinal Chemistry*. Elsevier Masson SAS, 76, pp. 256–263. doi: 10.1016/j.ejmech.2014.02.010.

Lu, Y., Sun, W. and Gu, Z. (2014) 'Stimuli-responsive nanomaterials for therapeutic protein delivery', *Journal of Controlled Release*. Elsevier B.V., 194, pp. 1–19. doi: 10.1016/j.jconrel.2014.08.015.

Lucigen Corporation (no date) *CloneSmart Cloning Kits (pSMART Vectors)*. 12–445. Middleton. Available at: www.lucigen.com.

Ma, M. *et al.* (2012a) 'Hyaluronic acid-conjugated mesoporous silica nanoparticles: Excellent colloidal dispersity in physiological fluids and targeting efficacy', *Journal of Materials Chemistry*, 22(12), pp. 5615–5621. doi: 10.1039/c2jm15489g.

Ma, M. *et al.* (2012b) 'Hyaluronic acid-conjugated mesoporous silica nanoparticles: Excellent colloidal dispersity in physiological fluids and targeting efficacy', *Journal of Materials Chemistry*, 22(12), pp. 5615–5621. doi: 10.1039/c2jm15489g.

Maeda, S. *et al.* (2005) 'IKK Couples Hepatocyte Death to Cytokine-Driven Compensatory Proliferation that Promotes Chemical Hepatocarcinogenesis', 121, pp. 977–990. doi: 10.1016/j.cell.2005.04.014.

Manning, M. C. *et al.* (2010) 'Expert Review Stability of Protein Pharmaceuticals : An Update', 27(4), pp. 544–575. doi: 10.1007/s11095-009-0045-6.

McComb, S. *et al.* (2014) 'Type-I interferon signaling through ISGF3 complex is required for sustained Rip3 activation and necroptosis in macrophages', *Proceedings of the National Academy of Sciences*, 111(31), pp. E3206–E3213. doi: 10.1073/pnas.1407068111.

Meier, M. *et al.* (2018) 'Synthesis of nanometric silica particles via a modified Stöber synthesis route', *Colloids and Surfaces A: Physicochemical and Engineering Aspects*. Elsevier, 538(September 2017), pp. 559–564. doi: 10.1016/j.colsurfa.2017.11.047.

Merck (2019a) *(3-Glycidyloxypropyl)trimethoxysilane*. Available at: (3-Glycidyloxypropyl)trimethoxysilane.

Merck (2019b) *IR Spectrum Table & Chart*. Available at: https://www.sigmaaldrich.com/technical-documents/articles/biology/ir-spectrum-table.html.

Mi, P. *et al.* (2015) 'Hybrid Calcium Phosphate-Polymeric Micelles Incorporating

Gadolinium Chelates for Imaging-Guided Gadolinium Neutron Capture Tumor Therapy', *ACS Nano*, 9(6), pp. 5913–5921. doi: 10.1021/acsnano.5b00532.

Mi, P. *et al.* (2017) 'Block copolymer-boron cluster conjugate for effective boron neutron capture therapy of solid tumors', *Journal of Controlled Release*. Elsevier, 254(March), pp. 1–9. doi: 10.1016/j.jconrel.2017.03.036.

Moerz, S. T. and Huber, P. (2015) 'pH-Dependent Selective Protein Adsorption into Mesoporous Silica'. doi: 10.1021/acs.jpcc.5b09606.

Mudunkotuwa, I. A., Minshid, A. Al and Grassian, V. H. (2014) 'ATR-FTIR spectroscopy as a tool to probe surface adsorption on nanoparticles at the liquid-solid interface in environmentally and biologically relevant media', *Analyst*, 139(5), pp. 870–881. doi: 10.1039/c3an01684f.

Nairi, V. *et al.* (2018) 'Interaction between bovine serum albumin and mesoporous silica nanoparticles functionalized with biopolymers', *Chemical Engineering Journal*. doi: 10.1016/j.cej.2018.01.011.

Naowanon, W. *et al.* (2018) 'Biphasic synthesis of amine-functionalized mesoporous silica nanospheres (MSN-NH2) and its application for removal of ferrous (Fe2 +) and copper (Cu2 +) ions', *Powder Technology*. Elsevier B.V., 323, pp. 548–557. doi: 10.1016/j.powtec.2016.09.014.

Novagen (2003) 'pET System Tutorial. Protein Expression. Procaryitic system', pp. 88–92.

Oba-yabana, I. *et al.* (2018) 'Acidic organelles mediate TGF- β 1-induced cellular fibrosis via (pro) renin receptor and vacuolar ATPase trafficking in human peritoneal mesothelial cells', (October 2017), pp. 1–14. doi: 10.1038/s41598-018-20940-x.

Observatory, G. C. (2018) *New Global Cancer Data: GLOBOCAN 2018*. Available at: https://www.uicc.org/news/new-global-cancer-data-globocan-2018 (Accessed: 4 July 2019).

Olov, N., Bagheri-khoulenjani, S. and Mirzadeh, H. (2018) 'Review Article Combinational drug delivery using nanocarriers for breast cancer treatments : A review', pp. 1–12. doi: 10.1002/jbm.a.36410.

Papadopoulos, J. S. and Agarwala, R. (2007) 'COBALT: Constraint-based alignment tool for multiple protein sequences', *Bioinformatics*, 23(9), pp. 1073–1079. doi: 10.1093/bioinformatics/btm076.

Parkins, K. M. *et al.* (2018) 'Multimodality cellular and molecular imaging of concomitant tumour enhancement in a syngeneic mouse model of breast cancer metastasis', (March), pp. 1–10. doi: 10.1038/s41598-018-27208-4.

Pfeffer, L. M. *et al.* (1998) 'Biological properties of recombinant alpha-interferons: 40th anniversary of the discovery of interferons.', *Cancer research*, 58(12), pp. 2489–99. Available at: http://www.ncbi.nlm.nih.gov/pubmed/9635566.

Qin, Y. *et al.* (2016) 'Using hyaluronic acid-functionalized pH stimuli-responsive mesoporous silica nanoparticles for targeted delivery to CD44-overexpressing cancer cells', *International Journal of Nanomedicine*, Volume 11, pp. 6485–6497. doi: 10.2147/ijn.s117184.

Qiu, Z. *et al.* (2016) 'Hepatocellular carcinoma cell lines retain the genomic and transcriptomic landscapes of primary human cancers', *Nature Publishing Group*. Nature Publishing Group, (May), pp. 1–13. doi: 10.1038/srep27411.

Radhakrishnan, R. *et al.* (1996) 'Zinc mediated dimer of human interferon-alpha 2b revealed by X-ray crystallography.', *Structure (London, England : 1993)*, 4, pp. 1453–1463. doi: 8994971.

Rajendran, S. *et al.* (2016) 'Ce3+-ion-induced visible-light photocatalytic degradation and electrochemical activity of ZnO/CeO2 nanocomposite', *Scientific Reports*. Nature Publishing Group, 6(July), pp. 1–11. doi: 10.1038/srep31641.

De Rosales, R. T. M. (2014) 'Potential clinical applications of bimodal PET-MRI or SPECT-MRI agents', *Journal of Labelled Compounds and Radiopharmaceuticals*, 57(4), pp. 298–303. doi: 10.1002/jlcr.3154.

Rosenholm, J. M. *et al.* (2012) 'Nanoparticles in targeted cancer therapy: mesoporous silica nanoparticles entering preclinical development stage', *Nanomedicine*, 7(1), pp. 111–120. doi: 10.2217/NNM.11.166.

Salis, A. *et al.* (2016) 'Mesoporous Silica Nanoparticles Functionalized with Hyaluronic Acid and Chitosan Biopolymers . Effect of Functionalization on Cell Internalization'. doi: 10.1021/acsbiomaterials.5b00502.

Sambrock, J., Fritschf, E. F. and MANIATIS, T. (1989) *Molecular Cloning, A Laboratory Manual*.

Senapati, S. *et al.* (2018) 'Controlled drug delivery vehicles for cancer treatment and their performance', *Signal Transduction and Targeted Therapy*, 3(1), p. 7. doi: 10.1038/s41392-017-0004-3.

Senbanjo, L. T. and Chellaiah, M. A. (2017) 'CD44: A Multifunctional Cell Surface Adhesion Receptor Is a Regulator of Progression and Metastasis of Cancer Cells', *Frontiers in Cell and Developmental Biology*, 5(March). doi: 10.3389/fcell.2017.00018.

Shen, Z., Wu, A. and Chen, X. (2017) 'Iron Oxide Nanoparticle Based Contrast Agents for Magnetic Resonance Imaging', *Molecular Pharmaceutics*, 14(5), pp. 1352–1364. doi: 10.1021/acs.molpharmaceut.6b00839.

Shi, H. *et al.* (2019) 'Charge-Selective Delivery of Proteins Using Mesoporous Silica Nanoparticles Fused with Lipid bilayers Charge-Selective Delivery of Proteins Using Mesoporous Sili- ca Nanoparticles Fused with Lipid bilayers'. doi: 10.1021/acsami.8b15390.

Slowing, I. I., Trewyn, B. G. and Lin, V. S. (2007) 'Mesoporous Silica Nanoparticles for Intracellular Delivery of Membrane-Impermeable Proteins', (22), pp. 8845–8849. doi: 10.1021/ja0719780.

Spangenberg, H. C., Thimme, R. and Blum, H. E. (2008) 'Evolving therapies in the treatment of hepatocellular carcinoma.', *Biologics : targets & therapy*, 2(3), pp. 453–62. Available at: http://www.pubmedcentral.nih.gov/articlerender.fcgi?artid=2721397&tool=pmcentrez&rendertype=abstract.

Srivastava, P. *et al.* (2005) 'Overexpression and purification of recombinant human interferon alpha2b in Escherichia coli', *Protein Expression and Purification*, 41(2), pp. 313–322. doi: 10.1016/j.pep.2004.12.018.

Stephen F. Altschul *et al.* (1997) 'Gapped BLAST and PSI-BLAST: a new generation of protein database search programs', *Nucleic Acids Research*, 25(17), pp. 3389–3402. doi: 10.1093/nar/25.17.3389.

Tamori, A. *et al.* (2016) 'Recent Advances in Antiviral Therapy for Chronic Hepatitis C', *Mediators of Inflammation*, 2016, pp. 1–11. doi: 10.1155/2016/6841628.

Thomas, Christoph; Moraga, Ignacio; Levin, Doron; Krutzik, Peter O.; Podoplelova; Yulia; Trejo, Angelica; Lee, Choongho; Yarden, Ganit; Vleck, Susan E.; Glenn, Jeffrey S.; Nolan, Garry P.; Piehler, Jacob Schreiber, Gideon and Garcia, K. C. (2011) 'Structural linkage between ligand discrimination and receptor activation by type I interferons', *Cell*, 146(4), pp. 621–632. doi: 10.1016/j.cell.2011.06.048.

Thorne, R. F., Legg, J. W. and Isacke, C. M. (2004) 'The role of the CD44 transmembrane and cytoplasmic domains in co-ordinating adhesive and signalling

events', 44(exon 1). doi: 10.1242/jcs.00954.

Tu, J. *et al.* (2016) 'Mesoporous Silica Nanoparticles with Large Pores for the Encapsulation and Release of Proteins'. doi: 10.1021/acsami.6b11324.

Valastyan, S, Weinberg, R. (2011) 'Tumor metastasis: molecular ınsights and evolving paradigms', *Cell*, 14;147(2)(2), pp. 275–292. doi: 10.1016/j.cell.2011.09.024.Tumor.

Wang, Y. *et al.* (2016) 'Charge-Reversal APTES-Modified Mesoporous Silica Nanoparticles with High Drug Loading and Release Controllability', *ACS Applied Materials and Interfaces*, 8(27), pp. 17166–17175. doi: 10.1021/acsami.6b05370.

De Weerd, N. A., Samarajiwa, S. A. and Hertzog, P. J. (2007) 'Type I interferon receptors: Biochemistry and biological functions', *Journal of Biological Chemistry*, 282(28), pp. 20053–20057. doi: 10.1074/jbc.R700006200.

Williams, K. *et al.* (2013) 'Experimental Biology and Medicine'. doi: 10.1177/1535370213480714.

Wolfbeis, O. S. (2015) 'An overview of nanoparticles commonly used in fluorescent bioimaging', *Chemical Society Reviews*. Royal Society of Chemistry, 44(14), pp. 4743–4768. doi: 10.1039/c4cs00392f.

Wu, D. and Prives, C. (2017) 'Relevance of the p53 – MDM2 axis to aging', *Nature Publishing Group*. Nature Publishing Group, pp. 1–11. doi: 10.1038/cdd.2017.187.

Xiwei Zheng, Cong Bi, Marissa Brooks, and D. S. H. (2015) 'HHS Public Access', *Anal Chem.*, 25(4), pp. 368–379. doi: 10.1016/j.cogdev.2010.08.003.Personal.

Xu, M., Ca, A. and Hamm, P. (2016) 'Protein Structural Memory In fl uences Ligand Binding Mode (s) and Unbinding Rates'. doi: 10.1021/acs.jctc.5b01052.

Zhang, J. *et al.* (2014a) 'Synthesis and characterization of hyaluronic acid/human-like collagen hydrogels', *Materials Science and Engineering C*. Elsevier B.V., 43, pp. 547–554. doi: 10.1016/j.msec.2014.07.058.

Zhang, J. *et al.* (2014b) 'Synthesis and characterization of hyaluronic acid/human-like collagen hydrogels', *Materials Science and Engineering C*. Elsevier B.V., 43, pp. 547–554. doi: 10.1016/j.msec.2014.07.058.

Zhang, K. J. *et al.* (2017) 'A potent in Vivo antitumor efficacy of novel recombinant type i interferon', *Clinical Cancer Research*, 23(8), pp. 2038–2049. doi: 10.1158/1078-0432.CCR-16-1386.

Zhao, D. *et al.* (1998) ‘Triblock copolymer syntheses of mesoporous silica with periodic 50 to 300 angstrom pores’, *Science*, 279(5350), pp. 548–552. doi: 10.1126/science.279.5350.548.

Zhou, Y., Quan, G., Wu, Q., Zhang, X. and Niu, B. (2018) ‘Mesoporous silica nanoparticles for drug and gene delivery’, *Acta Pharmaceutica Sinica B*. Elsevier B.V., 8(2), pp. 165–177. doi: 10.1016/j.apsb.2018.01.007.

Zhou, Y., Quan, G., Wu, Q., Zhang, X., Niu, B., *et al.* (2018) ‘Mesoporous silica nanoparticles for drug and gene delivery’, *Acta Pharmaceutica Sinica B*. Elsevier B.V., 8(2), pp. 165–177. doi: 10.1016/j.apsb.2018.01.007.

Zhuravlev, L. T. (2000) ‘The surface chemistry of amorphous silica . Zhuravlev model’, 173, pp. 1–38.

Supplementary Data

1. Supplementary Data #1

The experimental design of this work was executed as described in the following diagram, represented in Supplementary Figure 1.

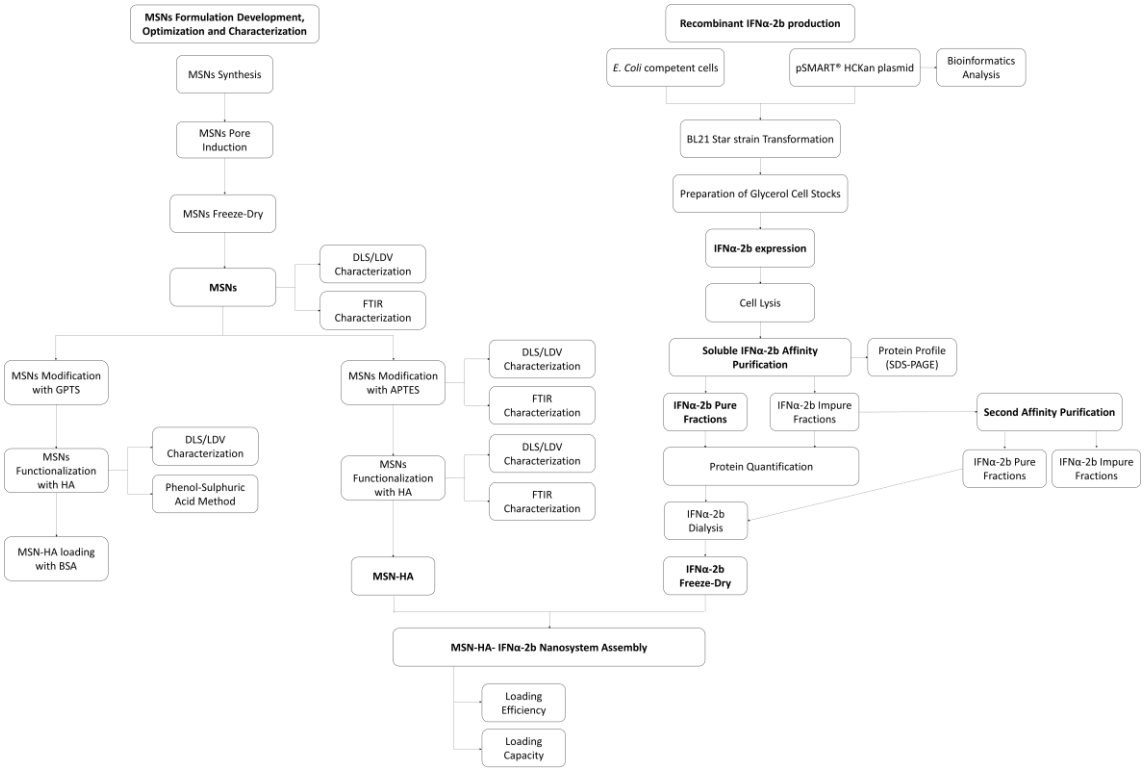

Supplementary Figure 1- Diagram representing the experimental design executed in this work, whose major steps are marked in bold.

2. Supplementary Data #2

Supplementary Table 1 presented in this chapter specifies DLS and LDV readings of all types of mesoporous silica nanoparticles used and developed in this work. Also, this data is represented in Figure 18.

Supplementary Table 1 – Average hydrodynamic diameter of unmodified (MSN-OH), modified (MSN-NH_2) and functionalized (MSN-HA) mesoporous silica nanoparticles and respective superficial charge (ζ-potential). Data are expressed as mean ± SEM of 4 independent experiments.

MSN Type	**Diameter (nm)**	**ζ-potential (mV)**
MSN-OH	403.4 ± 28.97	-32.06 ± 1.467
MSN-NH_2	538.0 ± 23.16	31.33 ± 0.729
MSN-HA	830.3 ± 36.91	-34.42 ± 0.484